Graduate School ETD Form 9
(Revised 12/07)

PURDUE UNIVERSITY
GRADUATE SCHOOL
Thesis/Dissertation Acceptance

This is to certify that the thesis/dissertation prepared

By Omar A. Elmaraghi

Entitled
INTEGRATED MULTIBODY DYNAMICS AND FATIGUE MODELS FOR PREDICTING THE FATIGUE LIFE OF POLY–V RIBBED BELTS

For the degree of Master of Science in Mechanical Engineering

Is approved by the final examining committee:

Tamer Wasfy
Chair

Hazim El-Mounayri

Sohel Anwar

To the best of my knowledge and as understood by the student in the *Research Integrity and Copyright Disclaimer (Graduate School Form 20)*, this thesis/dissertation adheres to the provisions of Purdue University's "Policy on Integrity in Research" and the use of copyrighted material.

Approved by Major Professor(s): Tamer Wasfy

Approved by: Sohel Anwar 03/04/2013
Head of the Graduate Program Date

INTEGRATED MULTIBODY DYNAMICS AND FATIGUE MODELS FOR PREDICTING THE FATIGUE LIFE OF POLY–V RIBBED BELTS

A Thesis
Submitted to the Faculty
of
Purdue University
by
Omar A. Elmaraghi

In Partial Fulfillment of the
Requirements of the Degree
of
Masters of Science in Mechanical Engineering

May 2013
Purdue University
Indianapolis, Indiana

I dedicate this thesis to my parents as an appreciation for their unconditional support to me until I finished my degree. I would like also to dedicate this work to my undergraduate professors; Dr. Hany Moneib, Dr. Ahmed Abo Habsa and Dr. Khaled Shebl for being precious teachers, advisors and examples, and for motivating me to continue my graduate studies.

ACKNOWLEDGEMENT

This thesis is the result of many months of work and it would not have been possible to complete without the support of my family, teachers, colleagues and friends.

I would like to show my gratitude to my advisor, Dr. Tamer Wasfy for teaching, advising and supporting me during the course of my thesis. I also want to extend my thanks to the thesis committee; Dr. Hazim Elmounayri and Dr. Sohel Anwar, who taught me a lot and gave me advice.

This thesis was done in cooperation with Cummins Inc. which supplied the experimental results and the case study. I would like to thank Amit Gabale and Ilya Piraner, from Cummins Inc. for their support and cooperation.

I feel grateful to my friends and peers for their exchange of knowledge and experience. Particularly, I would like to thank Tarek Elharis, Mohamed Kenawey and Daniel Aw for their help and support.

TABLE OF CONTENTS

Page

Page

Page

LIST OF TABLES

LIST OF FIGURES

Figure Page

Figure Page

Figure Page

Figure Page

Figure Page

ABSTRACT

Elmaraghi, Omar. M.S.M.E., Purdue University, May 2013. Integrated Multibody Dynamics and Fatigue Models for Predicting the Fatigue Life of Poly–V Ribbed Belts. Major Professor: Tamer Wasfy.

In this thesis, a high fidelity numerical model was developed using a multibody dynamics/finite element code to simulate a belt-drive that transmits power from a turbine of a Rankin cycle (that uses the exhaust waste heat of the internal combustion engine as a heat source) to the crank shaft of the engine. The belt was modeled using three-node beam elements to account for the belt axial and bending stiffness/damping, while the pulleys, shafts and tensioner body were modeled as rigid bodies. The pulleys have a cylindrical contact surface. The *penalty technique* was used to model normal contact between the belt and the pulleys. The code uses a time-accurate explicit numerical integration technique to solve the multibody dynamics differential equations.

An *asperity-based friction* model was used to approximate Coulomb friction between the belt and the pulleys. To account for the stiffness/damping of the shafts, torsional spring(s) were added at one or both sides of each shaft. Virtual sensors were placed on each belt span to measure belt tension, belt deflection and number of belt node at the sensor position. The model inputs are crankshaft angular velocity and torque applied on the turbine. The predicted angular velocity and the torque transmitted by a drive shaft are compared to experimental results supplied by Cummins, Inc. and excellent agreement was found with error less than 15% in the vibration amplitudes of the main frequencies.

A Parameter sensitivity study was performed by changing parameters such as the tensioner arm viscous and coulomb damping, belt axial stiffness and damping, belt bending stiffness and damping, the coefficient of friction between the belt and pulleys, gear tooth backlash, gear tooth stiffness and damping, and the shafts stiffness and damping. Then the effect of each change on the response was observed. It was found that the viscous and frictional (Coulomb) damping of the tensioner arm, and the coefficient of friction between the belt and the pulleys have the most significant effect on the system's response.

Predicted normal and tangential forces between the belt and the pulleys as well as the tension force in the belt were used to calculate different stresses experienced at the belt rib. The different stresses were added together using Sine's theory and represented by an equivalent uniaxial stress, which is used as a damage criterion to estimate the belt life-time based on a fatigue model. As the belt chords have much larger Young's modulus than the rubber, the chords limit the rubber strain keeping it in the linear elastic zone. Hence, the *High Cycle Fatigue (HCF)* model was used along with the modified Basquin relation to estimate the fatigue life of the belt. The fatigue life was estimated for different belt-drive operating ranges. The engine duty cycle, which specifies the percent of time the belt operates in each operating range, was used to estimate the overall fatigue life of the belt.

Finally, three different alternative configurations of the belt-drive were built and simulated for the same input, the same material properties and the same belt initial tension, but different idler pulley positions and configuration. The response was observed for each configuration in terms of the stresses and fatigue life. The results of the three configurations and the baseline were compared.

1. INTRODUCTION

Belt-drives are used for power transmission in many applications such as automotive accessory drives. They have the following advantages over alternative power transmission systems:

- They generally have lower cost than other power transmission systems.
- They are easier to maintain due to easy installation and the lack of need for lubrication.
- They are tolerant to sudden loads
- They allow high flexibility in the distances between drive and driven shafts.

Flat belts were the first type of belts to be introduced in industry. Flat belts have much lower maximum allowable transmitted power than alternative mechanical power transmission systems such as gears. One way to increase the power transmission capacity of a belt is to make it wider so that the contact area between the belt and the pulley becomes bigger. The V-belt was introduced to enable transmitting more power than flat belts of the same width due to the wedge action between the belt V-rib and the pulley groove. The V-belt power transmission capacity cannot be increased by increasing the belt width (like the case in the flat belt) because the wedge profile will change. To increase the power transmission capacity of the V-belt, multiple belts are installed on the same pulley to share load. The evolution of this concept led to the development of the *poly-V* ribbed belts which integrate the features of both the flat belt as well as the V-belt.

The poly-V belt can be considered as a flat belt with multiple V-shaped cross sectional ribs connected in parallel on one of its sides. The poly-V belt is now widely used in different applications especially the automotive industry.

1.1 Motivation

As belt-drives become more widely used for power transmission, it was essential to find methods to help designers and researchers design the belt-drive that would perform the required function. Experimental results are the most trusted; however, they require special arrangements like labs and special measuring devices. Also, a physical model of the system needs to be manufactured. This makes experimental validation of belt-drive designs an expensive process, which is not favorable for technology producers. Also some of the experiments, such as high cycle fatigue life, may take a long time to obtain the results which is not convenient for a designer who needs to run the experiment many times to tune the design. As a result, depending on experimental validation hinders the progress of spread of the technology and limits the designer abilities.

1.1.1 Present Application of Belt-Drive

Internal combustion engines waste around one third of the produced heat energy in the exhaust gasses [1, 2] (see Figure 1.1). Moreover, emission regulations are becoming stricter to limit Greenhouse Gasses (GHG) emissions including CO_2, which requires that less fuel be burnt in the engine. For those reasons, it is essential that researchers work on finding solutions to fuel efficiency, and consequently reducing fuel consumption and emissions. Currently many technologies are under development to recover the heat energy wasted through exhaust and coolant (see Figure 1.1). One of these technologies introduced is to add a Rankin cycle that uses the wasted heat energy in the tail pipe as input heat energy to evaporate a working fluid. The evaporated fluid (steam) rotates a turbine, which produces power. The waste heat recovery system can reduce the fuel consumption by up to 10% [3] and increase the engine power by 10% on

cruising speed on highways [2], thus decreasing the amount of emissions produced for the same trip.

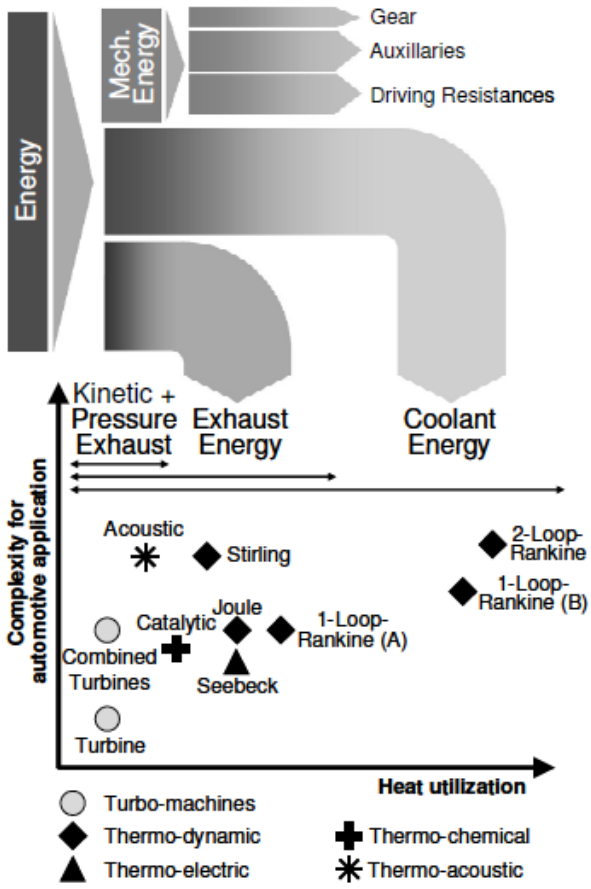

Figure 1.1 Energy utilization in ICE [2]

In order to add the power produced from the turbine (in the Rankin cycle) to the engine power, a mechanical power transmission system is required. A belt-drive was the preferred solution due to the advantages of belt-drives mentioned in the beginning of this chapter.

1.2 Literature Review

The belt drive has many advantages that make it the preferred solution for many applications, one of which is the accessory serpentine belt in the automotive industry. This made it necessary to understand the failure modes of belt-drives and develop methods to predict belt-drive failure. One of the most critical failure modes of a belt-drive is failure of the belt due to fatigue.

In 1965, G. J. Lake and P. B. Lindley [4] studied the mechanical fatigue limit for rubber due to a flaw cut growth which are initially present in rubber. The study was looking for the minimum tear energy under which a mechanical rupture can occur in the presence of oxidation. This helps to estimate the performance of the belt rubber under cyclic loading. In 1988, Y. S. Huang and O. H. Yeoh [5] further studied failure modes of a rubber chord composite. The study included a penny shaped crack initiate in the rubber where the crack grows. They employed a fracture mechanics approach using the strain energy release rate per unit area increase on one surface of a growing crack. They developed a theory to estimate the crack growth rate and the fatigue life. The theory has been validated using experimental results and both results were found to be in agreement.

In 1981 J. N Fawcett [6] reviewed studies that looked at various analytical solution methods related to chains and belt drives vibrations, noise, material properties and pulley belt interaction. With the development in computational power, the trend of solutions changed from analytical models to numerical models solved by computer simulation. In 1989, D. Frhzson [7] developed a theory to estimate the service life of the belt. However, the study was based on observing a certain parts of the belt when the belt is running under loading conditions, but not the entire belt. This approximation was taken to decrease the amount of computation and to avoid boundary effects. The study focused on three modes of failure, which are radial crack in the rubber, separation between rubber and chord and chord breakage.

S. Karunendiran, M. Clark and J. W.Zu [8, 9] used the stress life approach to create a belt life equation. The various types of stresses affecting the belt drive in a

planner multi-axial system were used in the fatigue model to estimate the life-time of the belt. An equivalent uniaxial approach was used to represent the uniaxial system in the fatigue model. The fatigue index and the fatigue strength coefficient are estimated empirically. The belt fatigue model was validated by experimental results from different configurations of belt drives. However, the stresses in the numerical model were described by equations that used curve fitting. The studies didn't include a time accurate prediction of the stresses on the belt.

One of the biggest challenges that faced researchers was to determine the material fatigue properties. Those properties were determined empirically by analyzing experimental results. Although the studies were validated and had a reasonable agreement with experimental results, they did not count for the effect of the operating temperature. When the operating temperature of the belt changes, the material properties of the belt change. Consequently, the forces and stresses applied on the belt change in magnitude. S. Sundararaman el al. [10] studied in 2009 the effect of temperature on the fatigue life of a V-ribbed serpentine belt. They employed a finite element model that can take the thermal degradation of the belt properties into account. This model was used to study the propagation of a crack due to a flaw that initially exists on the rib tip of the belt. It was shown that belt rubber suffers significant degradation due to the increase in working temperature, resulting in shorter fatigue life. T. Ha Anh and T. Vu-Khanh [11] studied the influence of temperature change on material properties. They used the polychloroprene (CR) to conduct the study. This material is usually used in the belt rubber manufacturing. Nassiri [12] proposed a new approach to determine the hyperelastic material properties of the belt rubber. Nassiri calculated the chord's elastic modulus of the belt. The results of calculation showed agreement with the results obtained from a tensile test. The predicted values of the belt parameters were used in finite element model. This model was used to estimate the belt fatigue life of a typical automotive belt-drive.

As belt wear progresses, the V-ribbed belt shape deforms and the load is no longer distributed uniformly. In 1998, D Yu et al [13] studied the effect of wear on the traction capacity of the belt. In their approach, they attempted to find how the load was

shared between the rib flanks and the rib root to achieve their purpose. They built a numerical model to simulate the new belt and another one to simulate the worn belt. The loading of the belt and the traction capacity were monitored in the numerical models. Wear was found to happen in three regions; the rib shoulder, the rib flanks and the rib root. It was found that belt wear resulted in 10 percent reduction in the maximum belt traction. The study, however, did not discuss the prediction of the life of the belt.

With further advancement in computation power, many endeavors were taken to simulate the belt drive with high fidelity. In 2002, Michael J. Leamy and Tamer Wasfy [14] worked on simulating a pulley belt drive system using a dynamic finite element model. The model consisted of simple system of two pulleys connected with a belt. This model was employed to determine the transient and steady state response of the system. The pulleys were modeled as rigid bodies with circular constraints and the belt was modeled using standard truss elements. The friction between both the pulleys and the belt was modeled using penalty formulation with friction laws that approximates coulomb friction. The drive was incorporated in an explicit finite element code. The solution was validated by comparing to an exact analytical solution [15] of steady state and an excellent agreement was found. T. Wasfy, M. Leamy and R. J. Meckstroth [16] used the multibody dynamics explicit finite element technique presented in [14] to predict belt drive natural frequencies. Two methods were employed to find the natural frequency of the system. The first technique applied a sharp impulse to the system and subsequently extracted the system natural frequencies using an FFT. The second technique applied a harmonic excitation to the system, then increasing the frequency of the harmonic excitation in a linear pattern and observing the frequency at which the system will have the highest response. Although these studies predicted the stresses very accurately, they did not use these responses to calculate the fatigue life of the belt due to the effect of these stresses.

1.3 Objectives

The wide spread use of belt-drives along with the limitations of experimental validation generated the need to have more flexible, cheaper but yet accurate methods to estimate the behavior of different belt-drives designs. With the boom in the computational power, and the decrease in computation expense, numerical analysis becomes a more attractive alternative to physical experiments. The challenge has always been how accurate is the numerical model (i.e. how close are the numerical results to the real system).

The thesis has four main objectives. The first aims at building a high fidelity numerical model of a practical belt-drive. In order to prove the model's accuracy, the numerical model is validated by comparing its response to experimental results. The next objective follows validating the numerical model, and it aims at conducting a parameter sensitivity study by changing one parameter at a time and observing the change of response. This study will give the designers an estimate of the impact of each parameter on the belt-drive dynamic response. The third objective aims at creating a belt fatigue life model and to be used to estimate the belt fatigue life for the practical belt-drive. The fourth and final objective is to change the belt-drive configuration, such as removing a pulley or changing its place, and observing the effect of this change on the belt fatigue life.

The study contributes to this field through integrating the multibody dynamics model presented in [17-20] with the fatigue model presented in [8, 12] to obtain a full model that can predict the belt fatigue life. The multibody dynamics model gives a time accurate prediction of the forces that the belt experience, which are used to calculate belt stresses. The stresses are then used in the fatigue model as a damage criterion. Another contribution of this thesis is creating and experimentally validating a high-fidelity numerical model of a practical belt-drive. Another contribution is to evaluate the sensitivity of the belt-drive's response due to the change of the value of the model parameters. The final contribution is exercising the integrated model on different belt configurations and comparing the results to show the capability of the integrated model in

comparing different configurations. The integrated multibody dynamics and fatigue models can be used as a useful tool for optimizing belt-drives' fatigue life.

1.4 Thesis Organization

Chapter 1 served as an introduction to belt-drive history and importance. It also presented the transition and developments in belt shape and configuration showing the advantages of each new configuration and the reason behind this development. Then, a literature review on belt fatigue life prediction and multibody dynamics of belt-drives was presented. The final section stated the thesis objectives.

The numerical model was solved using the explicit time integration *Dynamic Interactive simulator* (DIS) code [17]. Chapter 2 presents the multibody dynamics equations used in the numerical model. It starts with the general equations of motion. Then it shows the strategy of modeling and formulating the joints and how to incorporate the joint constraints in the solution procedure. The asperity friction model, used to approximate coulomb friction, is also shown along with its formulation. The three-node beam element used to model the belt is then described. Finally, the explicit solution procedure that incorporates the joint and contact constraints is presented at the end of chapter 2.

Moving to the case study, Chapter 3 has description of the belt-drive that has been studied. It describes the components, geometry, loading and input angular velocities of the system. To validate the response of the numerical model, it was compared to experimental results of the response of a physical model. The comparison is shown in Chapter 3 in form of comparison plots.

System response changes if some of the belt parameters change. There was an interest in knowing the sensitivity of the belt-drive response due to change in specific belt parameter. In Chapter 4 one parameter is changed every time and the response is

observed for any variation. Different parameters were studied such as stiffness, damping, friction and clearances for different components in the system.

Chapter 5 presents the procedure used to calculate the stresses acting on the belt rib. Different types of stresses are taken into account such as axial, transverse shear and bending stresses. Also a uniaxial equivalent stress is used to approximate the multi-axial stress. Sine's rule was employed to find the equivalent uniaxial stress.

Chapter 6 discusses the estimation of the belt fatigue life-time based on the fatigue theory. It begins with a general overview about the concept and definitions of fatigue. This includes the *low cycle fatigue* (LCF), *High cycle fatigue*, *S-N fatigue curve* and the effect of the *mean stress* on the fatigue life. The fatigue model is described in this chapter along with the derivations and equations. The equivalent uniaxial stress system, calculated in Chapter 5 is used in the fatigue model as a damage criterion. Chapter 6 also introduces the *cumulative damage theory* in the fatigue calculation applied on multi-pulley belt-drives. The fatigue model is applied on the case study belt-drive, which is the focus of this thesis, in order to estimate the fatigue life of the belt-drive. Results are listed and discussed at the end of the chapter.

Different alternative belt configurations are introduced in Chapter 7. The alternatives are supposed to do the same job under the same operating conditions but only different in configuration. The forces and stresses are observed for each of the alternative configuration and then the fatigue life is estimated using the fatigue model introduced in Chapter 6. Comparative results are listed and discussed at the end of the chapter.

Chapter 8 summarizes the work done in this thesis and conclusions reached from the research. It also presents recommendation for future research that can be performed to build on this research.

2. MULTIBODY DYNAMIC EQUATION

The multibody dynamics model was presented in [16, 19, 20] including the governing equations as well as joints and frictional contact model. Furthermore, the multibody dynamics model was used in [14, 15, 21] to model a belt-drive and study its response (mainly frictional contact). Those studies did not calculate the fatigue life for the belt.

2.1 Governing Equations

In the subsequent equations follows the following convention [18]:

- The indicial notation is used.
- The Einstein summation convention is used for repeated subscript indices unless otherwise noted.
- Upper case subscript indices denote node (or rigid body) numbers.
- Lower case subscript indices denote vector component number.
- The superscript denotes time.
- A superposed dot denotes a time derivative.

A multibody dynamic system consists of multiple rigid bodies (which are modeled using finite element nodes) that may come into contact with each other and are connected through joints.

.

The dynamics of each body will affect all other bodies. If we have a multibody system consisting of *N* rigid bodies, then we can write semi-discrete [18, 19] Newton-Euler equations for each rigid body (node) as:

$$M_k \ddot{X}^t_{Ki} = F^t_{ki} \tag{2.1}$$

$$I_{Kij}\ddot{\theta}^t_{Ki} = T^t_{ki} - \left(\dot{\theta}^t_{Kk} \times \left(I_{Kij}\dot{\theta}^t_{Kk}\right)\right)_{k_i} \tag{2.2}$$

Where:

Superscript t: is the running time.

Lower case indices indicate coordinate numbers.

Upper case indices indicate rigid body number.

K: is the rigid body number K = 1 to N

N: is the total number of rigid bodies.

M_k: is the mass of body K.

I_{Kij}: is the mass moment of inertia of body K.

X^t_{Ki}: is the position vector of the c.g. of body K.

$\dot{X}^t_{Ki}$: is the velocity vector of the c.g. of body K.

$\ddot{X}^t_{Ki}$: is the acceleration vector of the c.g. of body K.

$\dot{\theta}^t_{Kk}$: is the angular velocity vector of the rigid body K.

$\ddot{\theta}^t_{Ki}$: is the angular acceleration vector of the rigid body K.

F^t_{ki}: is the force vector acting on the rigid body K.

T^t_{ki}: is the applied/external moment vector acting on the rigid body K.

We can use the trapezoidal integration rule to integrate each body's translational equations of motion (6.3) in time [19]:

$$\dot{X}^{\,t}_{Kj} = \dot{X}^{\,t-\Delta t}_{Kj} + 0.5\,\Delta t\,(\ddot{X}^{\,t}_{Kj} + \ddot{X}^{\,t-\Delta t}_{Kj}) \tag{2.3}$$

$$X^{\,t}_{Kj} = X^{\,t-\Delta t}_{Kj} + 0.5\,\Delta t\,(\dot{X}^{\,t}_{Kj} + \dot{X}^{\,t-\Delta t}_{Kj}) \tag{2.4}$$

where Δt: is the time step.

Similarly, we can use the trapezoidal rule to integrate each body's rotational equations of motion (3.2) in time [19]:

$$\dot{\theta}_{Kj}^{t} = \dot{\theta}_{Kj}^{t-\Delta t} + 0.5\,\Delta t\,(\ddot{\theta}_{Kj}^{t} + \ddot{\theta}_{Kj}^{t-\Delta t}) \tag{2.5}$$

$$\Delta\theta_{Kj}^{t} = 0.5\,\Delta t\,(\dot{\theta}_{Kj}^{t} + \dot{\theta}_{Kj}^{t-\Delta t}) \tag{2.6}$$

Where:

$\Delta\theta_{Kj}^{t}$: is the incremental rotation vector of body *K*.

We can calculate the rigid body rotation matrix at time *t* as [19]:

$$R_{Kij}^{t} = R_{Kik}^{t-\Delta t}\, R_{Kkj}(\Delta\theta_{Kl}^{t}) \tag{2.7}$$

$$R_{Kkj}(\Delta\theta_{Kl}^{t}) = \begin{bmatrix} \cos(\Delta\theta_{K3}^{t}) & -\sin(\Delta\theta_{K3}^{t}) & 0 \\ \sin(\Delta\theta_{K3}^{t}) & \cos(\Delta\theta_{K3}^{t}) & 0 \\ 0 & 0 & 1 \end{bmatrix} \begin{bmatrix} \cos(\Delta\theta_{K2}^{t}) & 0 & \sin(\Delta\theta_{K2}^{t}) \\ 0 & 1 & 0 \\ -\sin(\Delta\theta_{K2}^{t}) & 0 & \cos(\Delta\theta_{K2}^{t}) \end{bmatrix} \begin{bmatrix} 1 & 0 & 0 \\ 0 & \cos(\Delta\theta_{K1}^{t}) & -\sin(\Delta\theta_{K1}^{t}) \\ 0 & \sin(\Delta\theta_{K2}^{t}) & \cos(\Delta\theta_{K2}^{t}) \end{bmatrix}$$

$$\Leftrightarrow \qquad R(\Delta\theta_{Kl}^{t}) = R(\Delta\theta_{K3}^{t})\, R(\Delta\theta_{K2}^{t})\, R(\Delta\theta_{K1}^{t}) \tag{2.8}$$

Where:

$$R(\Delta\theta_{K1}^{t}) = \begin{bmatrix} 1 & 0 & 0 \\ 0 & \cos(\Delta\theta_{K1}^{t}) & -\sin(\Delta\theta_{K1}^{t}) \\ 0 & \sin(\Delta\theta_{K2}^{t}) & \cos(\Delta\theta_{K2}^{t}) \end{bmatrix}$$

$$R(\Delta\theta_{K2}^{t}) = \begin{bmatrix} \cos(\Delta\theta_{K2}^{t}) & 0 & \sin(\Delta\theta_{K2}^{t}) \\ 0 & 1 & 0 \\ -\sin(\Delta\theta_{K2}^{t}) & 0 & \cos(\Delta\theta_{K2}^{t}) \end{bmatrix}$$

$$R(\Delta\theta_{K3}^{t}) = \begin{bmatrix} \cos(\Delta\theta_{K3}^{t}) & -\sin(\Delta\theta_{K3}^{t}) & 0 \\ \sin(\Delta\theta_{K3}^{t}) & \cos(\Delta\theta_{K3}^{t}) & 0 \\ 0 & 0 & 1 \end{bmatrix}$$

If the incremental angles $\Delta\theta_{Ki}^{t}$ are infinitesimally small then the order of the product $R(\Delta\theta_{K3}^{t})\, R(\Delta\theta_{K2}^{t})\, R(\Delta\theta_{K1}^{t})$ is not important. However, since $\Delta\theta_{Ki}^{t}$ are small but

finite. We should vary the order of the product during our solution procedure. Since there are three matrices therefore there are six possible orders:

$$
\begin{aligned}
R(\Delta\theta_{Kl}^t) &= R(\Delta\theta_{K3}^t)\,R(\Delta\theta_{K2}^t)\,R(\Delta\theta_{K1}^t) \\
R(\Delta\theta_{Kl}^t) &= R(\Delta\theta_{K3}^t)\,R(\Delta\theta_{K1}^t)\,R(\Delta\theta_{K2}^t) \\
R(\Delta\theta_{Kl}^t) &= R(\Delta\theta_{K2}^t)\,R(\Delta\theta_{K1}^t)\,R(\Delta\theta_{K3}^t) \\
R(\Delta\theta_{Kl}^t) &= R(\Delta\theta_{K2}^t)\,R(\Delta\theta_{K3}^t)\,R(\Delta\theta_{K1}^t) \\
R(\Delta\theta_{Kl}^t) &= R(\Delta\theta_{K1}^t)\,R(\Delta\theta_{K2}^t)\,R(\Delta\theta_{K3}^t) \\
R(\Delta\theta_{Kl}^t) &= R(\Delta\theta_{K1}^t)\,R(\Delta\theta_{K3}^t)\,R(\Delta\theta_{K2}^t)
\end{aligned}
\qquad (2.9)
$$

Each successive time step we can use a different order to calculate $R(\Delta\theta_{Kl}^t)$

2.2 Joint Modeling

A joint is used to connect different bodies to each other or to the ground. It defines the motion constraint between two points on different bodies. Joints constraints are shown in equation (2.10).

$$f(\{X\}) = 0 \qquad (2.10)$$

2.2.1 Connection Points

Each rigid body can have a number of connection points. A connection point is a point on the body where joints can be located. The position of a connection point *c* on rigid body *K* with respect to the global inertial reference frame (X_{c_i}) is given by:

$$X_{c_i} = X_{Ki} + R_{Kij} x_{c_j} \tag{2.11}$$

Where:

X_{Ki} : Position coordinates of the c.g. of rigid body K (body reference frame) with respect to the global inertial reference frame.

R_{Kij} : Rotation matrix of rigid body K

x_{c_j} : Position coordinates of point c with respect to the body reference frame. Those coordinates do not change with time since the body is rigid.

Figure 2.1 shows a random body in space with position vectors shown on it. A joint is defined by defining the relation between connection points.

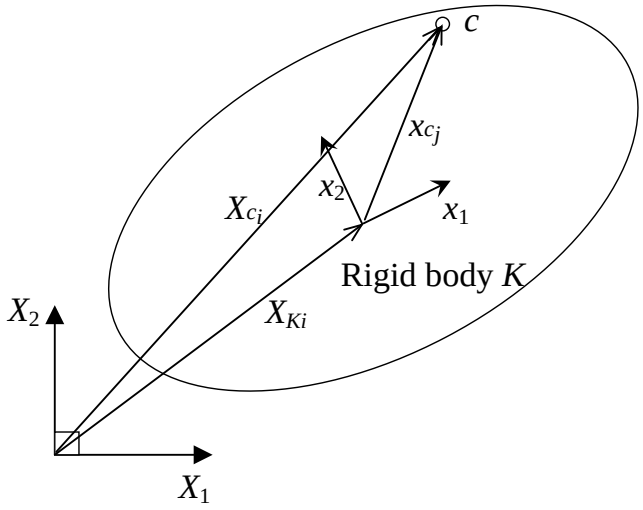

Figure 2.1 Rigid body in the space [19]

2.2.2 Spherical Joint

A spherical joint connects two points on two bodies. It constrains those two points such that they have the same translational coordinates relative to the global reference frame. Thus, a spherical joint between two connection points is defined as:

$$X_{c1_i}^t = X_{c2_i}^t \quad \Rightarrow \quad X_{c1_i}^t - X_{c2_i}^t = 0 \tag{2.12}$$

Where

$X_{c1_i}^t$: is the global position vector of the first point $c1$

$X_{c2_i}^t$: is the global position vector of the second point $c2$.

This constraint is of the form:

$$f(\{X\}) = 0 \tag{2.13}$$

A spherical joint leaves 3 relative rotational DOFs (degrees-of-freedom) between the two rigid bodies free and constrains 3 relative translational DOFs.

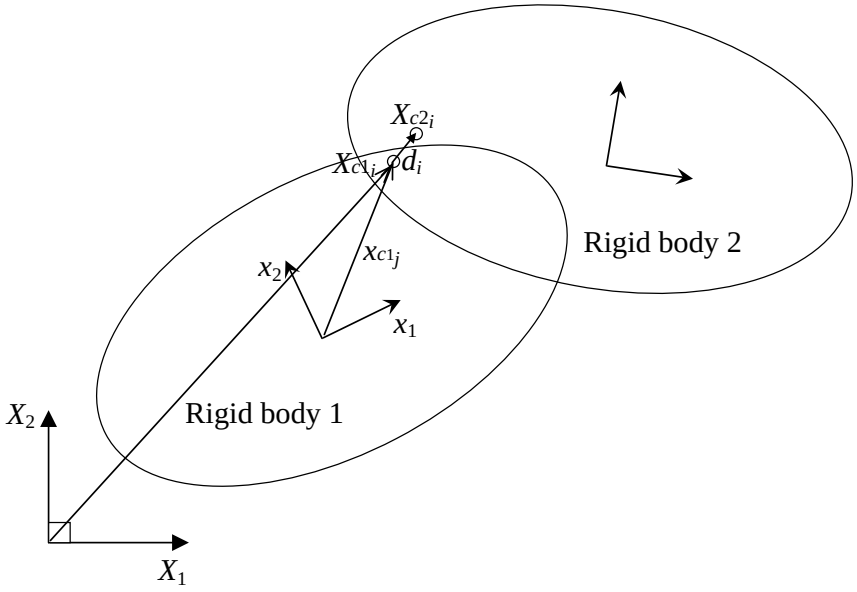

Figure 2.2 Two bodies connected with spherical joint

This constraint is imposed using the penalty technique as:

$$F_p = k_p d + c_p \, d_i \dot{d}_i \tag{2.14}$$

$$d_i = X_{c1_i}^t - X_{c2_i}^t \tag{2.15}$$

$$\dot{d}_i = \dot{X}_{c1_i^t} - \dot{X}_{c2_i^t} \tag{2.16}$$

$$d = \sqrt{d_1{}^2 + d_2{}^2 + d_3{}^2} \tag{2.17}$$

$$F_{pi} = \frac{F_p d_i}{d} \tag{2.18}$$

Where:

F_p : Penalty force magnitude.

k_p: Penalty spring stiffness.

c_p: Penalty damping.

d_i : Relative displacement vector between the points c1 and c2.

$\dot{d}_i$: Relative velocity vector between points c1 and c2.

d: Distance between points c1 and c2.

$\dot{X}_{c1_i^t}$: Global velocity vector for point c1.

$\dot{X}_{c2_i^t}$: Global velocity vector for point c2.

F_{pi} : Penalty reaction force on connection point c1. The penalty force on connection point c2 is to $-F_{pi}$

The joint penalty force is applied on the two connection points in opposite directions. This force tries to make points $X_{c1_i^t}$ and $X_{c2_i^t}$ coincident, i.e. it tries to impose the joint constraint $X_{c1_i^t} = X_{c2_i^t}$ or $d_i = X_{c1_i^t} - X_{c2_i^t} = 0$. A spherical joint is also called: “ball joint” or “ball-and-socket joint”. Each joint force is transferred to the c.g. of the corresponding rigid body using equation (2.19) and (2.20):

$$F_i = F_{p_i} \tag{2.19}$$

$$T_i = -(x_{c1_i} \times R_{ji} F_{p_i}) \quad \Leftrightarrow \quad \vec{T} = -(\vec{x}_{c1} \times R^T \vec{F}_p) \tag{2.20}$$

Where:

F_i: The force at the c.g. of the rigid body

T_i: The moment on the rigid body

x_{c1i}: The position of the point relative to the rigid body's frame

R_{ji}: The rigid body rotation matrix

The constraint forces are applied to the rigid bodies (nodes) by assembling them into the global forces F_{Ki}^{t}. Also, the constraint moments are applied to the rigid bodies by assembling them into the global torques T_{Ki}^{t}.

2.2.3 Revolute Joint

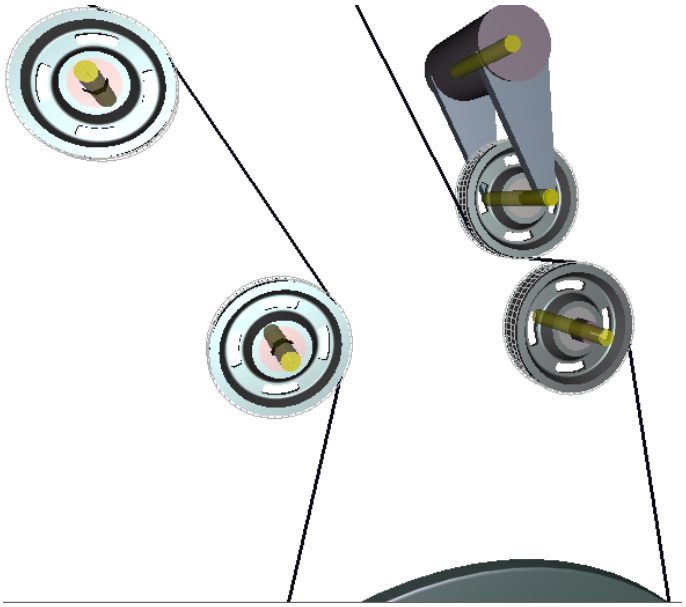

Figure 2.3 Revolute joint is shown as yellow cylinders at the axe of rotation

A revolute joint connects two rigid bodies in which it restricts 5 degrees of freedom and allowing only one rotational degree of freedom between the two bodies. Revolute joints are modeled by placing two spherical joints along a line. It's used to model all kinds of axes of rotation and some rotational shafts, see Figure 2.3. It is also called "hinge joint".

2.3 Contact Model

The contact between two bodies is modeled as normal contact between points of one body and the surface of the second one. The normal constraint is defined using penalty technique and is defined as shown in equation (2.21) [19].

$$f(\{X\}) \geq 0 \tag{2.21}$$

The first step is to find the position and velocity of each contact point (say contact point *c*) using Equations (2.22) and (2.23):

$$X_{c_i}^{\ t} = X_{Ki}^{\ t} + R_{Kij}^{t} x_{c_j} \quad \Leftrightarrow \quad \begin{Bmatrix} X_{K1} \\ X_{K2} \\ X_{K3} \end{Bmatrix} = \begin{Bmatrix} X_{0_1} \\ X_{0_2} \\ X_{0_3} \end{Bmatrix} + \begin{bmatrix} R_{11} & R_{12} & R_{13} \\ R_{21} & R_{22} & R_{23} \\ R_{31} & R_{32} & R_{33} \end{bmatrix} \begin{Bmatrix} x_{K1} \\ x_{K2} \\ x_{K3} \end{Bmatrix} \tag{2.22}$$

$$\dot{X}_{c_i}^{\ t} = \dot{X}_{Ki}^{\ t} + R_{Kij}^{t} \left(\{\dot{\theta}_K^t\} \times \{x_c\} \right)_j \quad \Leftrightarrow \begin{Bmatrix} \dot{X}_{K1} \\ \dot{X}_{K2} \\ \dot{X}_{K3} \end{Bmatrix} = \begin{Bmatrix} \dot{X}_{0_1} \\ \dot{X}_{0_2} \\ \dot{X}_{0_3} \end{Bmatrix} + [R] \left(\begin{Bmatrix} \dot{\theta}_1 \\ \dot{\theta}_2 \\ \dot{\theta}_3 \end{Bmatrix} \times \begin{Bmatrix} x_{K1} \\ x_{K2} \\ x_{K3} \end{Bmatrix} \right) \tag{2.23}$$

Where:

x_{c_j} : Coordinates of contact point *c* with respect to the local frame of the first body.

$X_{c_i}^{\ t}$: Position coordinates of contact point *c* with respect to the global frame at time *t*.

$X_{Ki}^{\ t}$: Coordinates of the center of the first body frame with respect to the global frame at time *t*.

R_{Kij}^{t} : Rotation matrix of the first rigid body at time *t*.

$\dot{X}_{c_i}^{\ t}$: Velocity components of contact point *c* with respect to the global reference frame at time *t*.

$\dot{X}_{Ki}^{\ t}$: Velocity components of the center of the first body frame with respect to the global frame at time *t*.

$\dot{\theta}_{Kk}^{t}$: Angular velocity components of the first body at time *t*.

Figure 2.4 shows the coordinates notation for a rigid body in the global and local frame of reference. It also shows the relation between them.

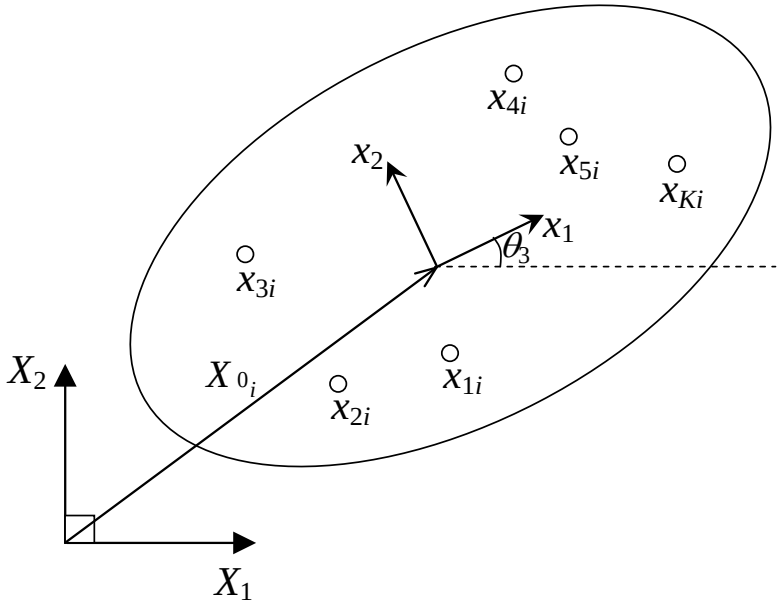

Figure 2.4 Rigid body coordinates

The normal and the tangential forces are calculated at the contact point. The total force F_c at each contact point is the summation of both of normal and tangential force on the point *c*. using Equation (2.19) and (2.20) F_c is transferred as a force and a moment to the center of the rigid body. Using the same equations, an equal in magnitude but opposite in direction force is transferred to the other body.

2.3.1 Normal Contact Model Using Penalty Technique

When a point on the first body penetrates the surface of the second body, a normal reaction force (F_{normal}) is developed on the body. This force has a magnitude proportional to the distance penetrated in the surface as well as the velocity of penetration

and is calculated in Equation (2.24) through (2.26). Figure 2.5 illustrates the penetration of a node on a rigid body into the surface of the other rigid body.

$$F_{normal} = Ak_p d + A\begin{cases} c_p \dot{d} & \dot{d} \geq 0 \\ s_p c_p \dot{d} & \dot{d} < 0 \end{cases} \tag{2.24}$$

$$\dot{d} = v_i n_i \tag{2.25}$$

$$v_{n_i} = \dot{d} n_i \tag{2.26}$$

Where:

A: Area of the rectangle associated with the contact point

k_p and c_p: Penalty stiffness and damping coefficient per unit area

d: Closest distance between the contact point and the contact surface

$\dot{d}$: Signed time rate of change of d

S_p: Separation damping factor between 0 and 1 which determines the amount of sticking between the contact point and the contact surface at the contact point (leaving the body)

$\vec{n}$: Unit vector normal to the surface

$\vec{v}_i$: The relative velocity vector between the contact point and the contact surface

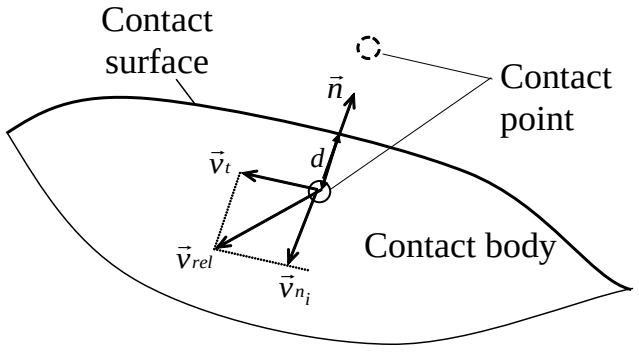

Figure 2.5 Contact surface and contact node [20]

2.3.2 Friction Model (Asperity-Friction)

The surface of a smooth rigid body looks rough with peaks and valleys if examined under a microscope. These peaks are called asperities, see Figure 2.6. Asperities on two moving surfaces, in contact with each other, interlock together developing a force which opposes motion. This force is called *friction force* or *asperity force*. To slide one body over the other, a large enough force should be applied to overcome the force developed due to asperity interlock.

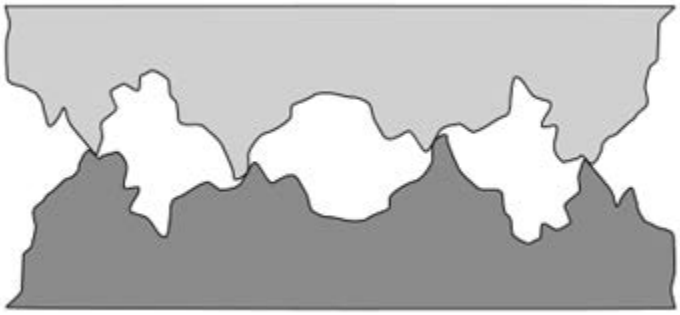

Figure 2.6 Surface asperities magnified for illustration

2.3.2.1 Asperity-Friction Model

The tangential force ($F_{tangent}$) is calculated using the normal force and the asperity friction model. The model approximates asperity friction by transmitting a tangential friction force vector between two bodies at the point of contact to represent the friction forces between two rough surfaces in contact arise due to the interaction of the surface asperities (F_{tj}). It is given by equation (2.27).

$$F_{ti} = F_{tangent}\, t_i \tag{2.27}$$

The asperity-spring friction model presented in Ref. [20] is used to model contact friction. The model consists of a piece-wise linear velocity-dependent approximate Coulomb friction element in parallel with a variable anchor point spring. When two surfaces are in static contact, the surface asperities act like tangential springs. When a

tangential force is applied, the springs elastically deform and pull the surfaces to their original position. If the tangential force is large enough, the surface asperities yield (i.e. the springs break) allowing sliding to occur between the two surfaces [20]. The breakaway force is proportional to the normal contact pressure. In addition, when the two surfaces are sliding past each other, the asperities provide resistance to the motion that is a function of the sliding velocity and acceleration, and the normal contact pressure.

2.4 Beam Element

The belt will be modeled using the three-node torsional spring beam finite elements presented in Ref. [16]. The beam element connects three nodes and consists of three sub-elements: two truss elements each connecting two-nodes to model the axial response of the beam and a torsional spring connecting the three nodes to model the bending response of the beam.

The truss sub-element connects two nodes. Due to the stiffness and damping of the element, it acts like a spring. The internal force in a truss element is calculated as shown in the following equation [18].

$$F = \frac{EA}{l_0}(l - l_0) + \frac{CA}{l_0}\dot{l} \tag{2.28}$$

Where:

E: The Young's Modulus

C: The Damping Modulus

A: The effective cross-sectional area

l: The current length, of the truss

$\dot{l}$: Rate of change in element length

l_0: The un-stretched length of the truss.

The three-node torsional spring sub-element has 3 point mass type nodes that have translational DOFs only. Figure 2.7(a) shows a beam element connects the point p_1

(mid-point of $\overline{12}$) to point p_2 (mid-point of $\overline{23}$). The beam element has a slope which is tangent to$\overline{12}$ at the point p_1, while it is tangent to $\overline{23}$ at the point p_2. The beam element consists of two truss sub-elements ($\overline{p_1 2}$) and $\overline{2p_2}$) and a torsional-spring bending sub-element ($p_1 \hat{2} p_2$). Equation (2.28) calculates the internal force in a sub-truss element [18]. The element reaction moment is given by [18]:

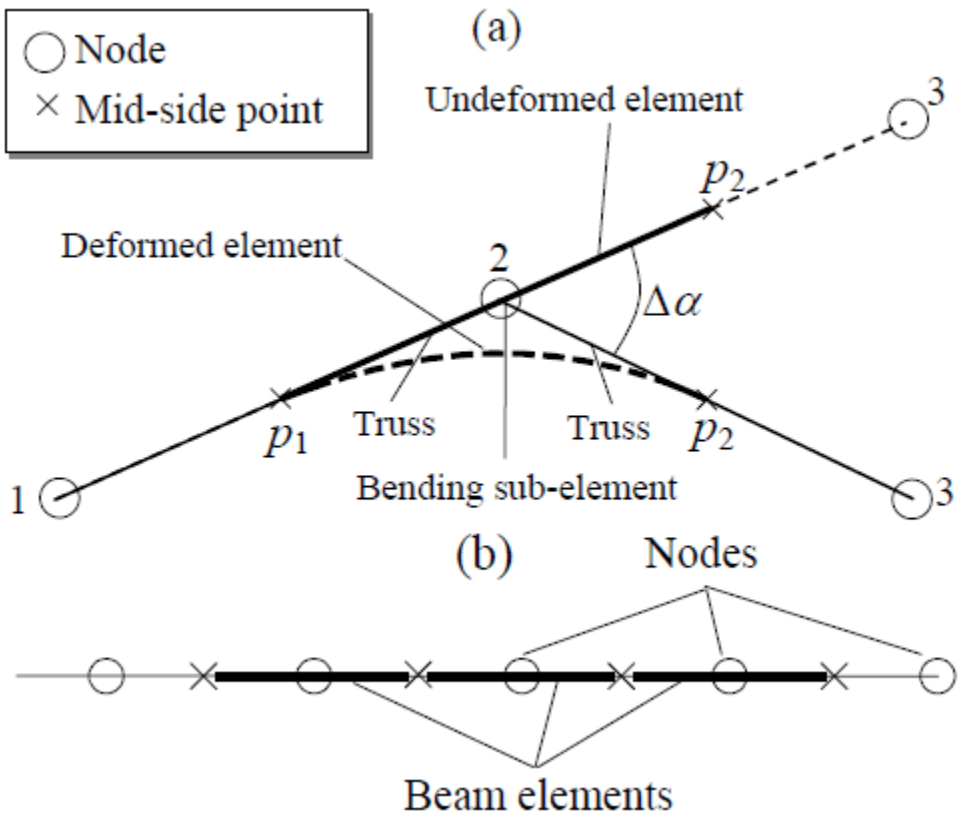

Figure 2.7 (a) Three-noded beam element (b) Finite element discretization of a beam using 3-nided beam element [18]

$$M = \frac{EI}{L_0}\Delta\alpha + \frac{CI}{L_0}\dot{\alpha} \tag{2.29}$$

Where:

E: The Young's Modulus

C: The Damping Modulus

I: The effective cross sectional moment of inertia

L_0: The un-stretched length of the truss of the bending element

$\Delta\alpha$: The change in angle between $\overline{p_1 2}$ and $\overline{2p_2}$

$\Delta\dot{\alpha}$: The rate of change in angle between $\overline{p_1 2}$ and $\overline{2p_2}$

Figure 2.7(b) shows how a beam is discretized using the 3-noded beam element. Note that this is a 1-D beam element that has no torsional response along the axis of the beam. It is also assumed that the beam has equal moments of inertia of the cross-section around two perpendicular cross-section axes. This is not true for belts; however, since the belt-problem is two-dimensional we are only need to accurately model the belt bending behavior around one axis (parallel to the axes of the pulleys).

2.5 Explicit Solution Procedure

The solution fields for modeling multibody systems are defined at the model rigid bodies. Note that a rigid body is modeled as one node. These solutions fields are:

- Global translational position vectors X^t_{Ki}
- Global translational velocity vectors $\dot{X}^t_{Ki}$
- Global translational acceleration vectors $\ddot{X}^t_{Ki}$
- Global → local rotation matrices R^t_{Kij}
- Local body rotational velocity vectors $\dot{\theta}^t_{Kj}$
- Local body rotational acceleration vectors $\ddot{\theta}^t_{Kj}$

Where

K = 1 to N

N: total number of rigid bodies.

An explicit predictor corrector solution procedure based on the trapezoidal integration rule for time is used. The explicit time integration solution procedure predicts the time evolution of the above response quantities.

1. Set $t = 0$ and set the initial conditions for all the rigid bodies (nodes) are set. Those are:

$$X_{Ki}^{0},\ \dot{X}_{Ki}^{0},\ \ddot{X}_{Ki}^{0},\ R_{Kij}^{0},\ \dot{\theta}_{Kj}^{0},\ \ddot{\theta}_{Kj}^{0}$$

2. Increment time: $t = t + \Delta t$
3. Set the nodal values at the last time step to be equal to the current nodal values for all solution fields.

$$X_{Ki}^{t} = X_{Ki}^{t-\Delta t} \qquad \dot{X}_{Ki}^{t} = \dot{X}_{Ki}^{t-\Delta t} \qquad \ddot{X}_{Ki}^{t} = \ddot{X}_{Ki}^{t-\Delta t}$$

$$R_{Kij}^{t} = R_{Kij}^{t-\Delta t} \qquad \dot{\theta}_{Kj}^{t} = \dot{\theta}_{Kj}^{t-\Delta t} \qquad \ddot{\theta}_{Kj}^{t} = \ddot{\theta}_{Kj}^{t-\Delta t}$$

4. Perform 2 iterations (predictor iteration and corrector iteration) of the following steps.
    a. Initialize the nodal forces and moments to zero.

$$F_{Ki}^{t} = 0 \qquad T_{Ki}^{t} = 0$$

    b. Calculate the nodal forces and moments produced by all elements, joints and contact forces and add (assemble) those forces and moments to F_{Ki}^{t} and T_{Ki}^{t}. Note that this is the most computationally expensive step in the solution procedure.
    c. Calculate $\ddot{X}_{Ki}^{t}$ and $\ddot{\theta}_{Kj}^{t}$ using Equations (6.3)and (2.2) respectively:

$$\ddot{X}_{\mathrm{Ki}}^{\mathrm{t}} = \frac{F_{Ki}^{t}}{M_K}$$

$$\ddot{\theta}_{Kj}^{t} = I_{Kij}^{-1}\left(T_{Ki}^{t} - \left(\dot{\theta}_{Kk}^{t} \times (I_{Kjl}\dot{\theta}_{Kl}^{t})\right)_{Ki}\right)$$

d. Use the trapezoidal time integration formulas Equations (2.3) through Equation (2.7) to calculate $\dot{X}_{Ki}^{t}$, X_{Ki}^{t}, $\dot{\theta}_{Kj}^{t}$ and R_{Kij}^{t}:

$$\dot{X}_{Kj}^{t} = \dot{X}_{Kj}^{t-\Delta t} + 0.5\,\Delta t\,(\ddot{X}_{Kj}^{t} + \ddot{X}_{Kj}^{t-\Delta t})$$

$$X_{Kj}^{t} = X_{Kj}^{t-\Delta t} + 0.5\,\Delta t\,(\dot{X}_{Kj}^{t} + \dot{X}_{Kj}^{t-\Delta t})$$

$$\dot{\theta}_{Kj}^{t} = \dot{\theta}_{Kj}^{t-\Delta t} + 0.5\,\Delta t\,(\ddot{\theta}_{Kj}^{t} + \ddot{\theta}_{Kj}^{t-\Delta t})$$

$$\Delta\theta_{Kj}^{t} = 0.5\,\Delta t\,(\dot{\theta}_{Kj}^{t} + \dot{\theta}_{Kj}^{t-\Delta t})$$

$$R_{Kij}^{t} = R_{Kik}^{t-\Delta t}\, R_{Kkj}(\Delta\theta_{Kl}^{t})$$

$R_{Kkj}(\Delta\theta_{Kl}^{t})$ is calculated using Equation (2.8) and (2.9)

e. Execute the prescribed motion constraints which set the nodal value(s) to prescribed values.

5. Go to step 2.

3. NUMERICAL MODEL DESCRIPTION

Figure 3.1 shows the belt-drive model that was built and simulated using the **DIS (*Dynamic Interactions Simulator)*** multibody dynamic software.

3.1 Components

The model consists of a belt-drive operating on an internal combustion engine as shown in Figure 3.1. This belt-drive is designed to add the torque produced by a turbine in Rankin cycle working on exhaust waste heat recovery to the torque produced by the internal combustion engine. The model consists of pulleys, shafts, gears, rotational tensioner and a belt which are discussed below in more details. Contacts between the belt and the pulleys as well as the contact between gears are modeled using the penalty technique with a penalty spring/damper. The friction between the belt and the pulleys is modeled using the asperity spring friction model to approximate coulomb friction.

1- The Ground

The ground is a hypothetical component that has a **ground constraint** (i.e. translational and rotational velocity and acceleration are equal to *zero* at all time). All pulleys, gears and the tensioner arm are connected to the ground using revolute joints. The ground represents the vehicle/engine frame.

2- The Crank Pulley (Fly Wheel)

The flywheel of the internal combustion engine is mounted on the crankshaft and it includes the crank pulley (see Figure 3.1). The engine torque is applied to the crankshaft. The crank pulley is modeled as a rigid body with a cylindrical contact surface. It is connected to the ground using a revolute joint.

3- The Turbine

The turbine appears on the top left of Figure 3.1. The turbine drives a 19 teeth pinion gear (referred to as **"the pinion"** in the rest of this thesis).

4- The Pinion

Both the pinion and the shaft are modeled as one rigid body. A torsional spring-damper between the shaft and the turbine is used to model the shaft torsional compliance.

5- The Drive gear

The pinion drives a bigger gear (modeled as a rigid body) that has 191 teeth (i.e. the gear ratio is 19:191) for speed reduction and torque magnification. This gear will be referred to as "**drive gear**".

6- The Drive Pulley

The drive gear is connected to a pulley through a shaft (both the pulley and shaft are modeled as rigid bodies). The pulley and the shaft will be referred to as "**drive pulley**" and "**drive shaft**" respectively.

7- The Drive Shaft

The drive shaft is modeled as a rigid body with a torsional spring-damper at each end to account for the shaft stiffness. The two torsional spring-dampers are considered to be connected in series and hence, the series spring summation rule is employed to

calculate the equivalent rotational stiffness and damping of both springs, which are equal to the equivalent stiffness and damping of the shaft.

8- The Tensioner

A rotational tensioner is used to maintain the belt tension and to absorb belt slack, thus reducing belt slip and vibrations and increasing the power transmission efficiency. So, the tensioner pulley is positioned on the low tension (slack) side of the belt. Note that the turbine is the driver, thus the low tension span is the right hand side span (see Figure 3.1).

9- The Idlers

Three idler pulleys are added to the belt drive to increase the belt wrapping angles around the crank and drive pulleys (which increase the belt traction on the pulleys) and to decrease the length of belt free spans (which decreases belt vibration). All Idlers are modeled as rigid bodies and are connected to the ground by a revolute joint.

10- The Belt

A serpentine belt is running over the pulleys to couple torque between the turbine (through the drive pulley) and the crank. The belt is modeled using beam elements with the element length set to 5mm. As stated before, the friction between the belt and the pulley is modeled using asperity spring friction technique to approximate coulomb friction. The belt parameters (axial stiffness/damping, bending stiffness/damping and mass per unit length) are chosen to match the specifications of the belt **8Pk2630**.

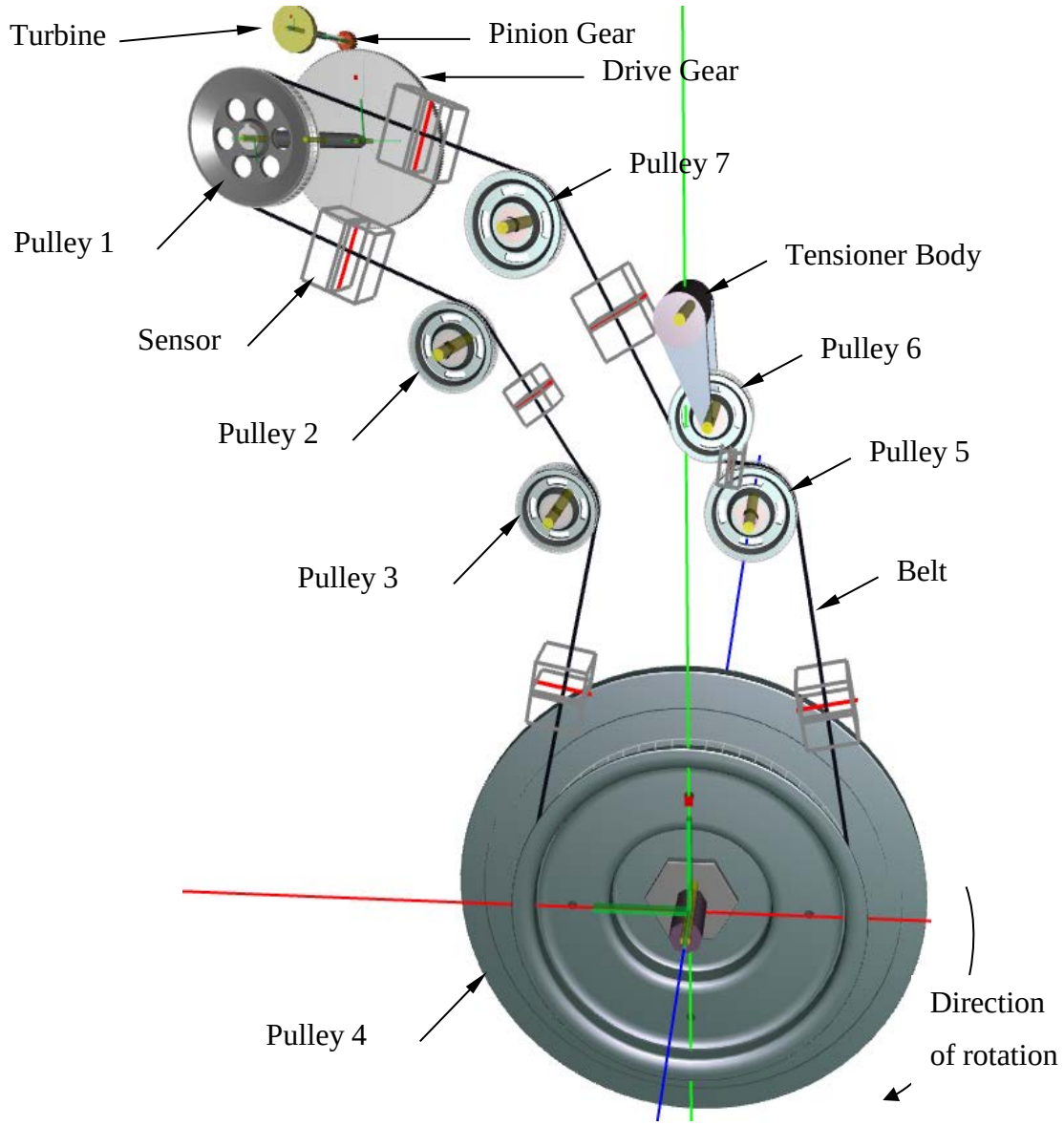

Figure 3.1 The belt drive Model

11- Sensors

Sensors are virtual box-shaped sensing elements that can read information of the belt elements inside it. Sensors are placed on each belt span (see Figure 3.1) to measure the belt tension, and the transverse belt deflection (i.e. deflection of the belt normal to the belt span).

3.2 Geometry and Physical Properties

Table 3.1 shows the geometric properties of the belt drive (coordinates of the centers of the pulleys and the tensioner and the pitch diameters of the pulleys).

Table 3.2 shows the other physical properties of the belt drive. Those include: moment of inertia of the pulleys, mass of the tensioner pulley, mass and c.g. location of the tensioner, torsional stiffness/damping/friction of the tensioner, initial tensioner torque, drive and driven shafts torsional stiffness/damping, gear teeth stiffness/damping, gear tooth backlash, belt axial stiffness/damping, belt bending stiffness/damping, belt mass per unit length and coefficient of friction between the belt and the pulleys. Some of the model properties are hard to measure, such as the tensioner arm viscous damping and tensioner arm friction torque; those parameters were tuned so that the numerical simulation results match the experimental results. An initial estimate was used for each tuning parameter, and then the value was increased or decreased until the best match was obtained. The tuning parameters are:

- Torsional viscous damping coefficient of the tensioner
- Friction torque of the tensioner
- Belt bending damping
- Belt bending stiffness
- Belt axial damping
- Coefficient of friction between belt and pulley

Plots showing the numerical results and experimental results are shown in Section 3.5. The plots show excellent match between both results. Table 3.2 shows the final values for the model parameters that are used in the model.

Table 3.1 Layout and geometry of the pulleys and tensioner

Pulley #	Description	X-Coordinate (mm)	Y- Coordinate (mm)	Pitch diameter (mm)
1	Drive Pulley	-407.90	722.60	104.4
2	Idler	-210.00	540.00	74
3	Idler	-120.00	400.00	74
4	Crank	0.00	0.00	338.3
5	Idler	60.00	400.00	82.5
6	Tensioner Pulley	23.57	483.14	74
7	Idler	-148.00	640.00	82.5
Tensioner pivot	Tensioner arm pivot	0.00	570.00	N/A

Table 3.2 Model parameters

Crank Pulley	
Inertia ($kg.m^2$)	0.1269
Idler Pulley 5	
Inertia ($kg.m^2$)	0.000823
Tensioner Pulley	
Mass (Kg)	1.135
Inertia ($kg.m^2$)	0.000819
Tensioner body	
Mass (Kg)	0.64378
Inertia ($kg.m^2$)	0.00287
Rotational stiffness (Nm/rad)	26.22
Rotational Damping (N.m.sec/rad)	0
Friction moment (N.m)	3.16
C.G Location from the pivot along the axis of symmetry to the tensioner pulley (m)	0.025
Initial torque (N)	45.368
Arm length (m)	0.09
Idler pulley 7	
Inertia ($kg.m^2$)	0.000823
Drive pulley	
Inertia ($kg.m^2$)	0.004244
Idler Pulley2	
Inertia ($kg.m^2$)	0.00102947
Idler Pulley3	
Inertia ($kg.m^2$)	0.00102947

Table 3.2 Continued

Drive Shaft	
Inertia (kg.m2)	0.0088217
Stiffness (N/m)	5674
Damping (N.sec/m)	45
Driven Gear	
Inertia ($kg.m^2$)	0.011414
Turbine	
Inertia ($kg.m^2$)	6.56E-05
Turbine Shaft with Pinion	
Inertia ($kg.m^2$)	3.00E-06
Stiffness (N/m)	1442
Damping (N.m/sec)	4
Pinion tooth Stiffness (N/m)	2.00E+13
Pinion tooth Damping (N.m/sec)	8.00E+06
Tooth backlash (m)	5.00E-05
Belt	
Axial stiffness (EA) (N)	140,563
Axial Damping (CA) (N.sec)	10
Bending Damping (CI) ($N.m^2.sec$)	5.00E-05
Mass per unit length (Kg/m)	0.4

3.3 Dynamics

3.3.1 Crankshaft Angular Velocity

The numerical model uses the crank shaft angular velocity versus time as an input to the system. There are six ranges of operation at 5 different engine mean angular velocities. These ranges and their corresponding mean angular velocity are shown in Table 3.3. The exact crank angular velocity is measured experimentally and was used as an input to the numerical model. The numerical simulation was run for **20 seconds** simulating the six operation ranges. Figure 3.2 shows the crank angular velocity profile. Intentionally, **0.3 seconds** in the beginning of simulation was set to 0 RPM to allow the belt drive to reach the initial static configuration, followed by **0.7 seconds** to ramp the crank angular velocity from 0 RPM to 700 RPM to start simulation of the idle engine operating speed. A PID controller is used to control the desired angular velocity of the crank shaft. Each of the six operating ranges is simulated for **3 seconds**. There is **0.2 seconds** interval between each operating range to allow the system to ramp up between different mean angular velocities. To avoid the effect to transients, only the last second of each range is compared to the experimental results.

Table 3.3 Mean crank RPM for different ranges of operation

Operation Range	**RPM**
Idle operation	700
A100	1250
B100	1500
C100	1800
Unloaded Up	2100
Unloaded Down	2100

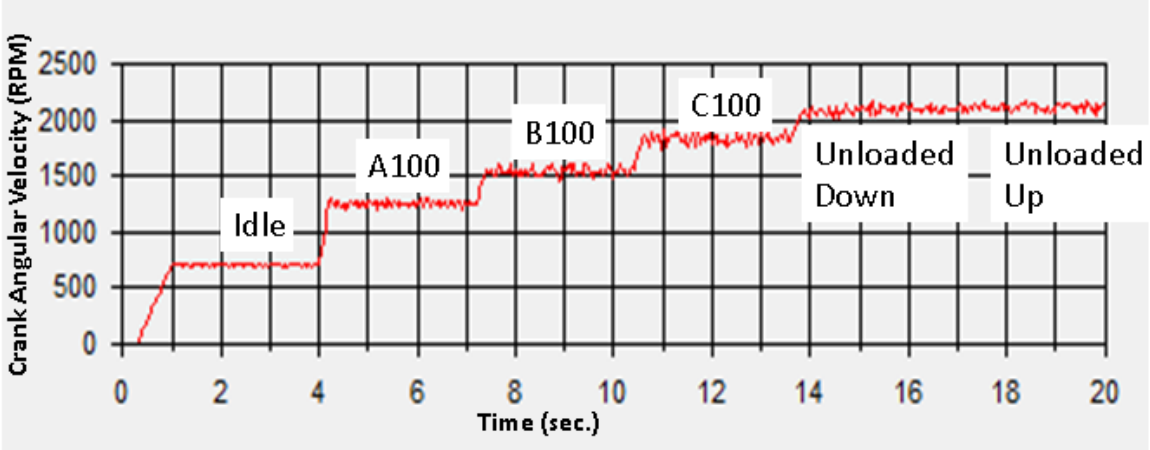

Figure 3.2 Crank angular velocity profile used as an input to the numerical model. Note the crank is rotation in the clockwise direction.

3.3.2 Turbine Torque

Turbine torque comes from the output power of the Rankin cycle at the turbine shaft. The turbine torque depends on many parameters including engine load, engine speed, temperature of the exhaust and mass flow rate of the exhaust. In the numerical model the turbine torque was assumed to be a function of only the turbine angular velocity. Figure 3.3 and Table 3.4 show the profile of the turbine torque versus the turbine angular velocity in rpm. The negative sign indicate that the torque is in the clockwise direction. The turbine torque acts in the same direction as the engine rotation so that it adds to the engine torque, thus increasing the effective engine power (with no additional fuel consumption). Turbine torque is used as another input to the system.

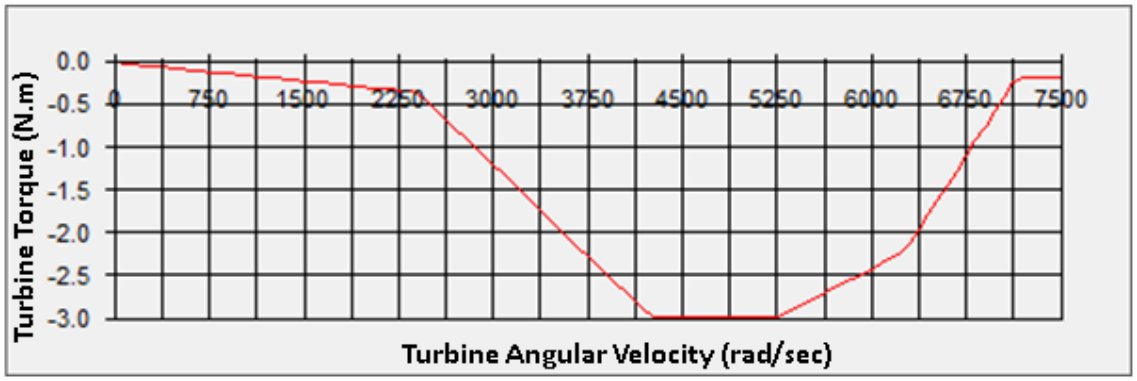

Figure 3.3 Turbine torque profile

Table 3.4 Turbine torque Vs. turbine RPM

Turbine RPM	Turbine Shaft Torque (Nm)		Turbine RPM	Turbine Shaft Torque (Nm)
0	0		52120	26
22802	3		58635	24
29317	10		59771	22
32575	15		60263	12
35832	20		65150	5
39090	25		68265	2
40758	30		68407	2
45605	30		69227	1
50310	30			

3.4 Experimental Results

A test rig was built by Cummins Inc. (a leading manufacturer of diesel engines). The crank angular velocity profile used in the model was obtained from the test rig. The input turbine torque profile (Table 3.4) was first roughly estimated from the test rig, and then the profile was tuned in the numerical model. Output quantities of the experiment were chosen to be the drive shaft angular velocity and the drive shaft torque. Results were measured using high fidelity measuring instruments. More information about the test rig was not available due to confidentiality restrictions of Cummins, Inc..

3.5 Numerical Results

Table 3.5 shows a summary of the finite element model used to model the belt-drive. The finite element numerical model has 526 nodes. They consists of 1 node for the ground object (i.e. engine frame), 7 nodes represents the pulleys, 1 node for the tensioner arm, 2 nodes for the turbine and drive shafts, 1 node for the drive gear, 1 node for the turbine and 513 nodes for the belt elements. The model was solved using trapezoidal explicit numerical integration with predictor corrector technique using a time step of 3×10^{-7} seconds. The simulation time was 20 seconds and it was solved in 14.8 hours using an Intel(R) Core(TM) i7-2700k CPU @ 3.50 GHz with 8.00 GB of RAM.

Table 3.5 Numerical solution parameters

Elemetn length	0.005 m
No. of belt elements	513
No. of pulleys	7
No. of Gears	2
Simulation time (sec.)	20
Numerical integration Time Step (sec.)	3×10^{-7}
Computational times (hours)	14.85

3.6 Comparison between Experimental and Numerical Results

The numerical model was simulated using the DIS code, which uses an explicit numerical integration technique to solve equations of motion. The experiment was run on the numerical model for 20 seconds with angular velocity profile to the crank shaft shown in Figure 3.2. The drive shaft angular velocity and drive shaft torque (which were agreed to be the system outputs) were compared with the experimental results. Each output was compared for each range of operation, and results were plotted in both time domain and frequency domain. The time domain plot gives sense of the behavior of the system and the overall shape of the signal. The frequency domain shows the main frequencies of the system and the magnitude of vibration at those frequencies. The frequency domain graphs were calculated using the Fast Fourier Transform (FFT) technique. Plots of the input crank angular velocity, drive shaft angular velocity and drive shaft torque are shown in Figure 3.5 through Figure 3.21. As shown in the plots, idle, A100, B100 and C100 numerical results show excellent agreement with the experimental results. The code accurately predicted at least the first 3 main frequencies. The difference between the amplitudes of the main frequencies in the experiment and simulation in the idle operation was less than 10%. While the difference between the main frequencies in the experiment and simulation for the A100 operation range was about 15%. In the B100 and C100 operation ranges the difference between the experiment and simulation in the amplitudes of the 2 main frequencies was less than 15%, while the third main frequency error was 50%. The other two ranges, namely Unloaded up and Unloaded down show more frequencies than the numerical results. By investigating the frequency domain graph of the input crank shaft angular velocity as a function of vibration amplitude it was found that the number of exciting frequencies in the crank shaft angular velocity is much less than the number of excited frequencies in the response (drive shaft angular velocity and torque). This means that there has to be another source of excitation to the system. It was concluded that, most likely, the other source of excitation is structural excitation to the test rig. Such excitation cannot be reproduced by the numerical model unless the structure was modeled, which was not the focus of this work. Hence, the results are considered to

be an acceptable match. Thus, overall, the model showed enough fidelity to be confidently used in further investigation.

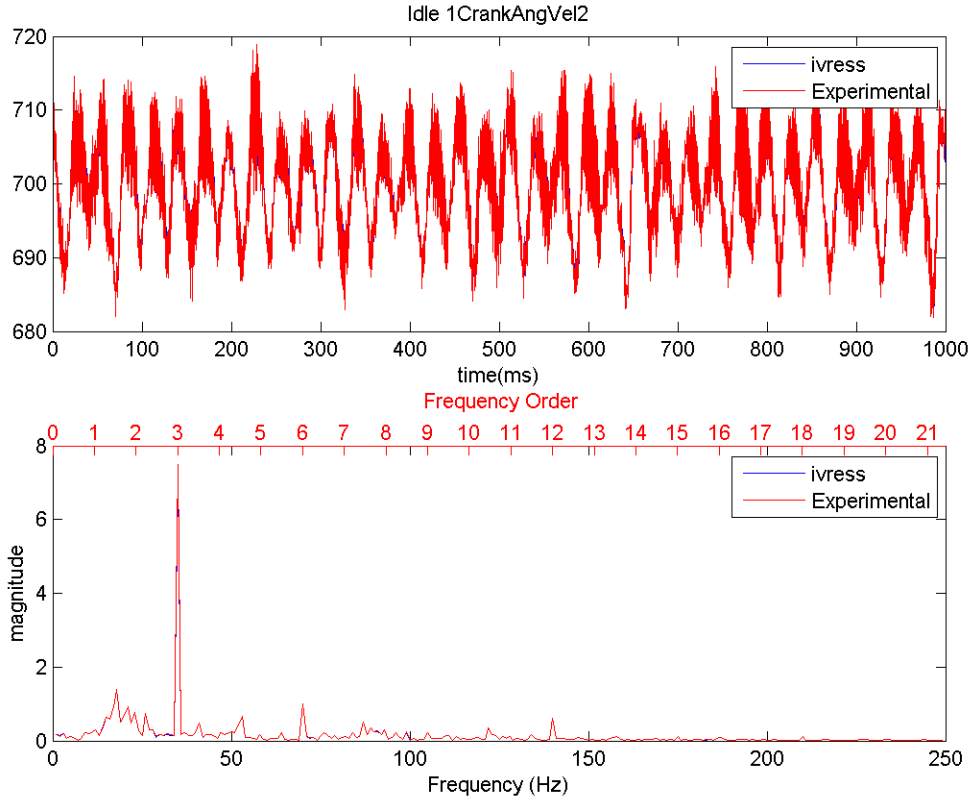

Figure 3.4 Crank angular velocity comparison for the idle operation range

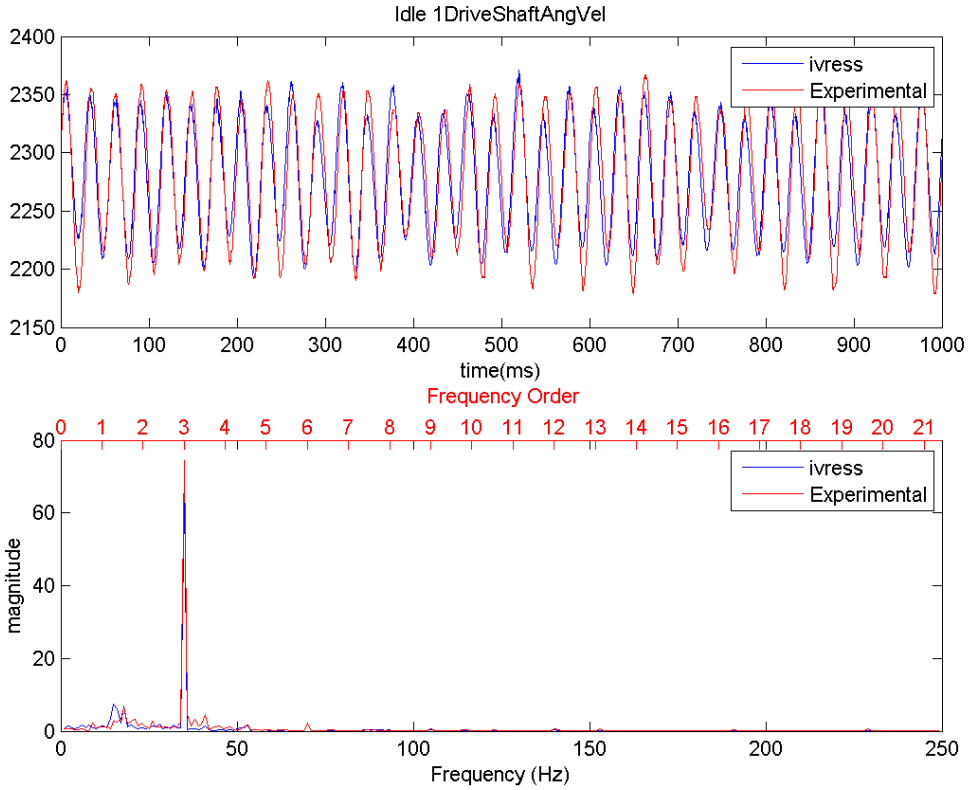

Figure 3.5 Drive shaft angular velocity (RPM) comparison for the idle operation range

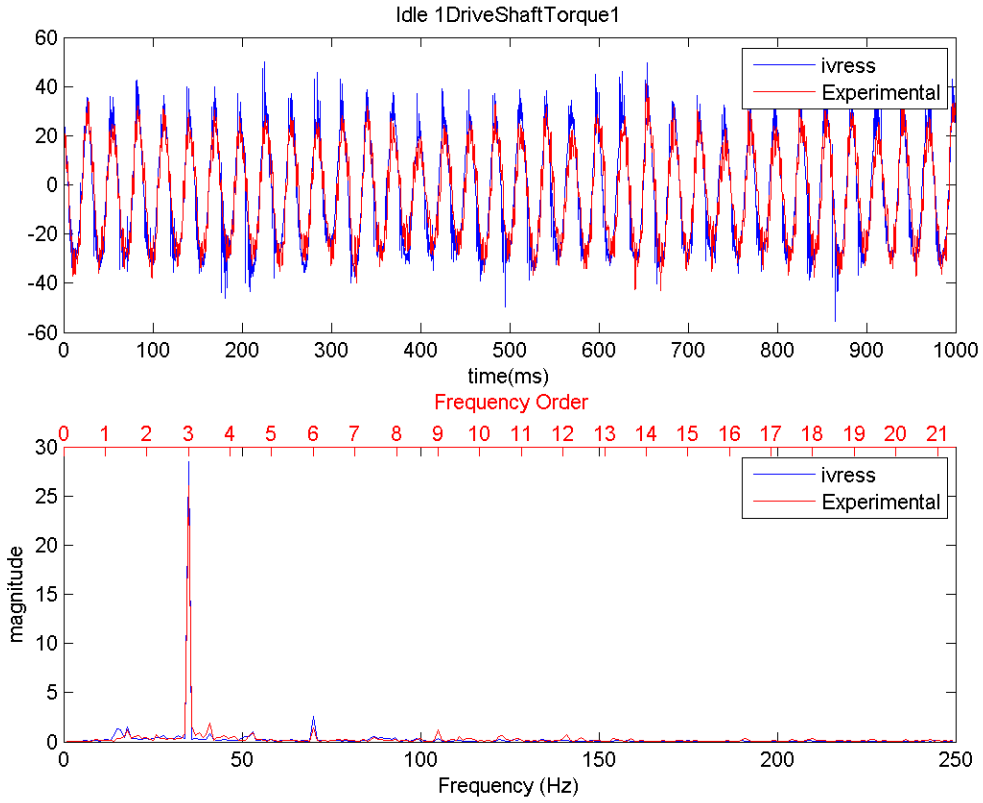

Figure 3.6 Drive shaft torque (N.m) comparison for the idle operation range

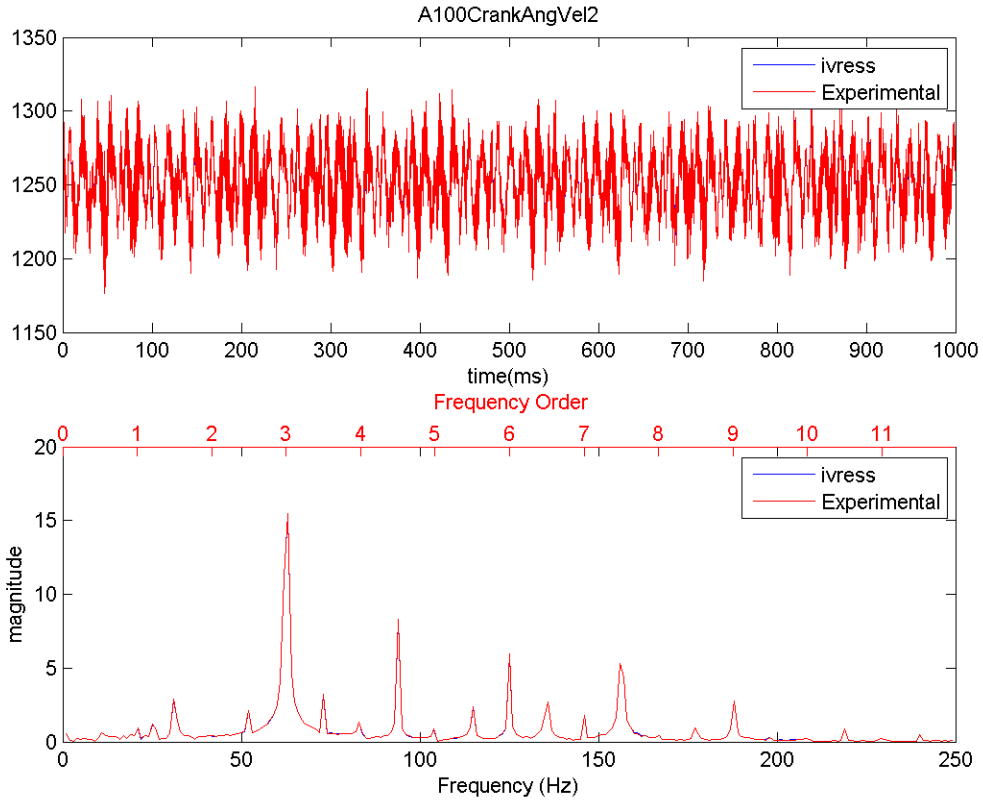

Figure 3.7 Crank angular velocity comparison for the A100 operation range

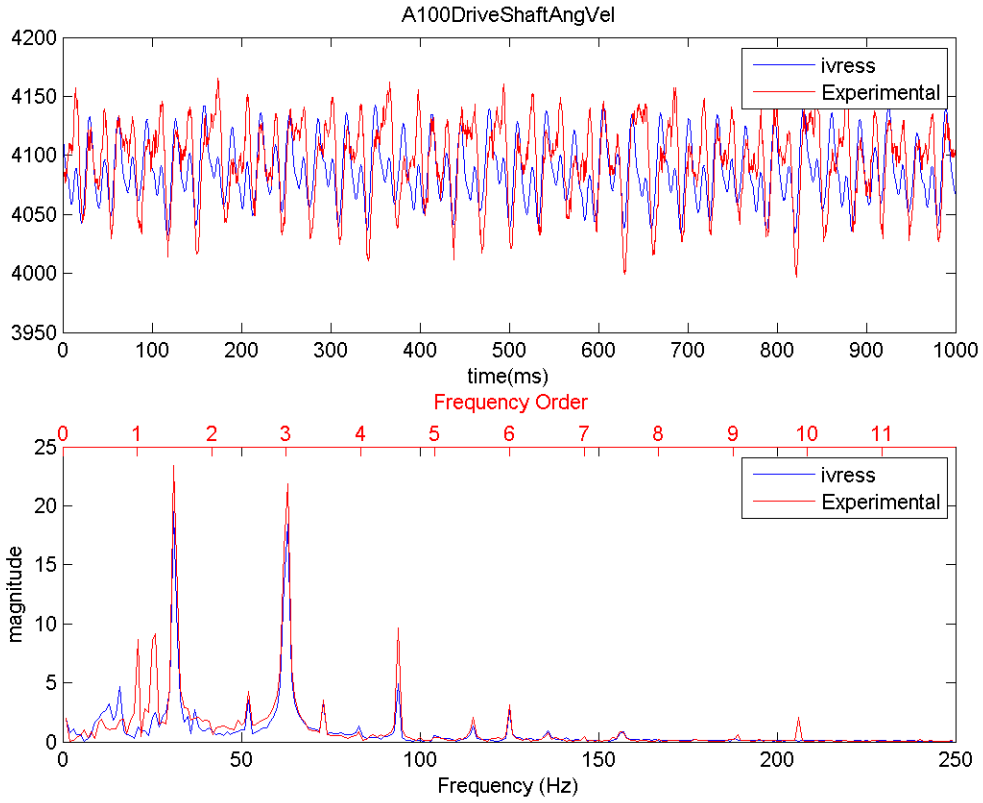

Figure 3.8 Drive shaft angular velocity (RPM) comparison for the A100 operation range

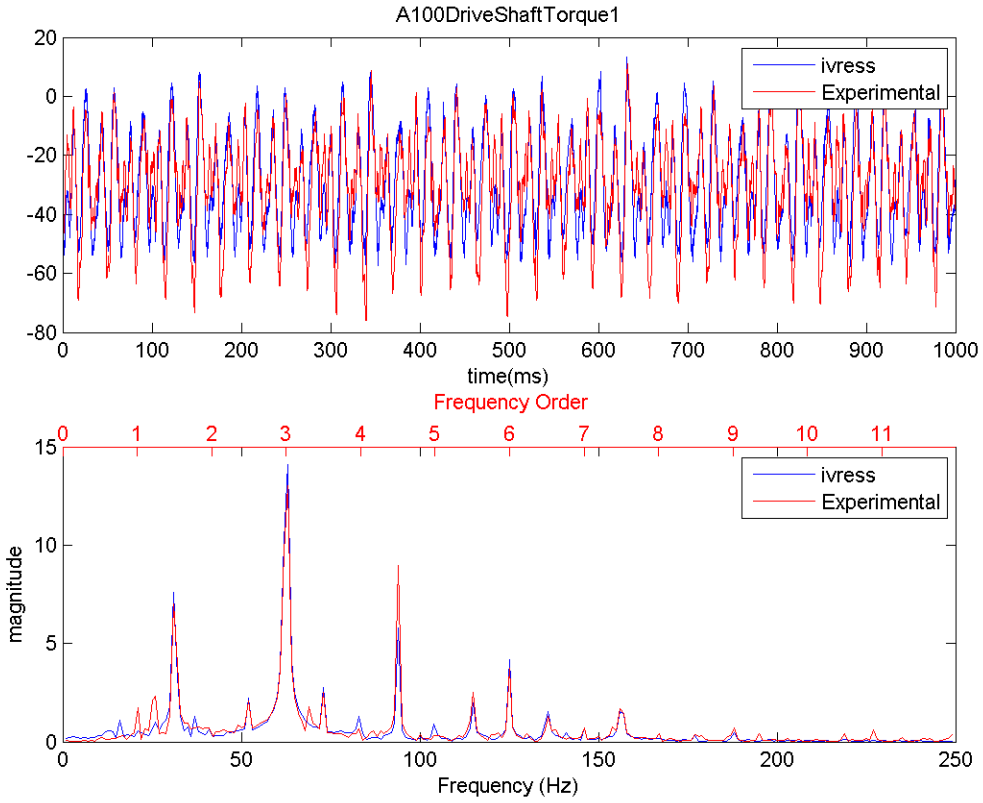

Figure 3.9 Drive shaft torque (N.m) comparison for the A100 operation range

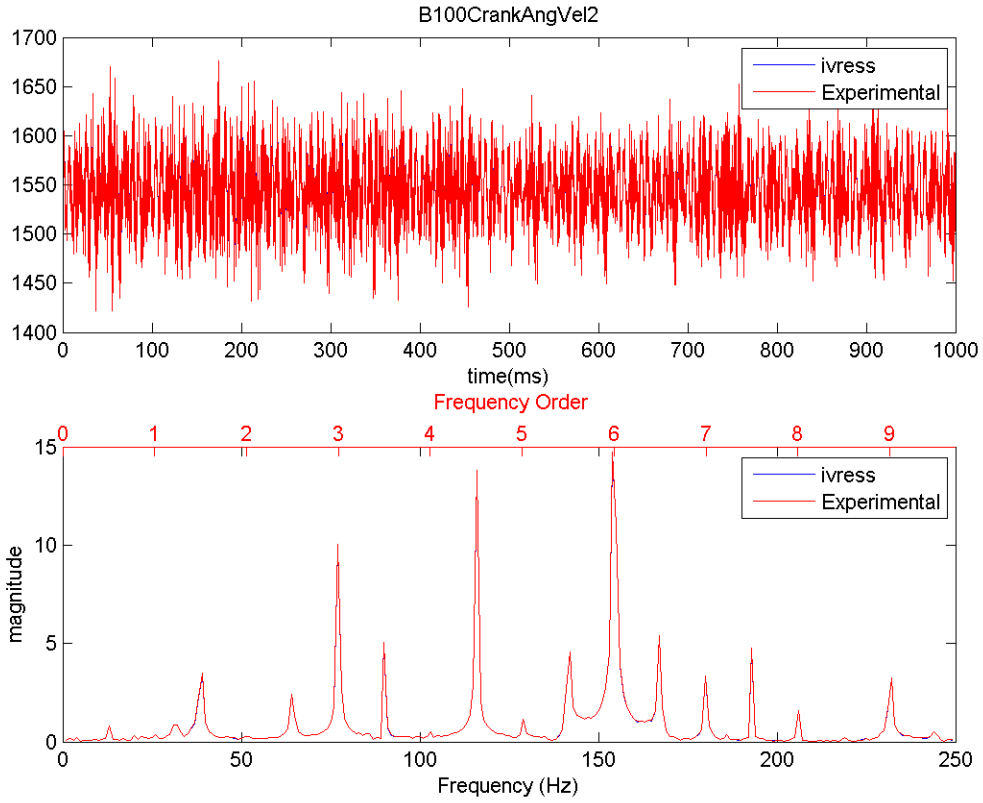

Figure 3.10 Crank angular velocity comparison for the B100 operation range

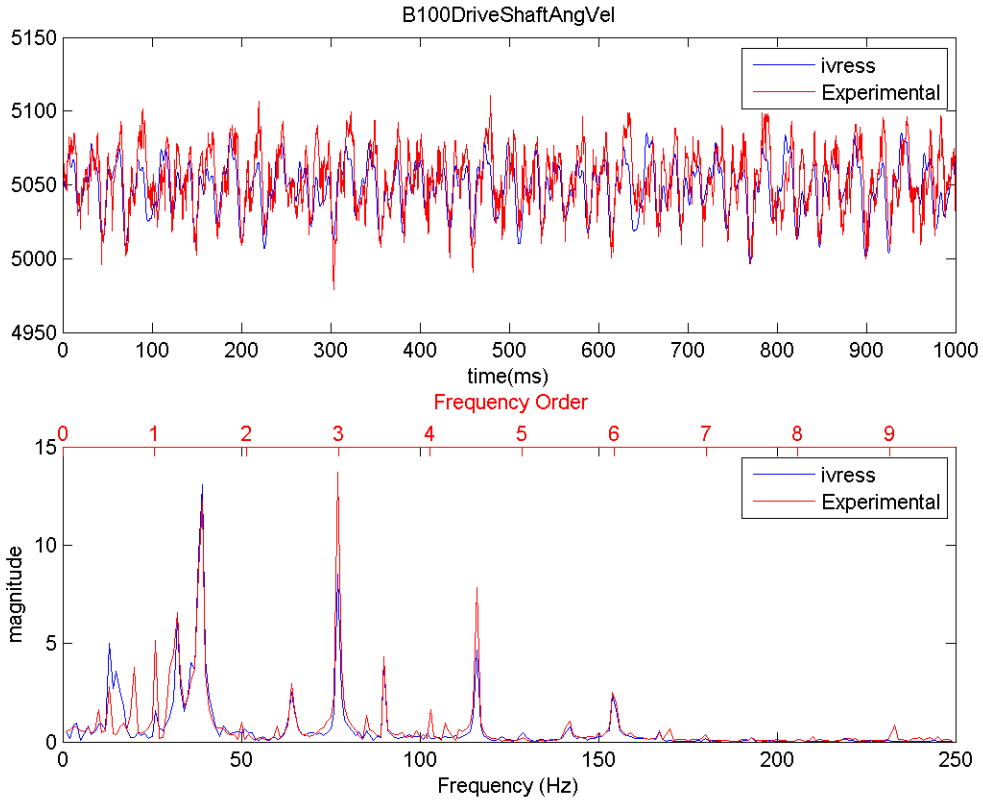

Figure 3.11 Drive shaft angular velocity (RPM) comparison for the B100 operation range

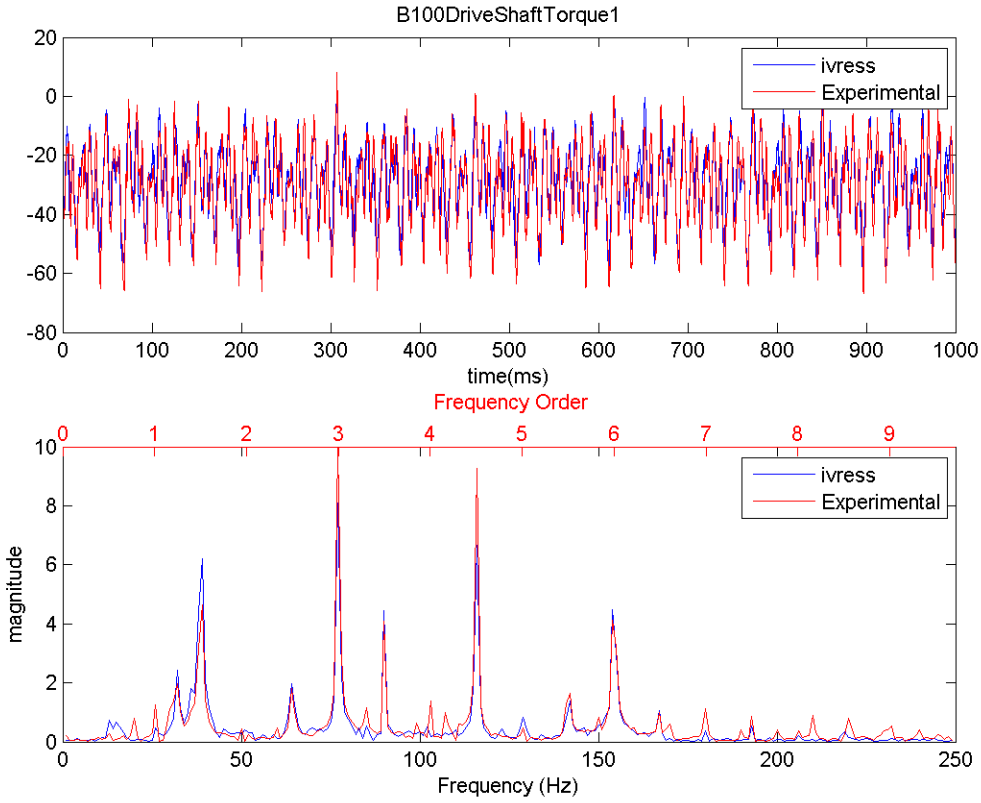

Figure 3.12 Drive shaft torque (N.m) comparison for the B100 operation range

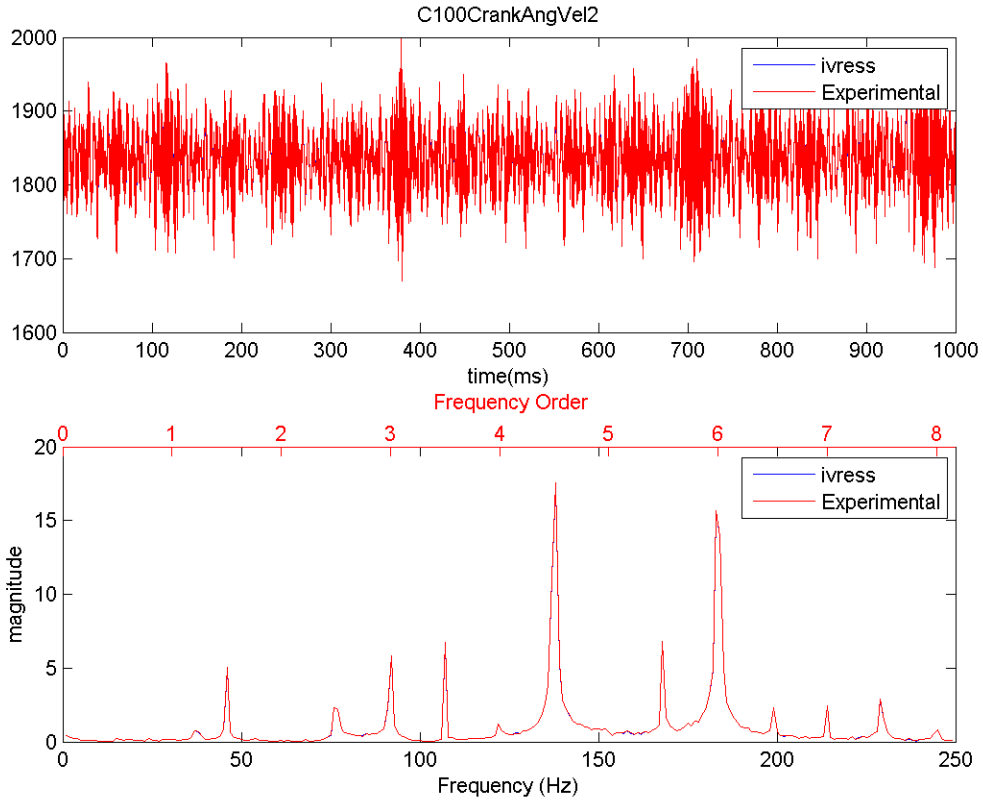

Figure 3.13 Crank angular velocity comparison for the C100 operation range

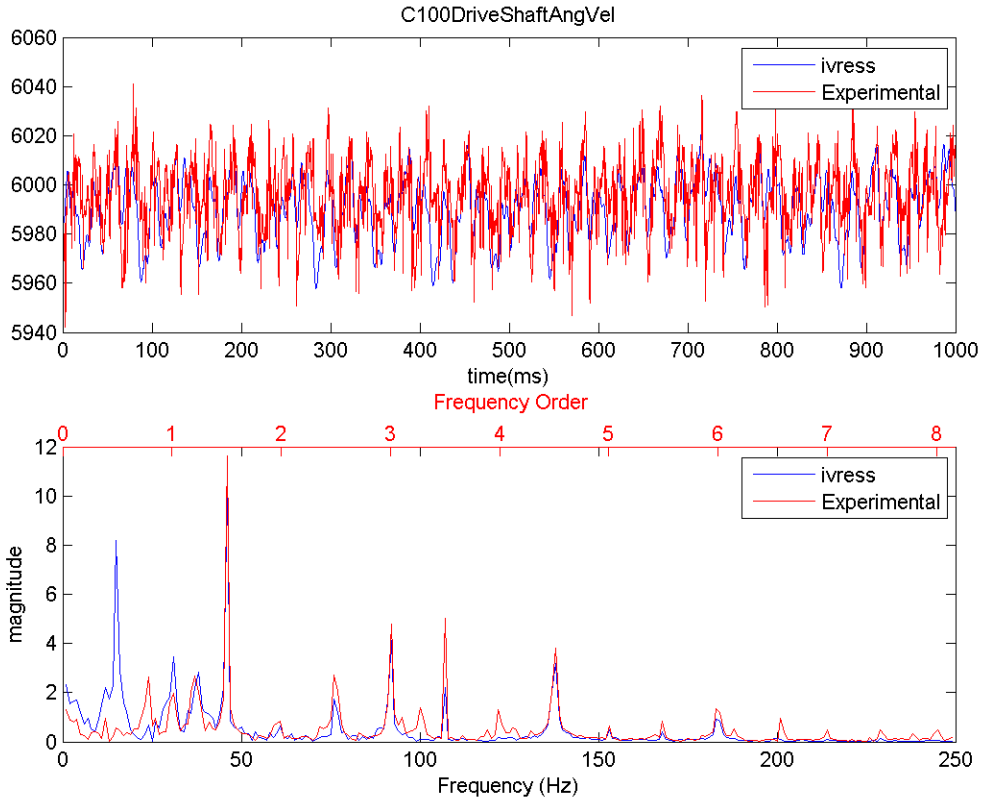

Figure 3.14 Drive shaft angular velocity (RPM) comparison for the C100 operation range

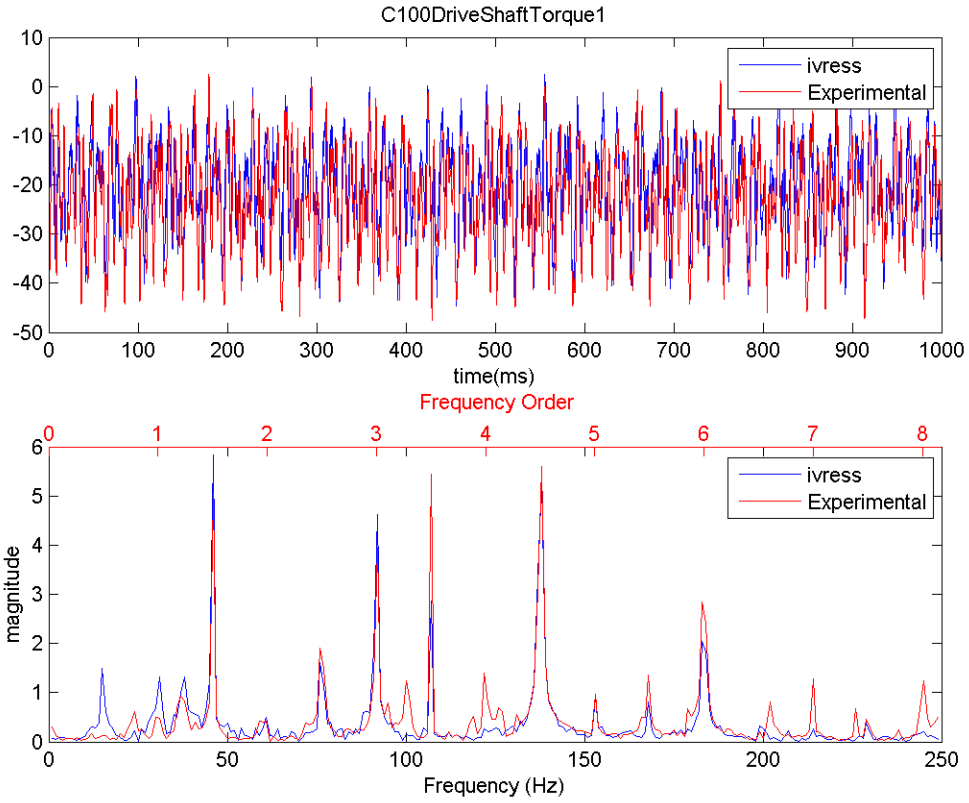

Figure 3.15 Drive shaft torque (N.m) comparison for the C100 operation range

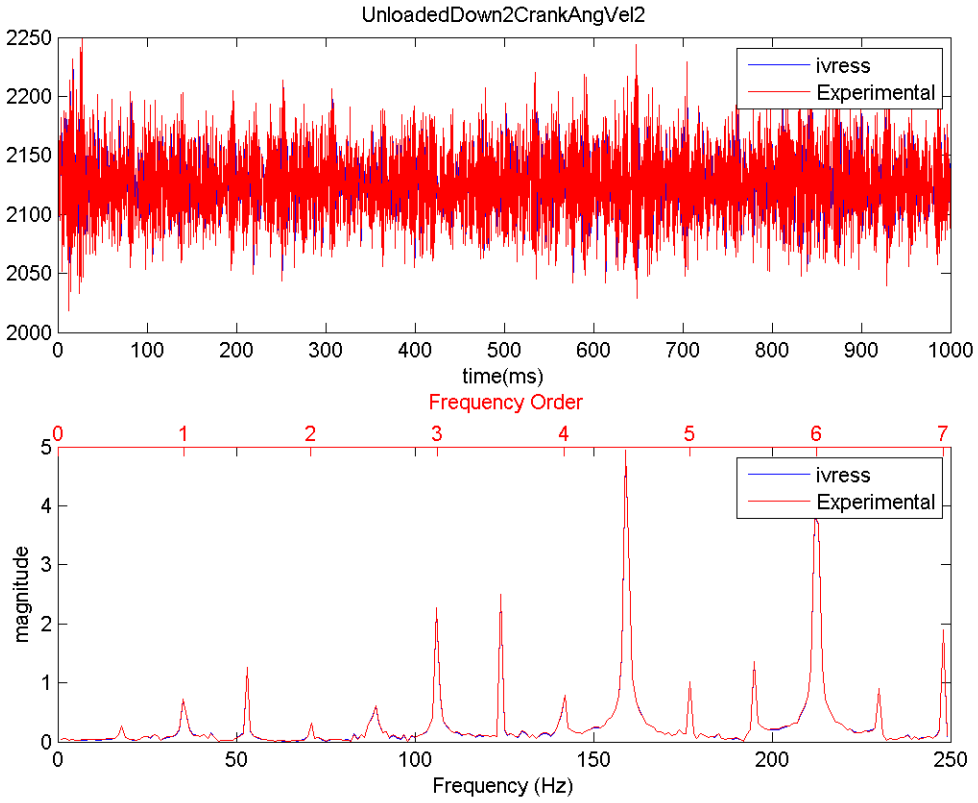

Figure 3.16 Crank angular velocity comparison for the Unloaded Down2 operation range

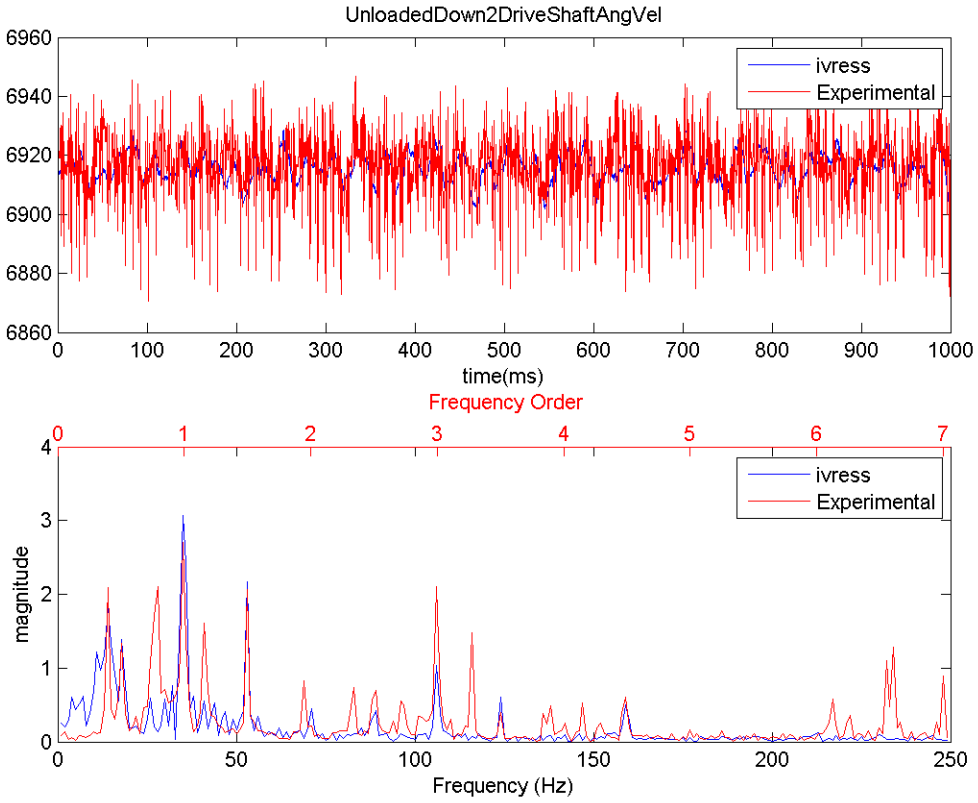

Figure 3.17 Drive shaft angular velocity (RPM) comparison for the Unloaded Down operation range

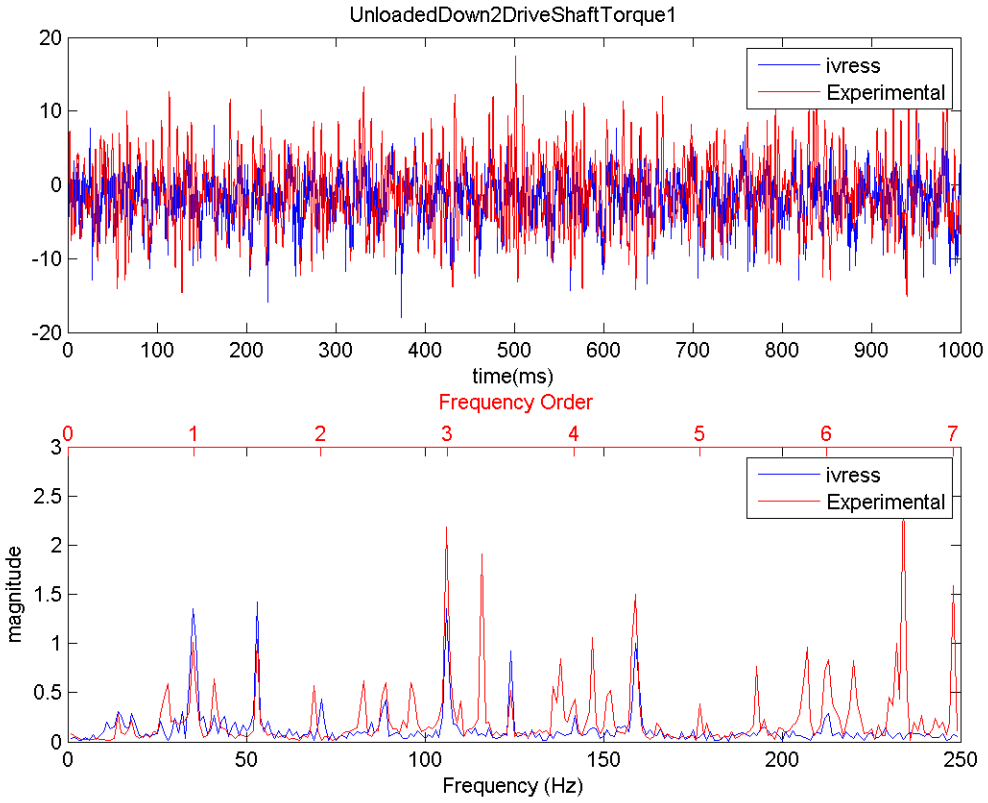

Figure 3.18 Drive shaft torque (N.m) comparison for the Unloaded Down operation range

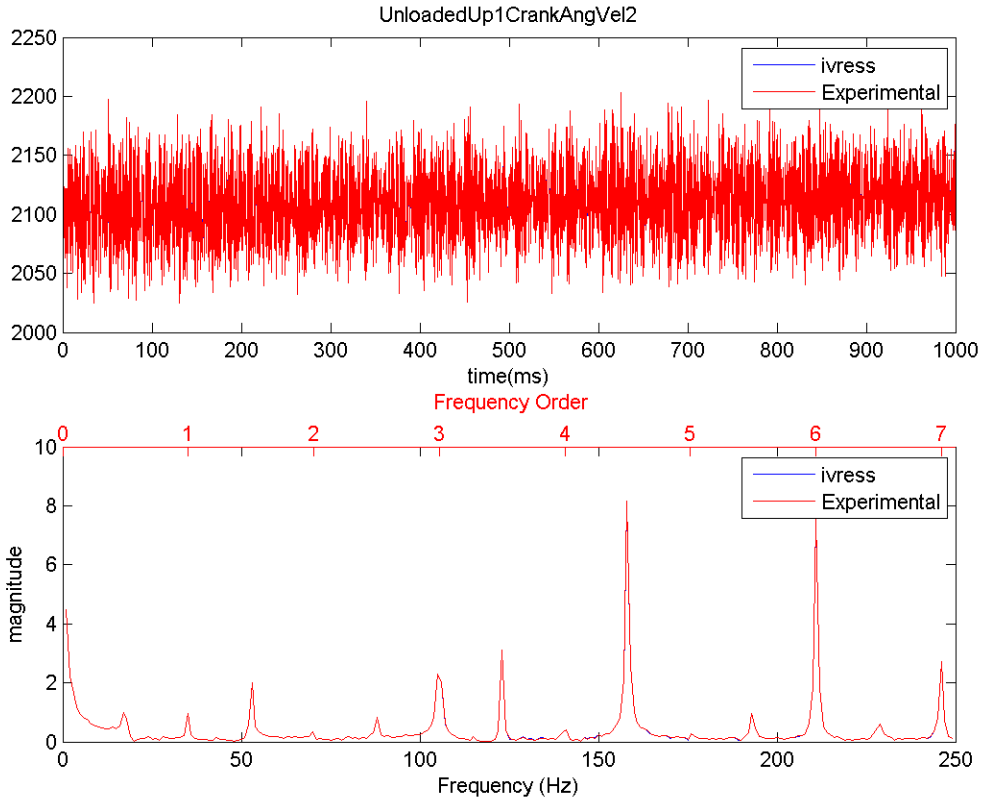

Figure 3.19 Crank angular velocity comparison for the Unloaded Up 1 operation range

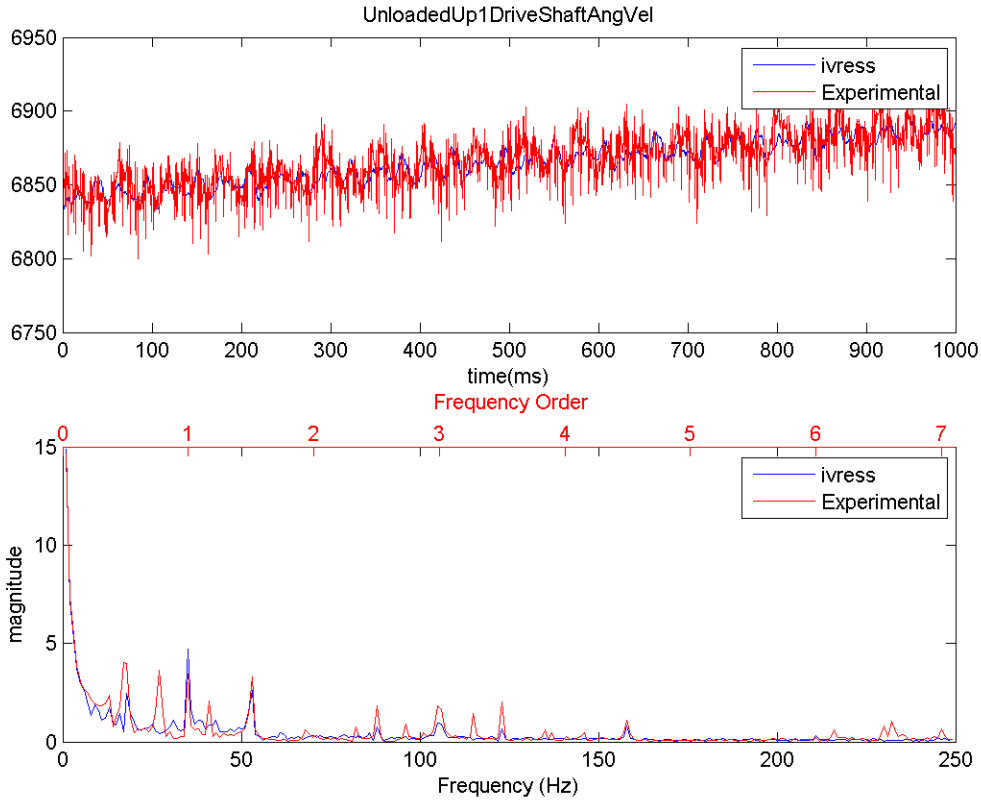

Figure 3.20 Drive shaft angular velocity (RPM) comparison for the Unloaded Up operation range

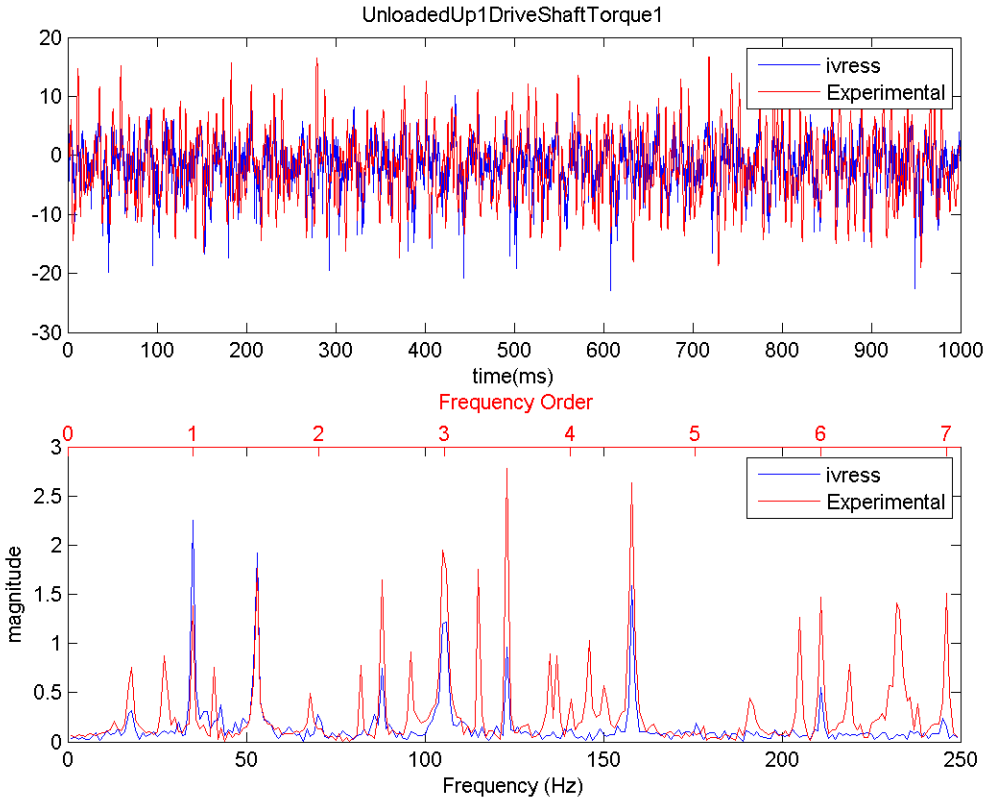

Figure 3.21 Drive shaft torque (N.m) comparison for the Unloaded Up operation range

4. PARAMETER STUDY

Belt properties can change due to change in the physical operating conditions, like operating temperature and humidity or change in belt chemical composition due to oxidation. Moreover, some belt properties are not constant and can be a function of the belt kinematic variables, contact forces or internal belt forces. For example, belt material damping coefficient can be dependent on the strain rate and belt-pulley friction coefficient can be dependent on the normal contact forces. When belt parameters change, the estimation of belt forces and stresses becomes challenging. As a result, it was important to study how the parameters change can affect the dynamic response of the system to assess the accuracy of the model's prediction. In this section, a parameter sensitivity study is conducted to study the effect of the various model parameters on the dynamic response of the belt drive. Then one model parameter is changed and the dynamic response of the new model is generated. In Section 3.5, the dynamic response of the baseline model closely matches the experimental results for the idle, A100, B100 and C100 operation ranges. Therefore, in this section the new models responses are compared to the experimental results in order to assess the sensitivity of a parameter on the dynamic response. The amount of change of a model parameter is selected to be equal to the expected uncertainty or range of change (during the belt operation) of the parameter value in the physical system. Representative plots comparison plots are shown in this section. Appendix I shows the full response comparison plots for all the belt-drive operation ranges.

The model parameters that are changed in the study are:

Tension arm

- Viscous damping.
- Coulomb friction.

Belt

- Axial damping.
- Axial Stiffness
- Bending damping.
- Bending stiffness.
- Coefficient of friction between the front-wrapped pulleys and the belt.

Gears

- Gear backlash.
- Gear tooth stiffness.
- Gear tooth damping.

Drive shaft

- Torsional stiffness.
- Torsional damping.

Turbine shaft

- Torsional stiffness.
- Torsional damping.

4.1 Tensioner Arm

The tensioner arm viscous damping and coulomb friction was found to have a direct and significant effect on the system dynamic response. This is because it affects the response of the tensioner to take over the belt slack.

4.1.1 Viscous Damping

The viscous damping of the tensioner arm, in the baseline numerical model is **0 N.S/m**. On setting the tensioner arm damping to **5 N.S/m** instead of **0 N.S/m**, the amplitude of the drive shaft torque decreased significantly. This is due to the dissipation of some energy of the system to compensate the extra tensioner damping. The comparison is shown in Figure 4.1.

4.1.2 Coulomb Friction

Coulomb friction torque (due to friction at the tensioner pivot point) in the tensioner has a similar effect to damping. On increasing the friction torque from 3.14 N.m to 8 N.m the response becomes more damped and the vibration amplitude of the drive shaft angular velocity is about half that of the experimental results (Figure 4.2).

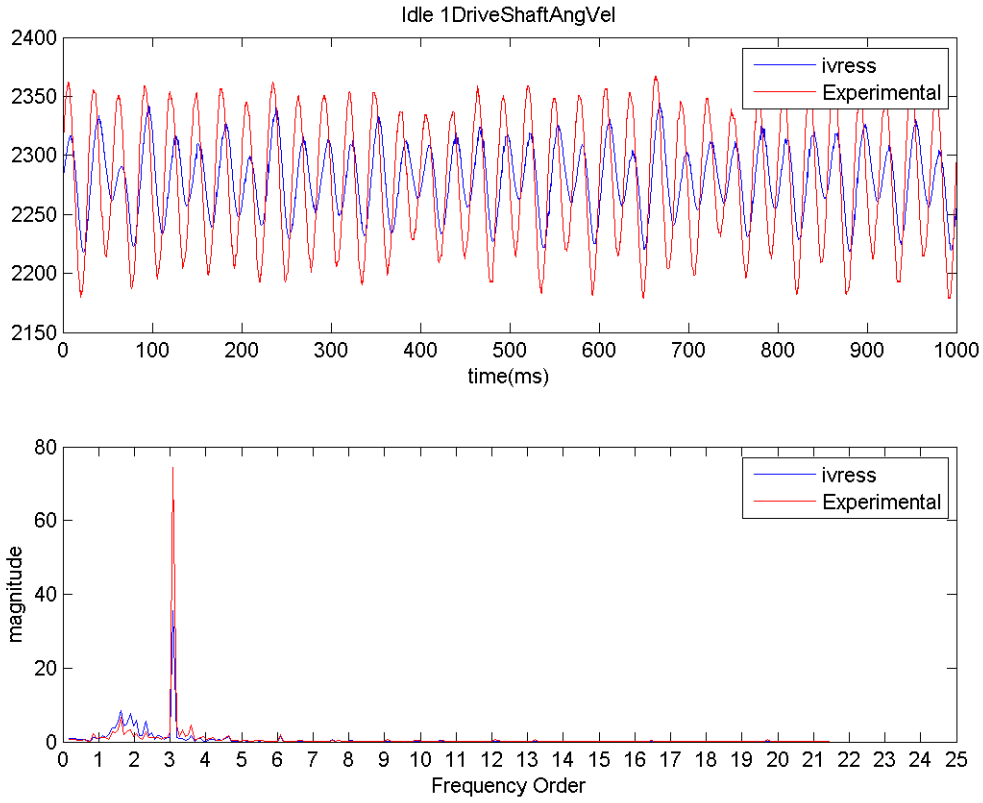

Figure 4.1 Drive shaft angular velocity in the idle operation range with tensioner arm viscous damping = 5 N.S/m

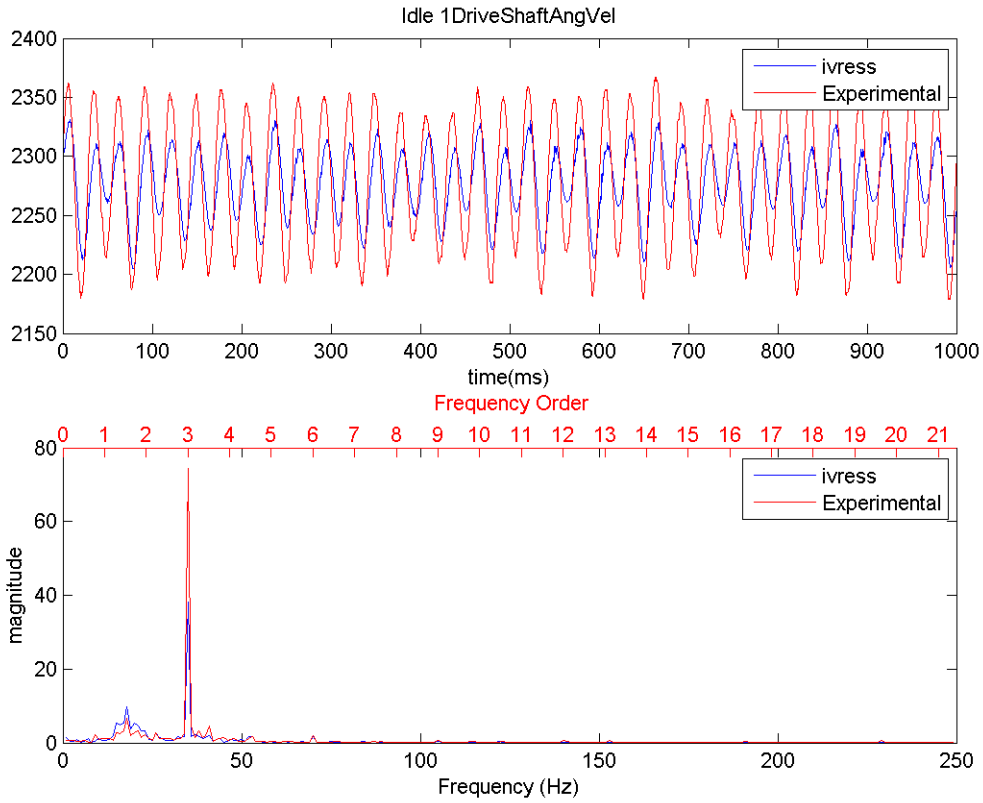

Figure 4.2 Drive shaft angular velocity in the idle operation range with tensioner arm coulomb friction = 8 instead of 3.14 in the base line

4.2 Belt

Belt axial stiffness and damping may change with the belt age due to heat, chemical effects and belt fatigue loading.

4.2.1 Belt Axial Damping

In this study, the belt axial damping was chosen to be constant, but a simulation was run to determine the sensitivity of the system to change in belt axial damping. In this simulation, the belt damping was increased by 50% from 10 N.s/m to 15 N.s/m. the

response, in terms of drive shaft angular velocity and drive shaft torque didn't show any significant change from the base line run. Figure 4.3 and Figure 4.4 show the result plots from the sensitivity study.

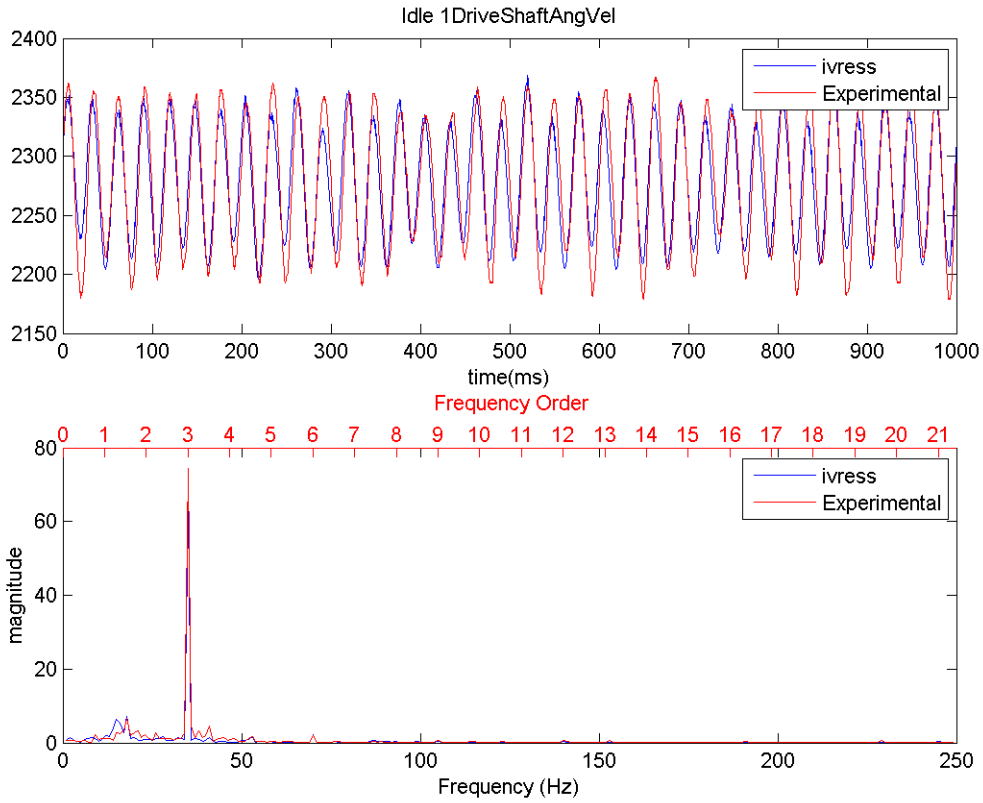

Figure 4.3 Drive shaft angular velocity in the idle operation range with belt axial damping = 15 N.s/m instead of 10 N.s/m in the base line

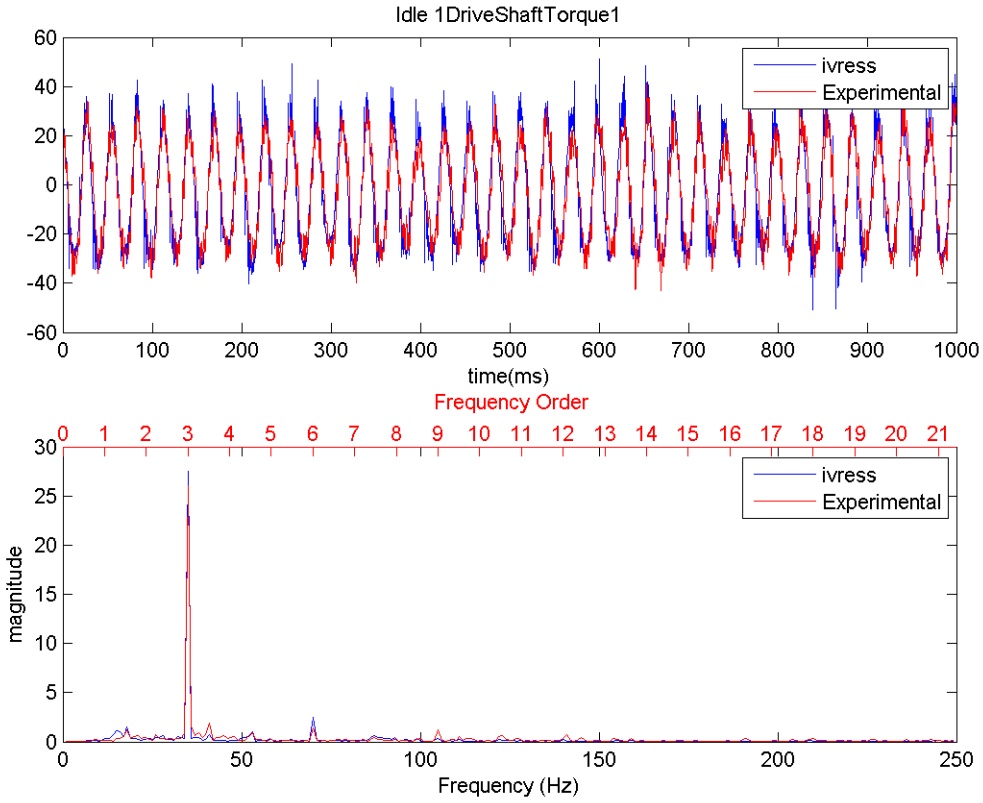

Figure 4.4 Drive shaft torque in the idle operation range with belt axial damping = 15 $N.s/m$ instead of 10 $N.s/m$ in the base line

4.2.2 Belt Axial Stiffness

Decreasing the belt axial stiffness (EA) from 140,563 N to 110,000 N makes the belt more flexible thus causing it to exhibit more axial strain. This behavior dissipates more energy due to belt axial damping. This can be observed as more damped response compared to the baseline and experimental results as shown Figure 4.5 and Figure 4.6.

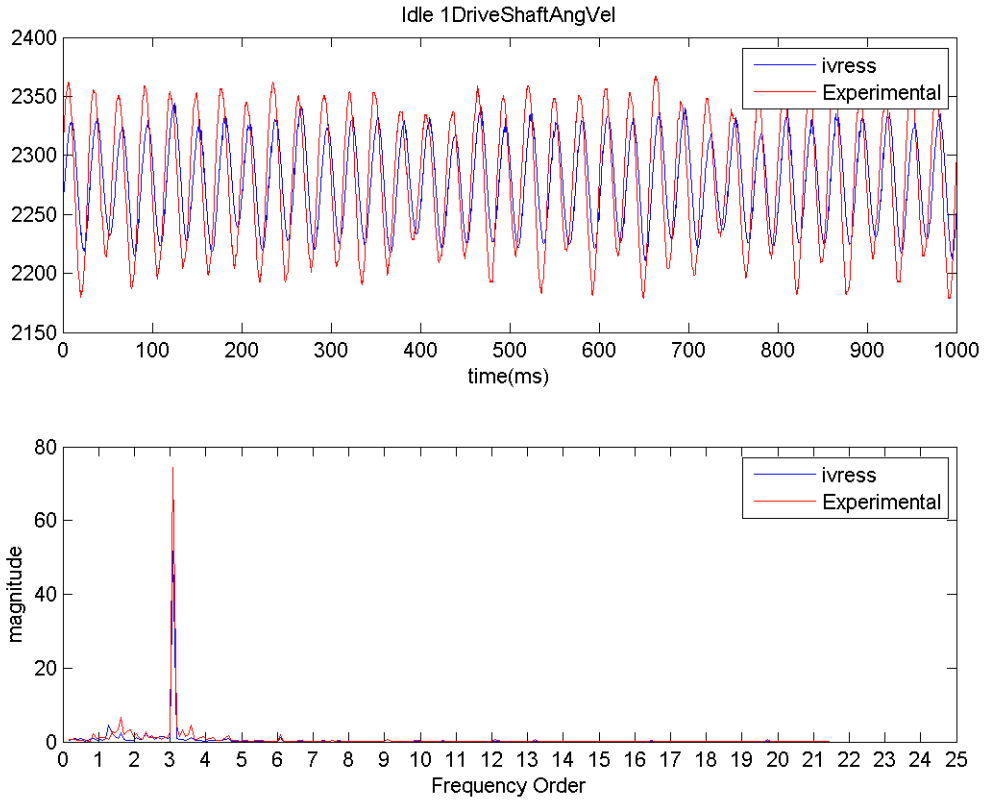

Figure 4.5 Drive shaft angular velocity in the idle operation range with belt axial stiffness (EA) = 110,000 N instead of 140,563N in the base line

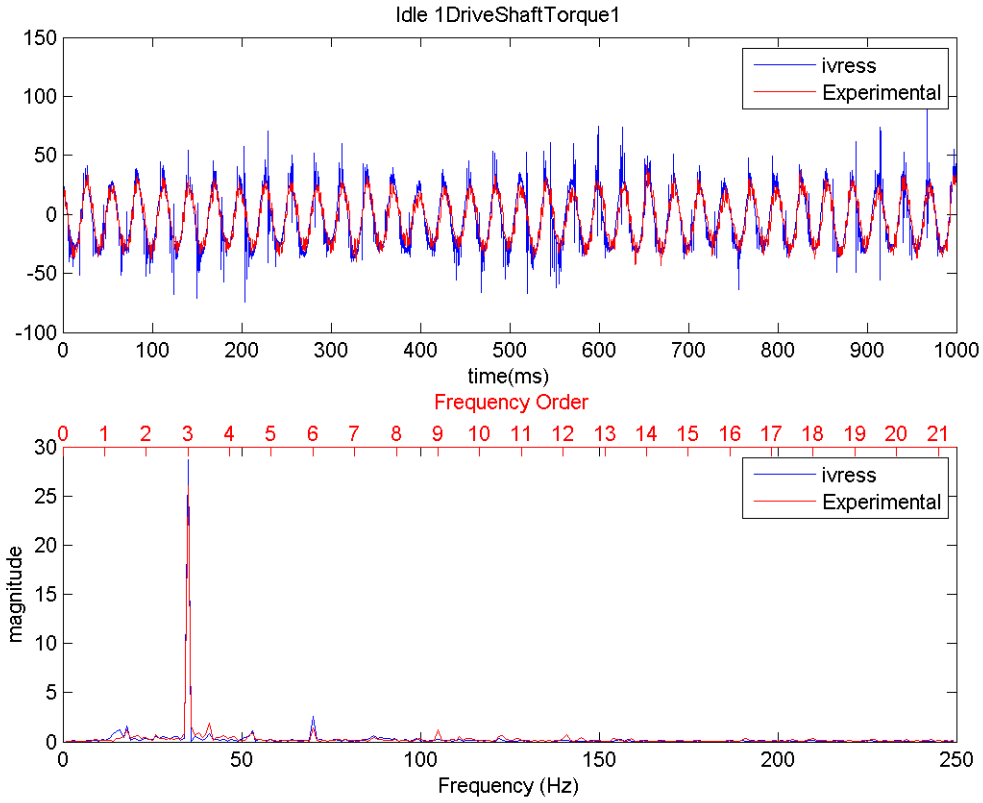

Figure 4.6 Drive shaft torque in the idle operation range with belt axial stiffness (EA) = 110,000 N instead of 140,563 N in the base line

4.2.3 Belt Bending Damping

The belt bending damping is increased from 5×10^{-5} N.m^2.s to 10×10^{-5} N.m^2.s. The response did not show any significant difference between this simulation and the base line in both drive shaft angular velocity and torque (See Figure 4.7 and Figure 4.8).

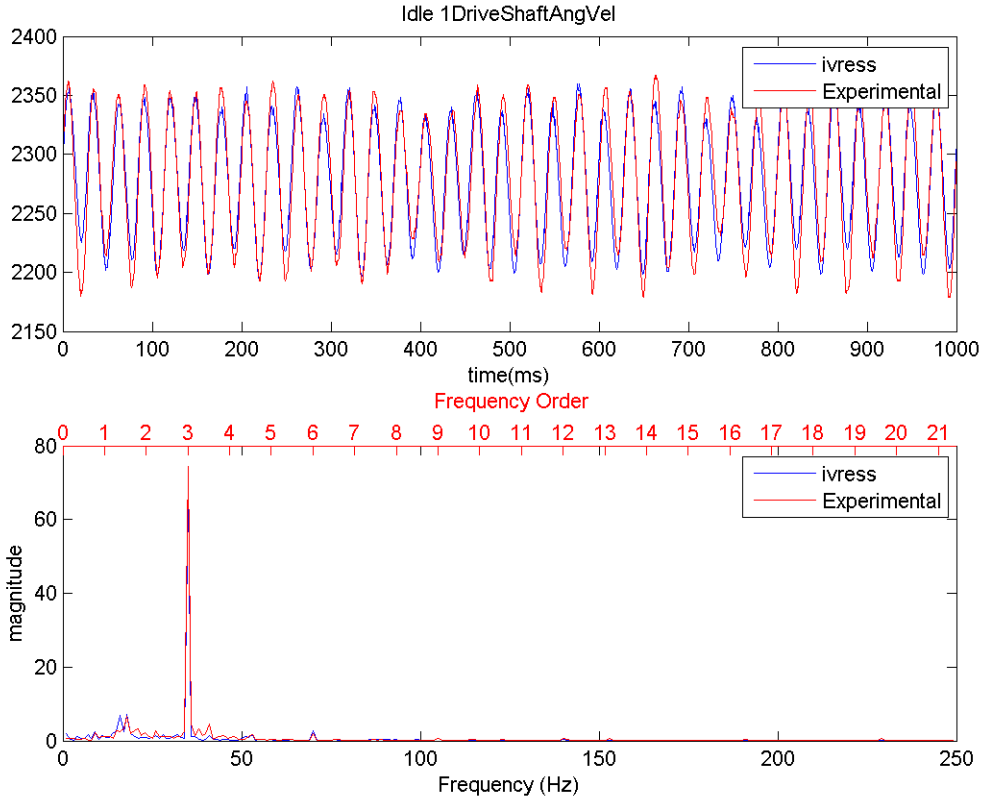

Figure 4.7 Drive shaft angular velocity in the idle operation range with belt bending damping = 10×10^{-5} N.s/rad instead of 5×10^{-5} N.s/rad in the base line

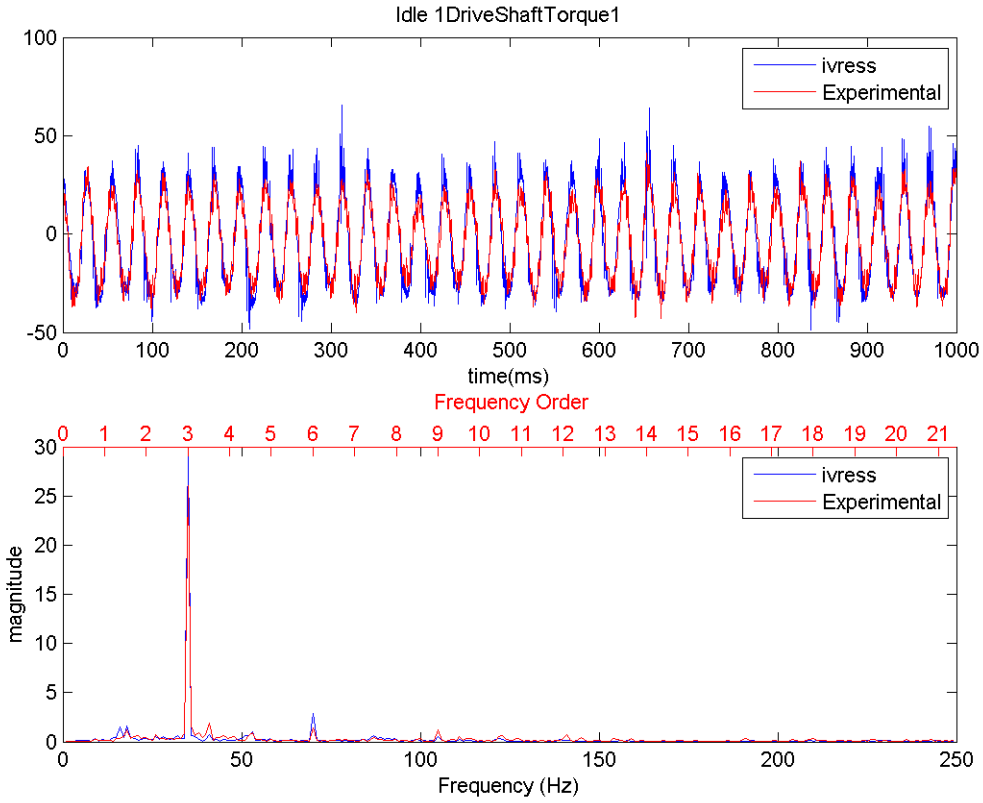

Figure 4.8 Drive shaft torque in the idle operation range with belt bending damping $= 10 \times 10^{-5}$ N.s/rad instead of 5×10^{-5} N.s/rad in the base line

4.2.4 Belt Bending Stiffness

In the baseline model, the belt bending stiffness was set to zero. On increasing the belt bending stiffness the belt will tend to lose the ability to fully bend around the pulleys. Figure 4.9 and Figure 4.10 show the result plots for drive shaft angular velocity and torque when belt bending stiffness has increased from 0 N/rad to 2 N/rad in both time and frequency domain. When the belt bending stiffness was increased to 2 $N.m^2$, the belt exhibited less wrapping around the pulleys causing poor traction force on the pulleys. In the frequency domain, the main frequency is shifted to a lower value. Note that this response is not expected in the physical model, but it is expected that the belt will crack in order to follow the pulley geometry instead of resisting bending.

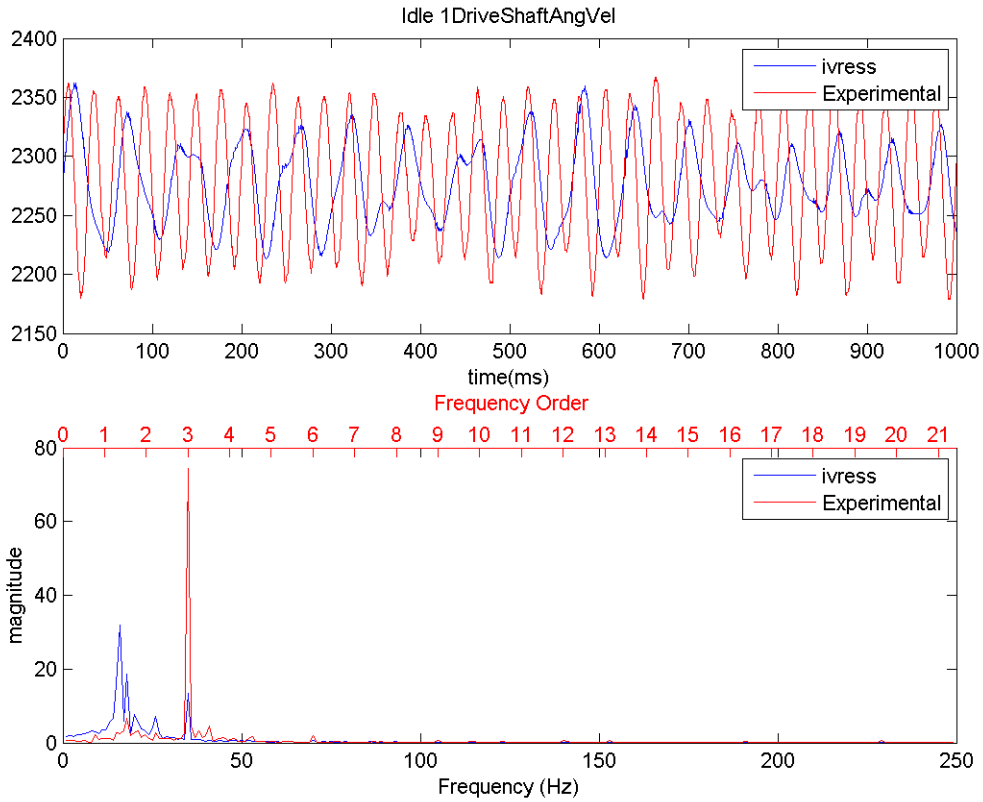

Figure 4.9 Drive shaft angular velocity in the idle operation range with belt bending stiffness = 2 N/rad instead of 0 N/rad in the base line

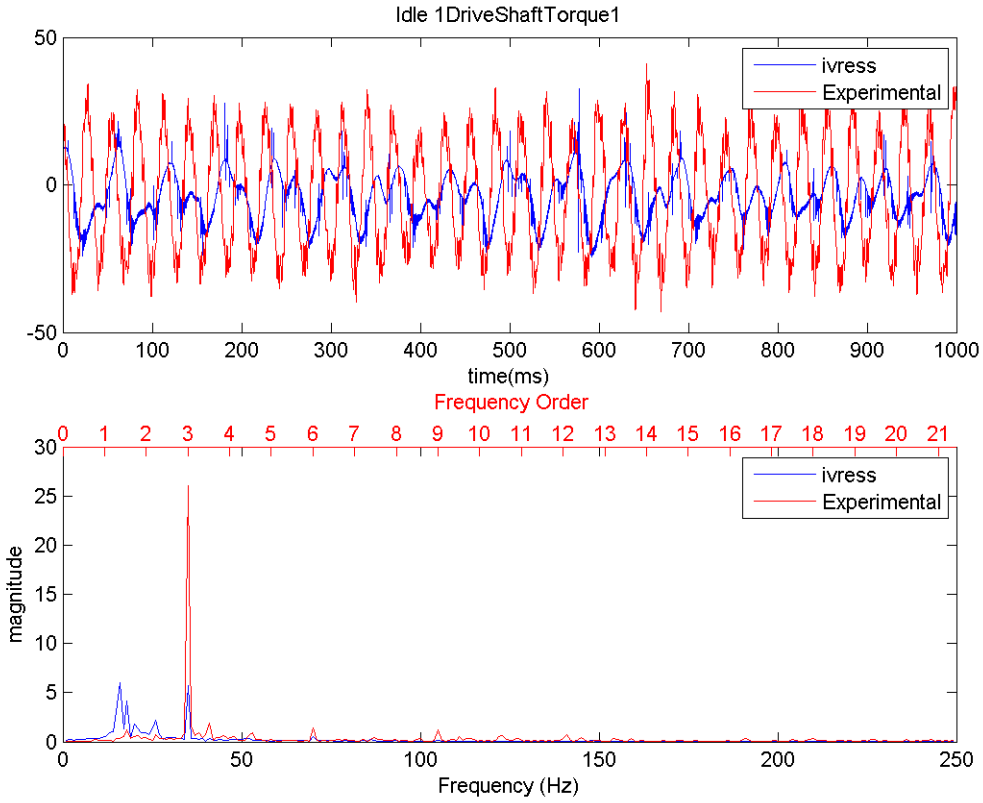

Figure 4.10 Drive shaft torque in the idle operation range with belt bending stiffness = 2 N/rad instead of 0 N/rad in the base line

4.2.5 Coefficient of Friction (Static-Kinetic Friction Curve)

In this section, two simulations were run. In the first one, the belt coefficient of friction was increased to 1 instead of 0.6 in the baseline model (Figure 4.13 and Figure 4.14). While in the second simulation, the belt coefficient of friction was reduced to 0.4 instead of 0.6 in the base line (Figure 4.15 and Figure 4.16). The simulations showed that on changing the coefficient of friction, the amplitude of the drive shaft angular velocity as well as the drive shaft torque doesn't have a significant change till it drops below some threshold where the belt starts to loose traction with the pulleys and slip. In this model, the coefficient of friction threshold appears to be around 0.45 for the B100 operation range which has the highest transmitted torque. Thus, the B100 operation range results were selected as representative results in this section figures. When the belt coefficient of friction was decreased to 0.4, the result showed a significant decrease in the amplitude for both drive shaft angular velocity, as well as drive shaft torque (Figure 4.15 and Figure 4.16).

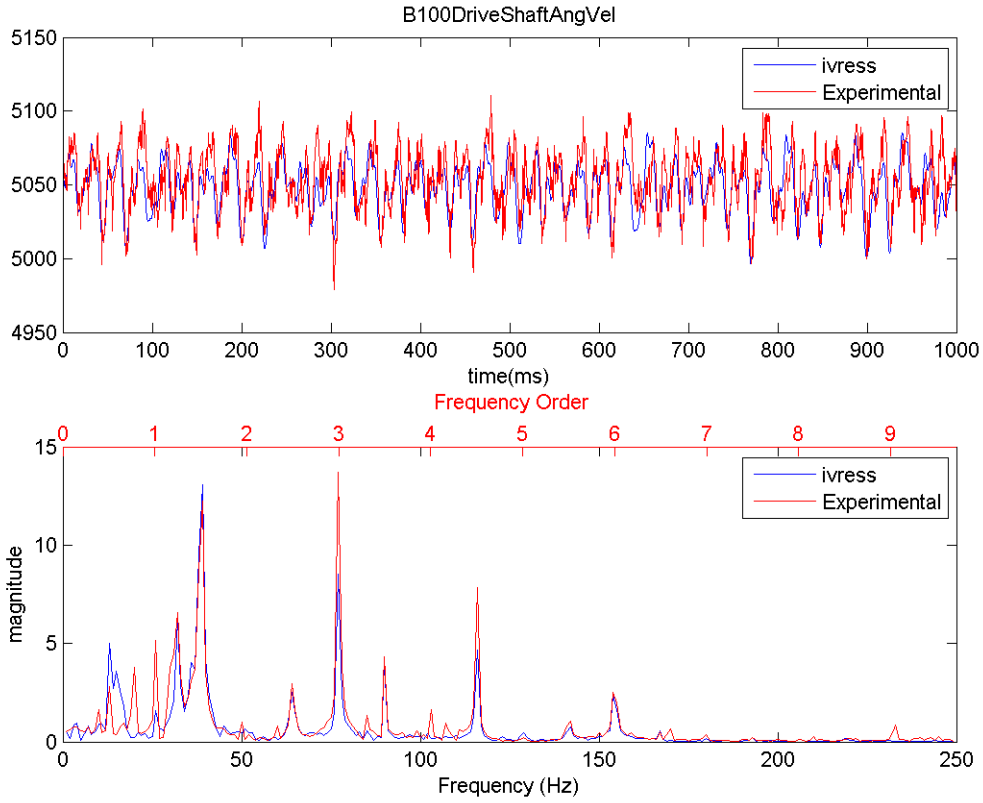

Figure 4.11 Drive shaft angular velocity in the B100 operation range with belt coefficient of friction 0.6

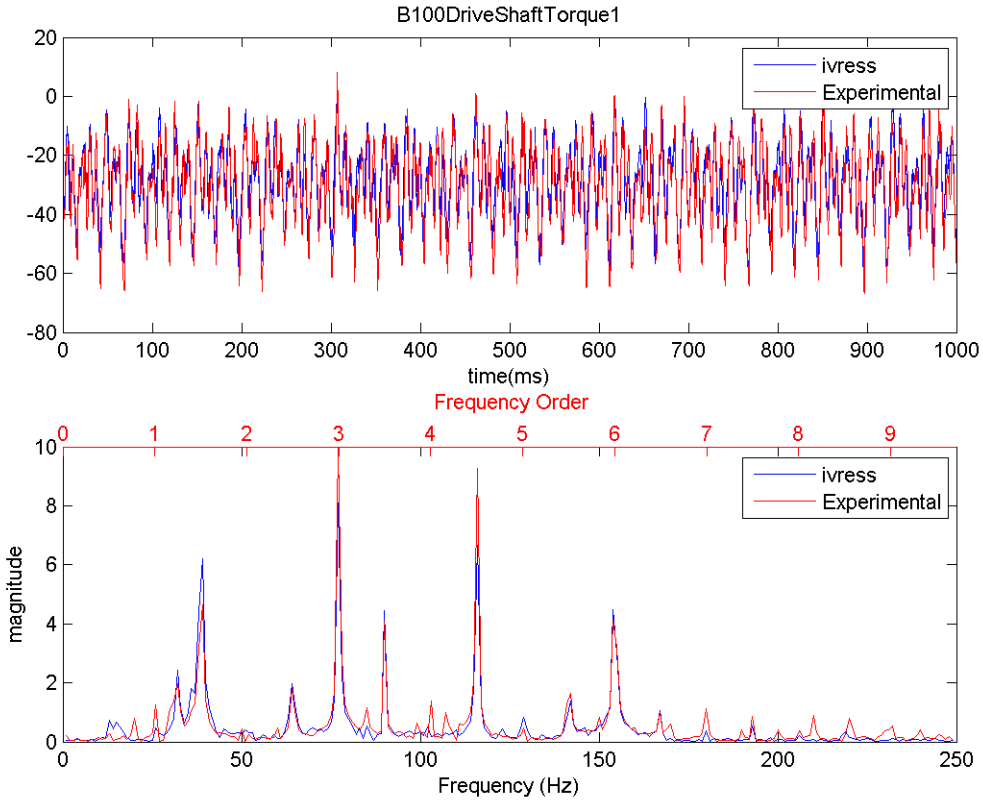

Figure 4.12 Drive shaft torque in the B100 operation range with belt coefficient of friction 0.6

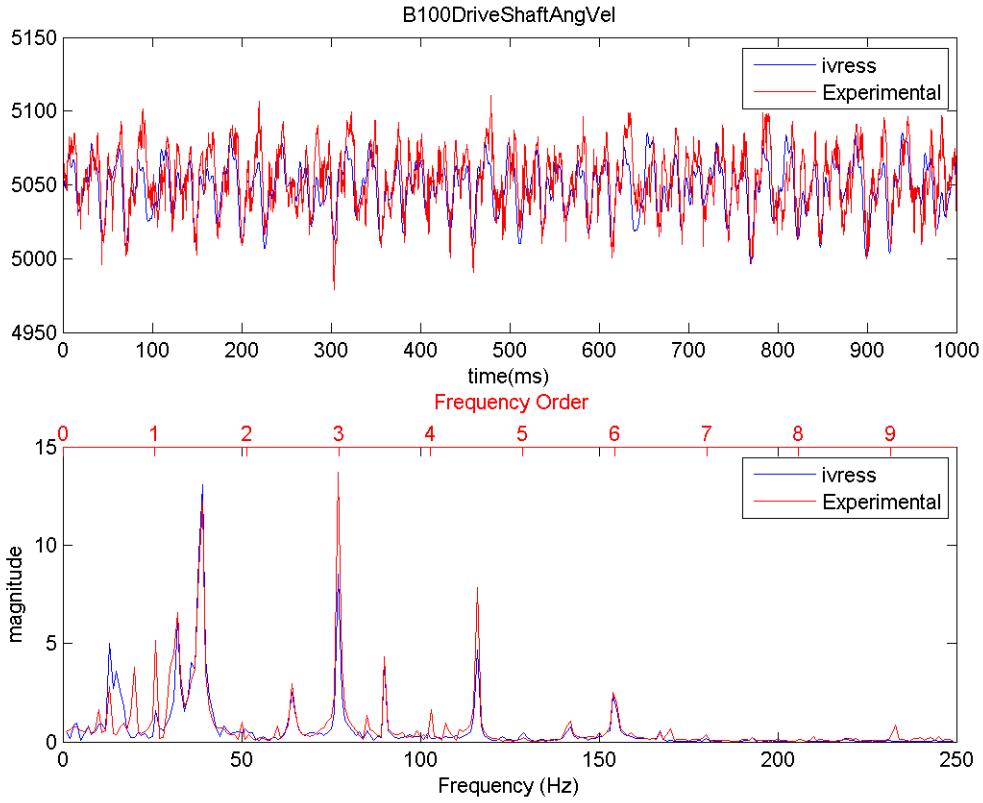

Figure 4.13 Drive shaft angular velocity in the idle operation range with belt coefficient of friction increased to 1 instead of 0.6 in the baseline

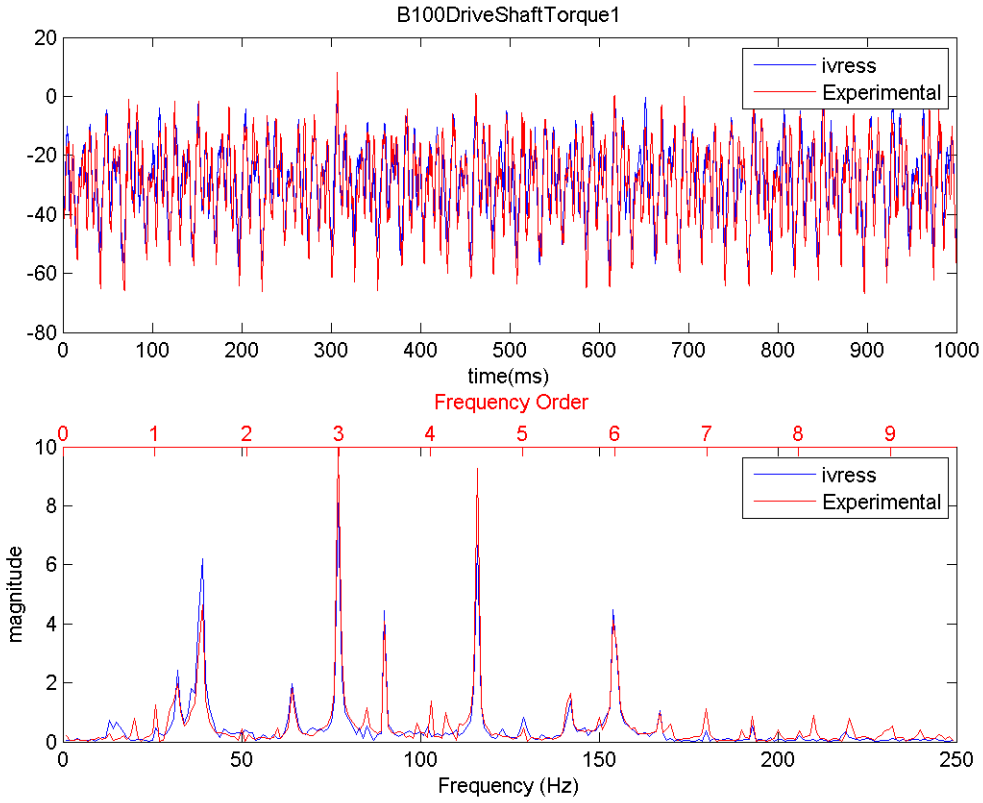

Figure 4.14 Drive shaft torque in the idle operation range with belt coefficient of friction increased to 1 instead of 0.6 in the baseline

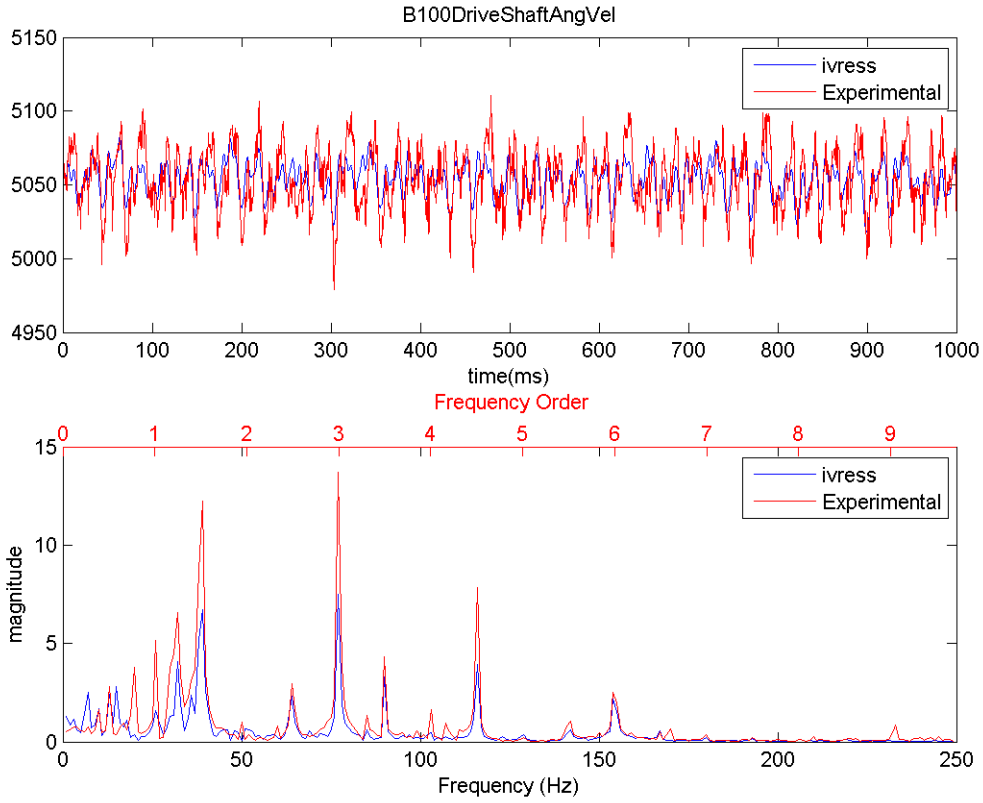

Figure 4.15 Drive shaft angular velocity in the B100 operation range with belt coefficient of friction decreased to 0.4 instead of 0.6 in the baseline

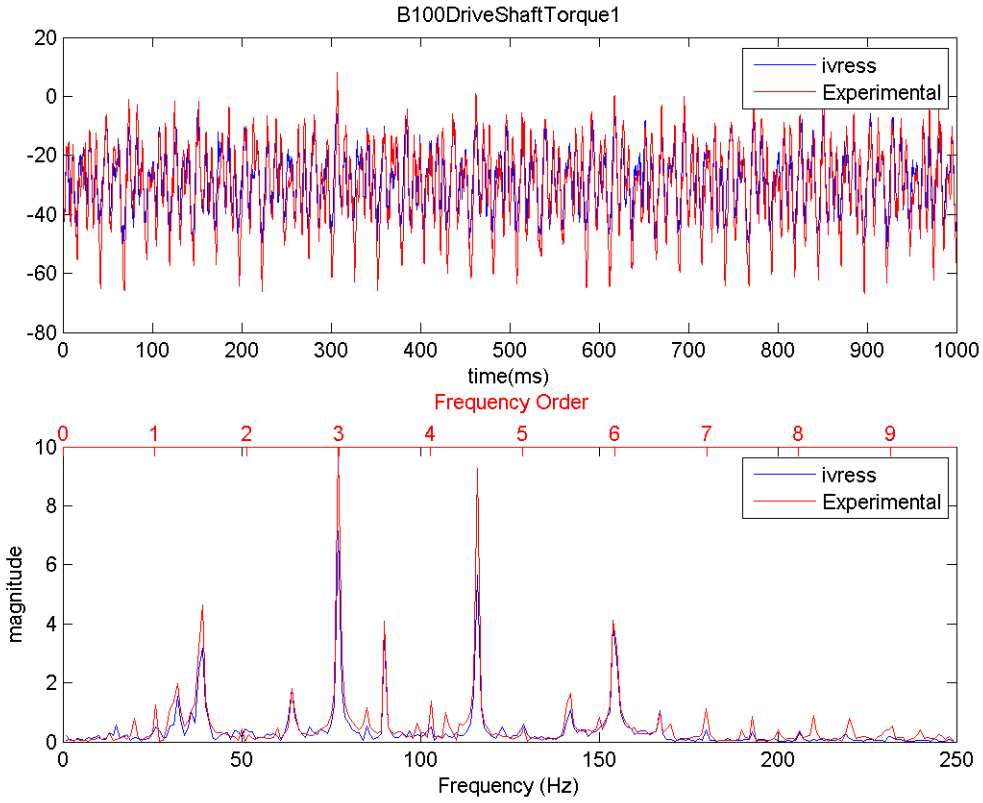

Figure 4.16 Drive shaft torque in the B100 operation range with belt coefficient of friction decreased to 0.4 instead of 0.6 in the baseline

4.3 Gears

4.3.1 Gear Backlash

Increasing the gear backlash did not have any significant effect on the response till some limit when the gears start to bounce. When the gears start bouncing, the angular velocity response at the drive shaft does not have significant change, however; the torque response will start to show spikes, see Figure 4.17, due to bouncing and tooth impact.

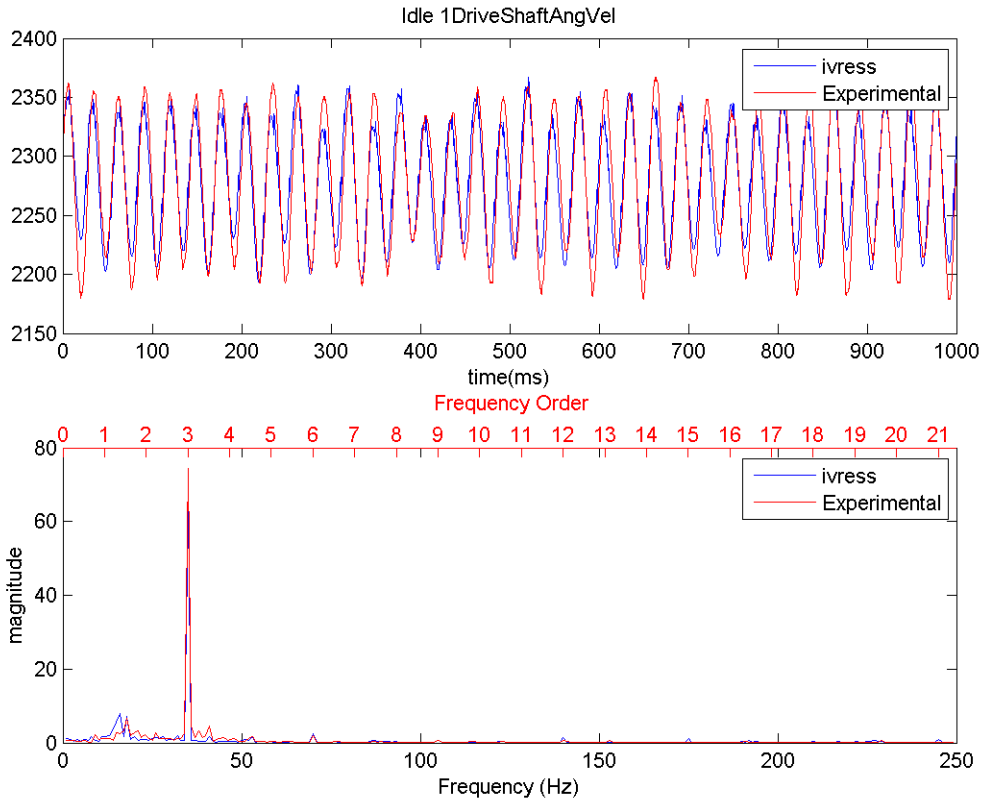

Figure 4.17 Drive shaft angular velocity in the idle operation range with pinion tooth backlash increased to $25 \times 10^{-5}m$ instead of $5 \times 10^{-5}m$ in the baseline

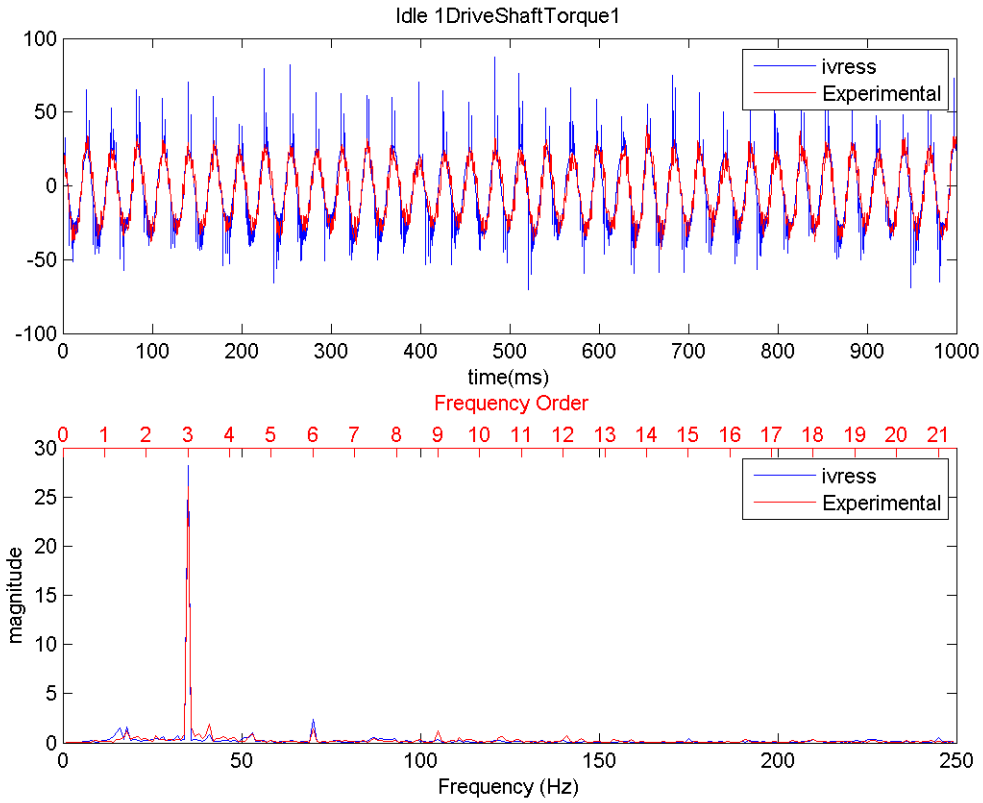

Figure 4.18 Drive shaft torque in the idle operation range with pinion tooth backlash increased to $25 \times 10^{-5}\ m$ instead of $5 \times 10^{-5}\ m$ in the baseline

4.3.2 Gear Tooth Stiffness

Increasing the pinion gear tooth stiffness from $4 \times 10^{13} N/m$ instead of $2 \times 10^{13} N/m$ in the base line, didn't have significant impact on the response of the driveshaft angular velocity, however, the torque response shows some spikes in the time domain due to the increase of the impact magnitude, due to the increase in stiffness.

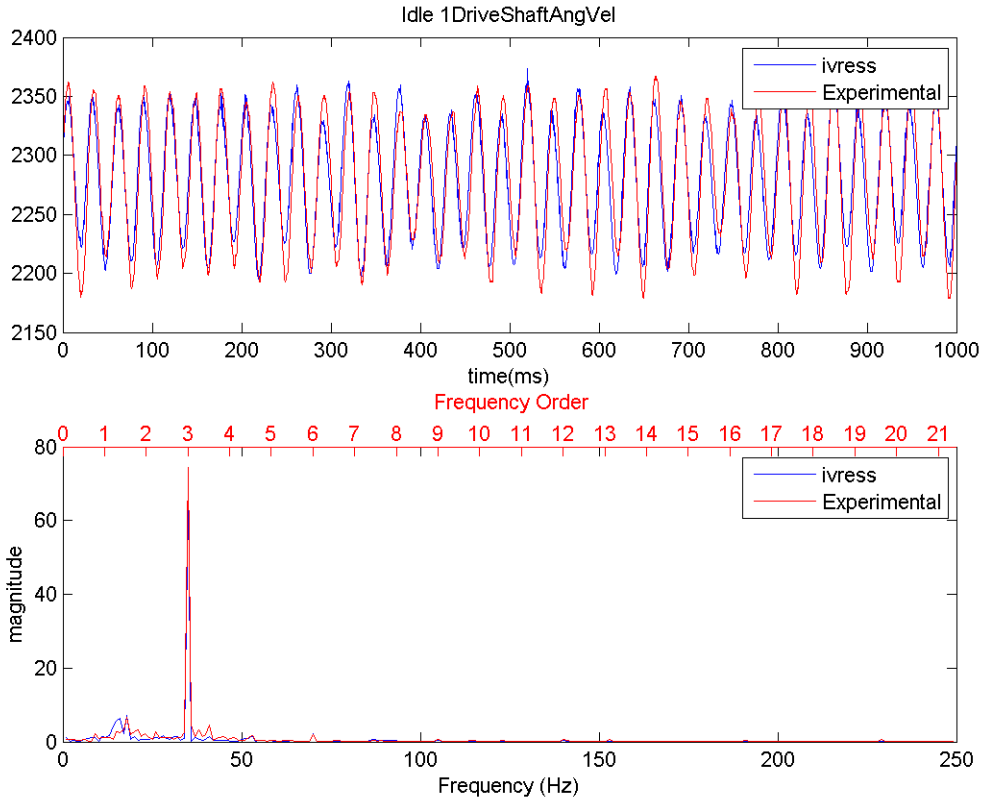

Figure 4.19 Drive shaft angular velocity in the idle operation range with pinion tooth stiffness increased to $4 \times 10^{13} N/m$ instead of $2 \times 10^{13} N/m$ in the baseline

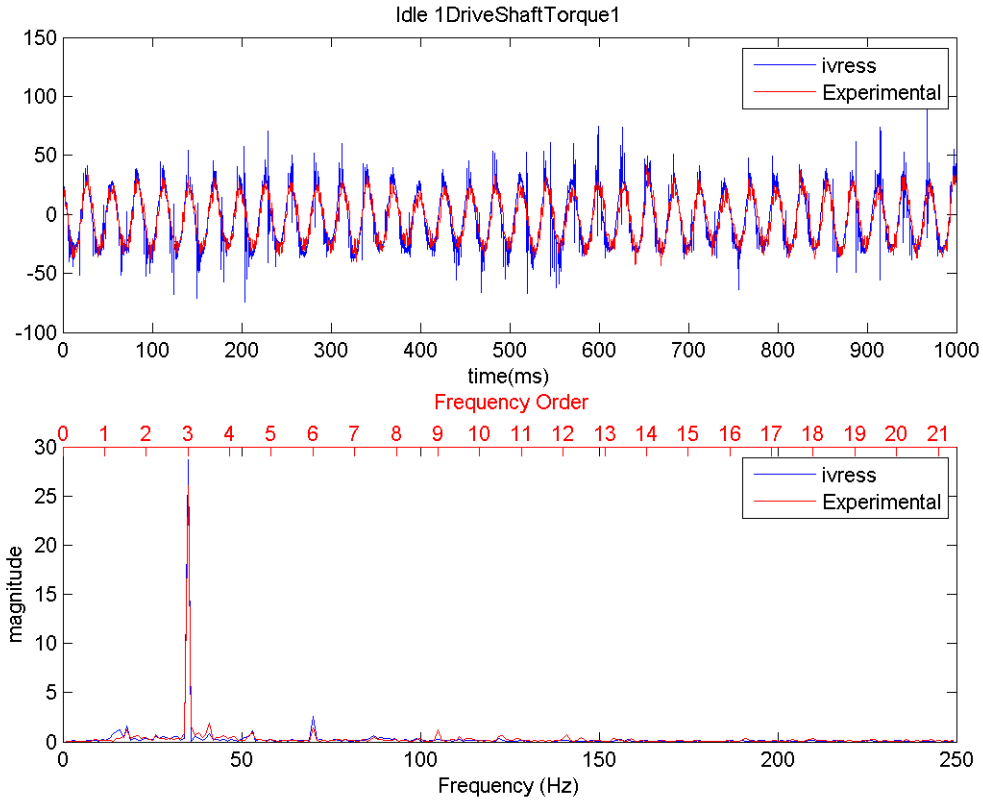

Figure 4.20 Drive shaft torque in the idle operation range with pinion tooth stiffness increased to 4×10^{13} N/m instead of 2×10^{13} N/m in the baseline

4.3.3 Gear Tooth Damping

In this simulation, the pinion gear tooth damping has been decreased $2 \times 10^6\ N.s/m$ instead of $4 \times 10^6\ N.s/m$ in the baseline. Decreasing the tooth stiffness did not have a significant effect on the response of any of drive shaft angular velocity or the torque. The responses are shown in Figure 4.21 and Figure 4.22

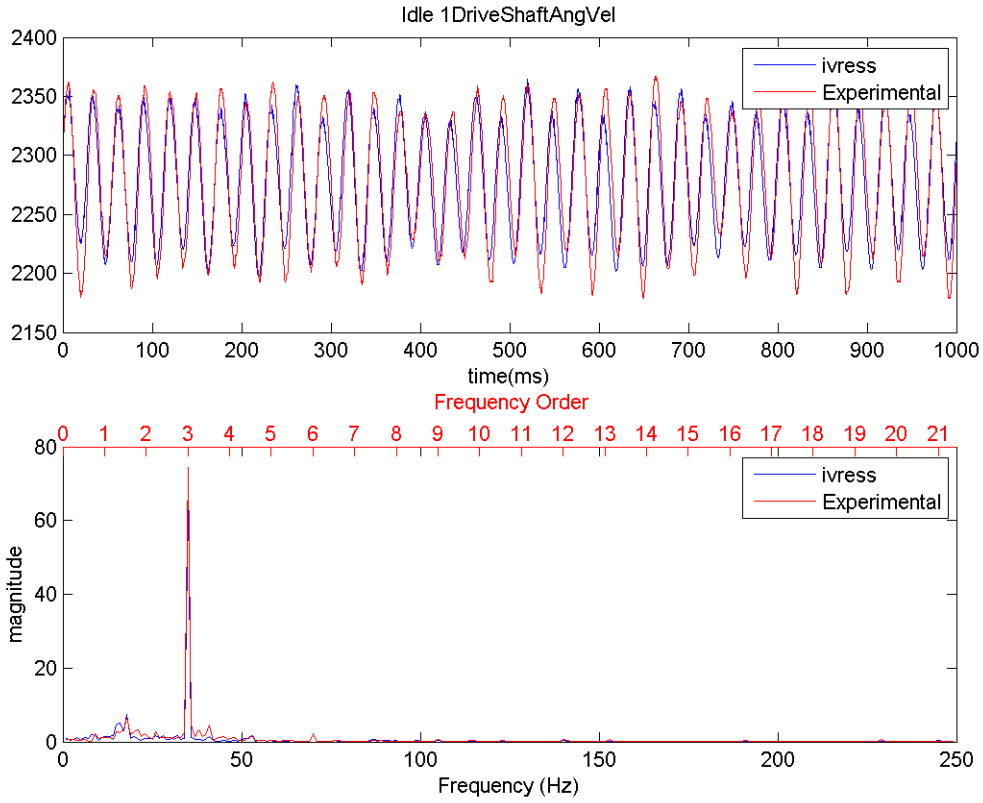

Figure 4.21 Drive shaft angular velocity in the idle operation range with pinion tooth damping decreased to $2 \times 10^6 N.s/m$ instead of $4 \times 10^6 N.s/m$ in the baseline

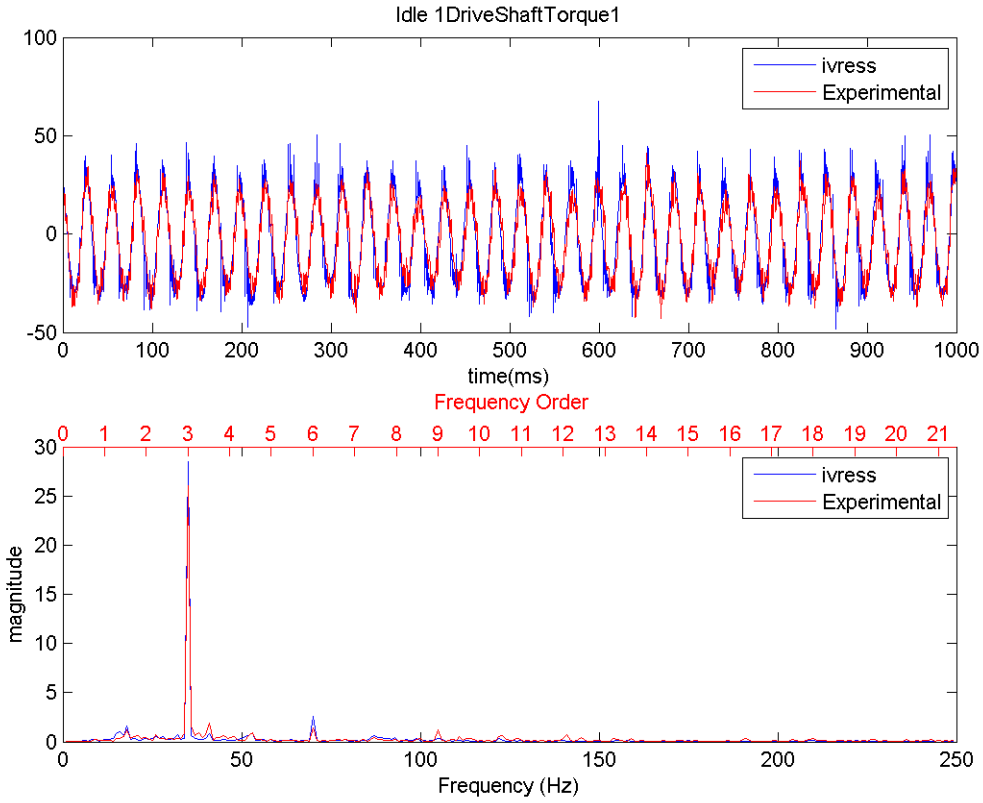

Figure 4.22 Drive shaft torque in the idle operation range with pinion tooth damping increased to $4 \times 10^{13} N/m$ instead of $2 \times 10^{13} N/m$ in the baseline

4.4 Drive Shaft

4.4.1 Drive Shaft Torsional Stiffness

In this simulation, the drive shaft torsional stiffness is increased to 7500 N/rad instead of 5674 N/rad. The shaft stiffness is modeled by adding two rotational springs at both ends of the shaft having an equivalent torsional stiffness to the shaft. The responses show no significant change for the drive shaft angular velocity or the drive shaft torque.

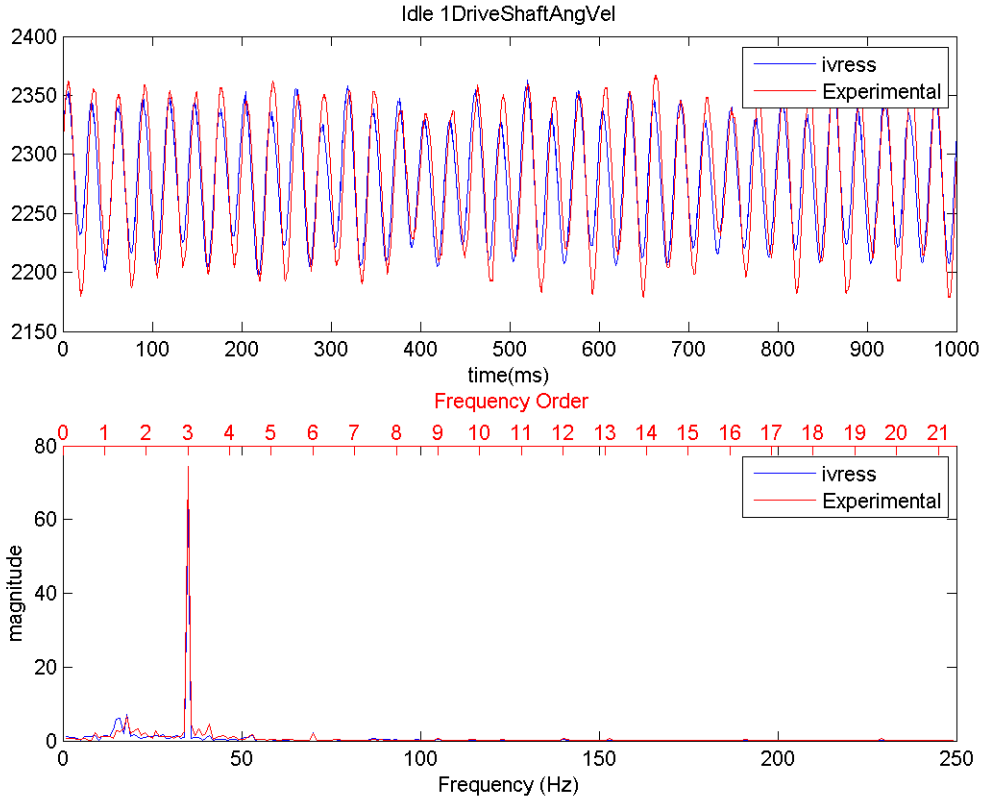

Figure 4.23 Drive shaft angular velocity in the idle operation range with drive shaft torsional stiffness increased to 7500 N/rad instead of 5674 N/rad

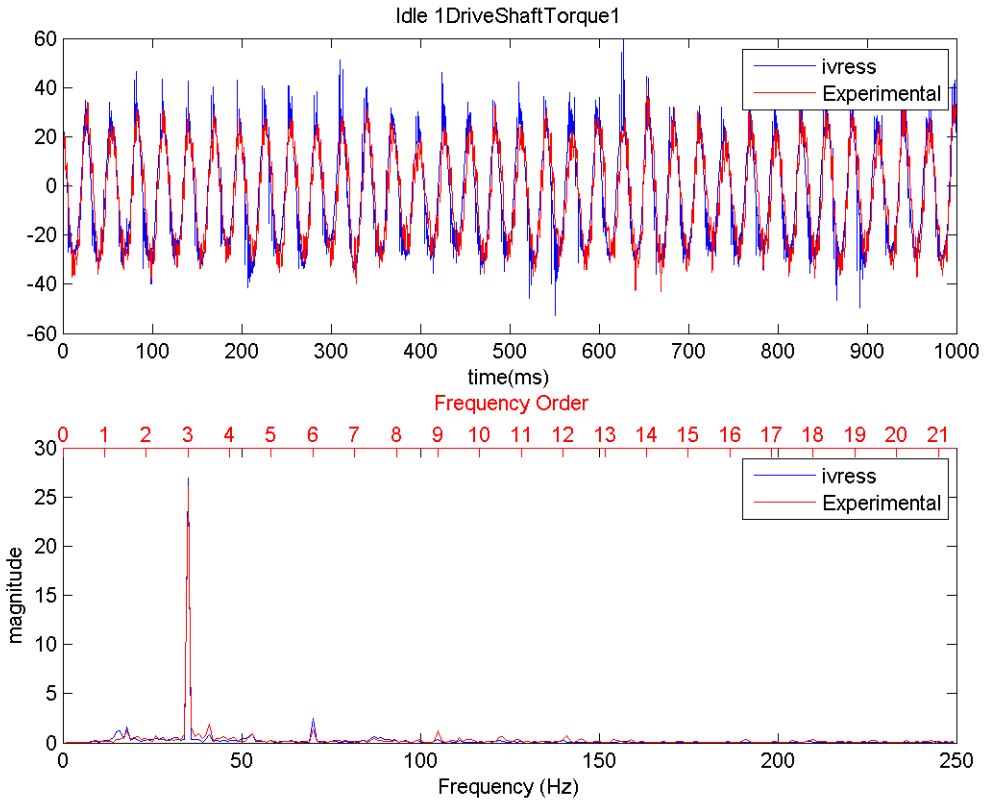

Figure 4.24 Drive shaft torque in the idle operation range with drive shaft torsional stiffness increased to 7500 N/m instead of 5674 N/m

4.4.2 Torsional Damping

Changing the drive shaft torsional damping does not affect the system response. Figure 4.25 and Figure 4.26 show the drive shaft angular speed velocity and torque respectively, when decreasing the rotational damping of the drive shaft from 45 $N.s/rad$ to 35 $N.s/rad$.

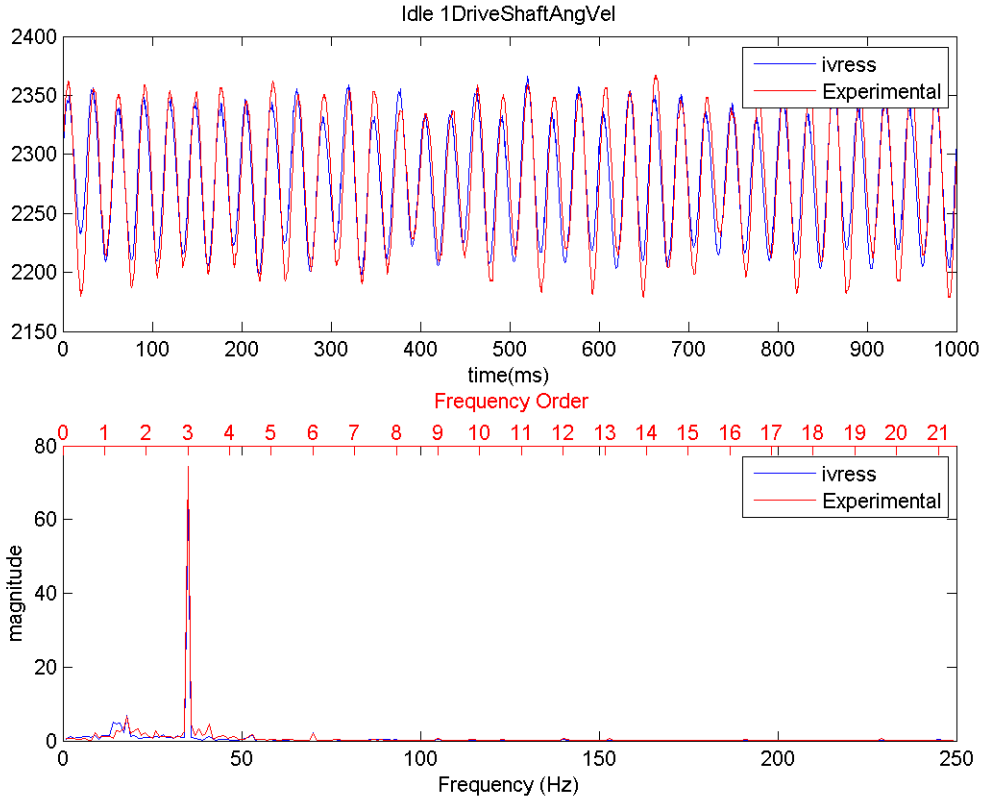

Figure 4.25 Drive shaft angular velocity in the idle operation range with drive shaft damping decreased to 35 $N.s/rad$ instead of 45 $N.s/rad$ in the baseline

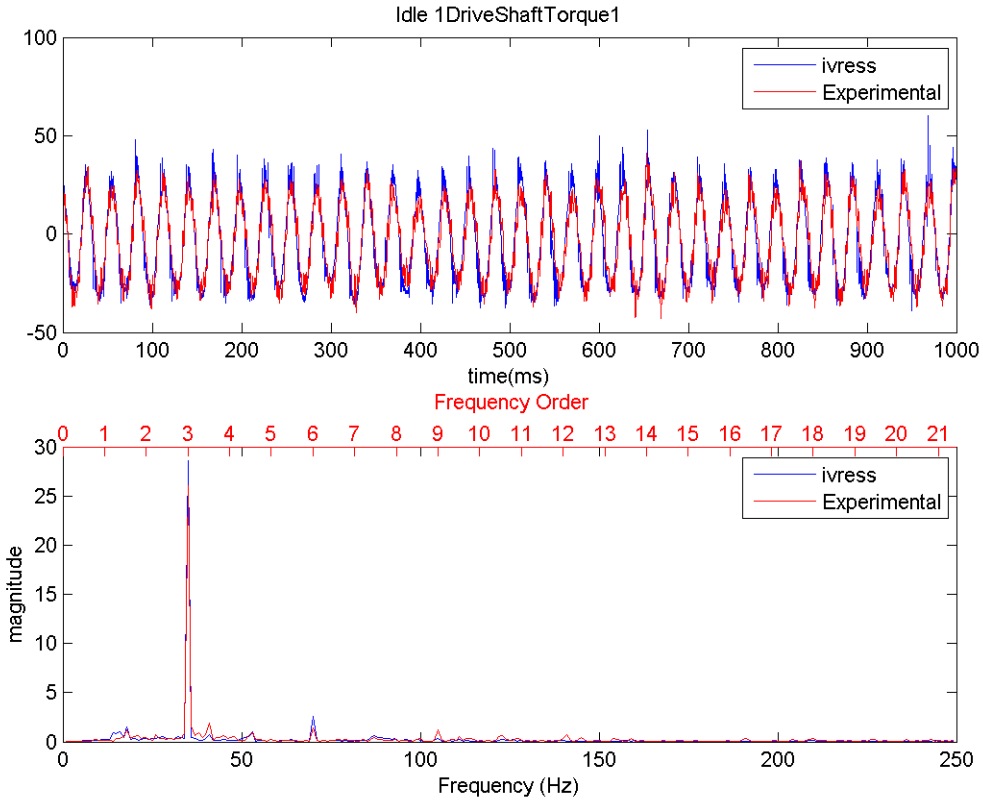

Figure 4.26 Drive shaft angular velocity in the idle operation range with drive shaft damping decreased to 35 N.s/m instead of 45 N.s/m in the baseline

4.5 Turbine Shaft

4.5.1 Turbine Shaft Torsional Stiffness

In this simulation, the turbine shaft torsional stiffness is decreased to 1000 N/rad instead of 1442 N/rad. The shaft stiffness is modeled by adding a spring at the turbine end of the shaft having an equivalent stiffness as desired. The responses show no significant change for the drive shaft angular velocity or the drive shaft torque.

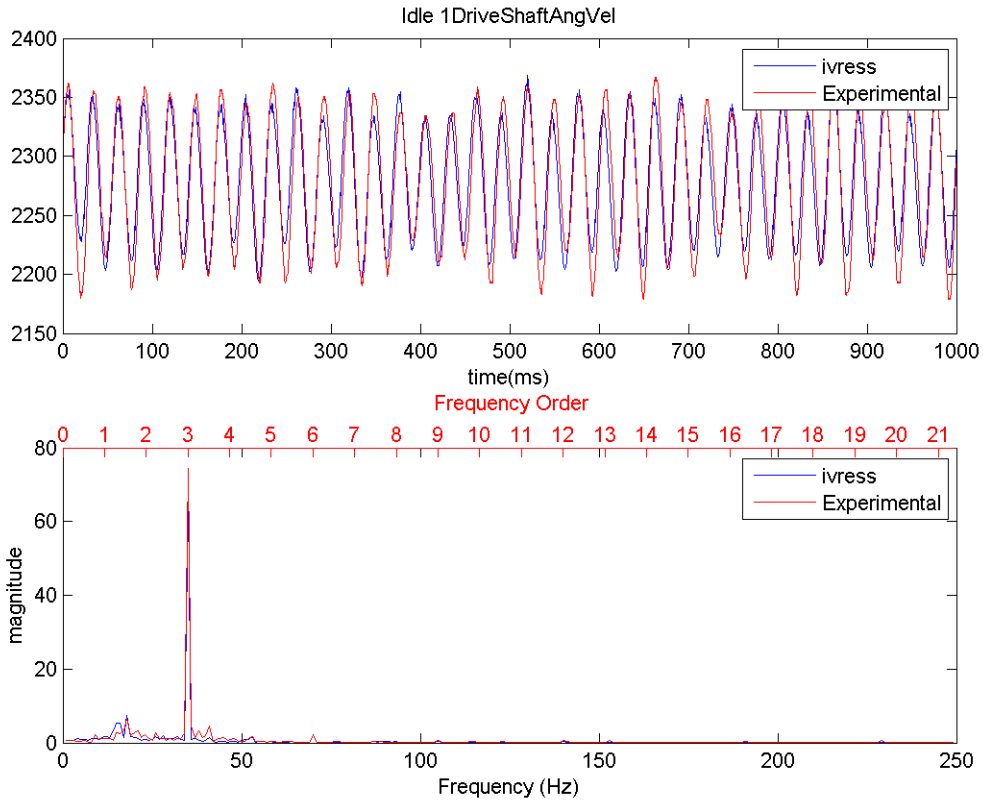

Figure 4.27 Drive shaft angular velocity in the idle operation range with turbine shaft torsional stiffness decreased to 1000 N/rad instead of 1442 N/rad

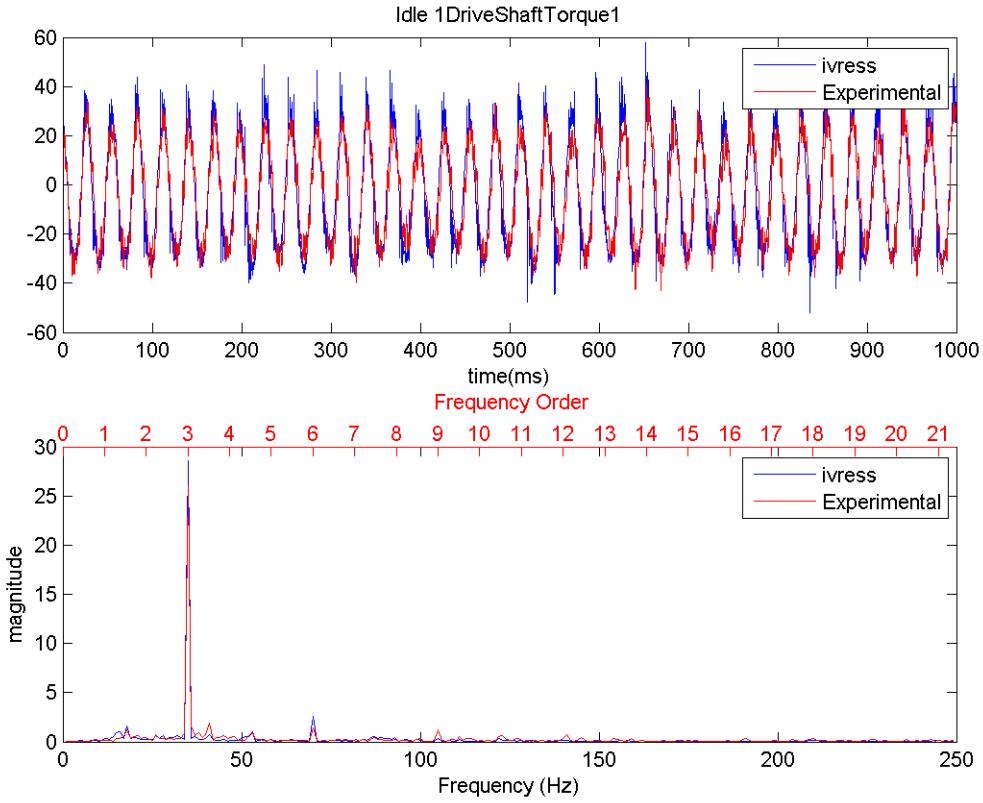

Figure 4.28 Drive shaft torque in the idle operation range with turbine shaft torsional stiffness decreased to 1000 N/rad instead of 1442 N/rad

4.5.2 Torsional Damping

Like drive shaft torsional damping, changing the turbine shaft torsional damping does not affect the system response. Figure 4.29 and Figure 4.30 show the turbine shaft angular speed velocity and torque respectively, when decreasing the rotational damping of the drive shaft from 4 $N.s/rad$ to 2 $N.s/rad$.

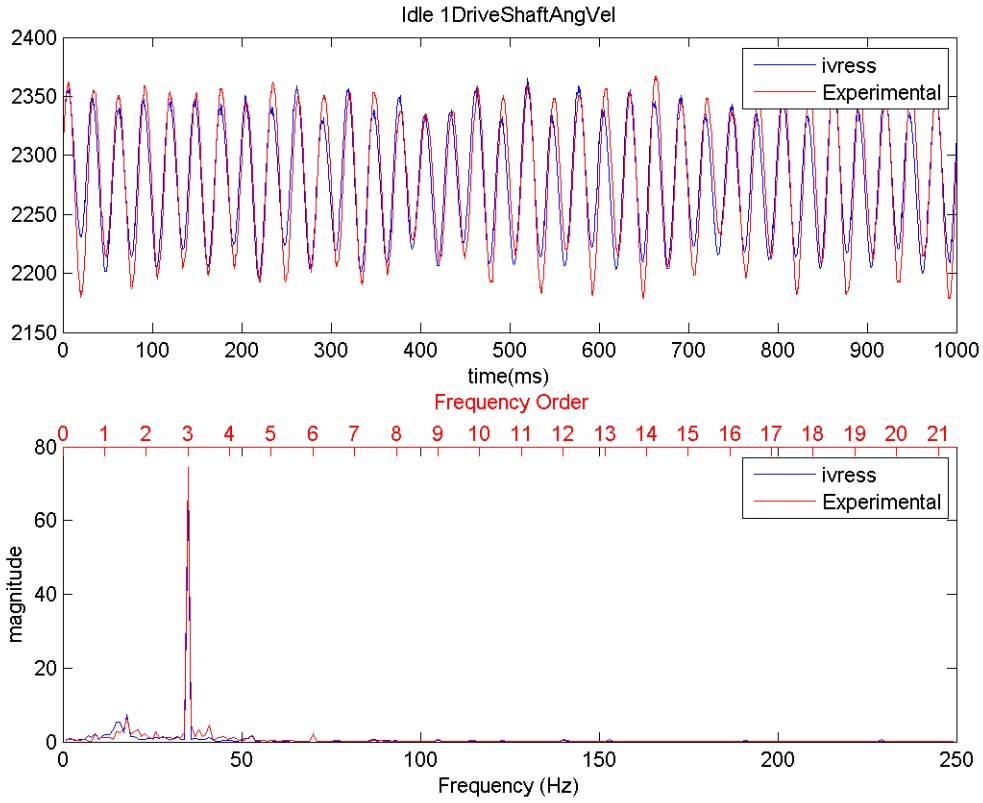

Figure 4.29 Drive shaft angular velocity in the idle operation range with turbine shaft torsional damping decreased to 2 $N.s/rad$ instead of 4 $N.s/rad$

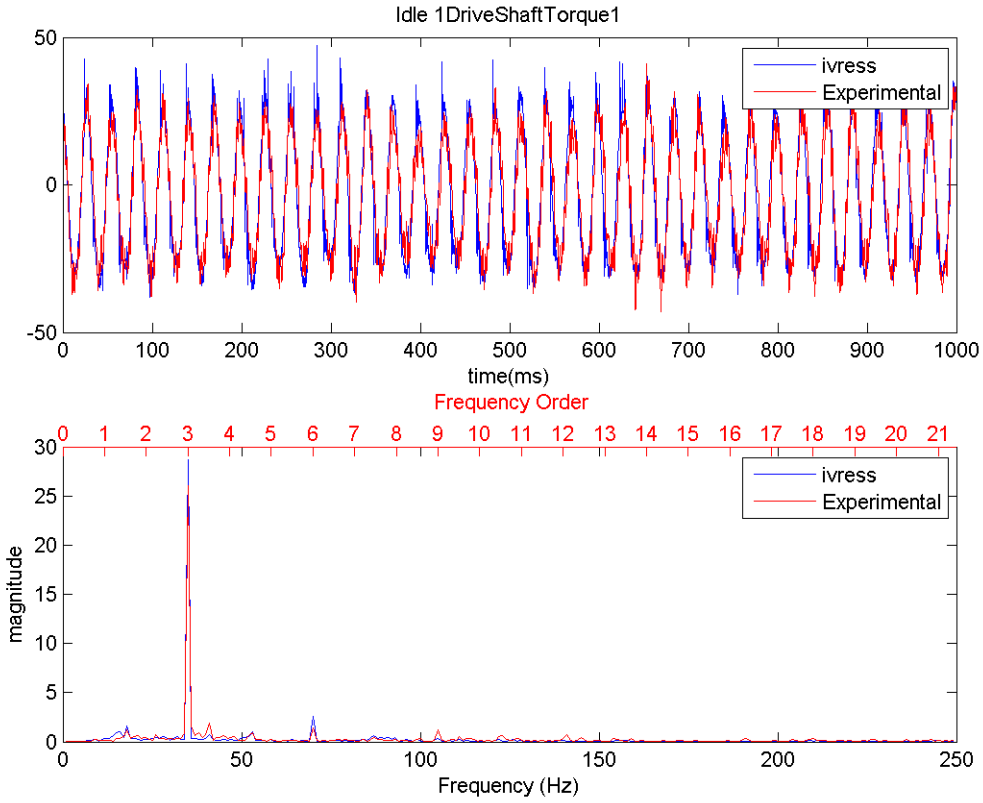

Figure 4.30 Drive shaft torque in the idle operation range with turbine shaft torsional damping decreased to 2 $N.s/rad$ instead of 4 $N.s/rad$

4.6 Conclusion and Discussion

The effect of changing the system parameters on the belt-drive response was studied in this chapter. By observing the response due change of different parameters, it was shown that the main components affecting the response of the system are the tensioner arm and the belt parameters, namely:

- Tensioner arm viscous damping
- Tensioner arm coulomb friction torque
- Belt axial stiffness
- Belt Bending Stiffness
- Belt Coefficient of friction

Results are shown in Figure 4.1 to Figure 4.30 and a comparison summary is shown in Table 4.1.

Increasing the tensioner arm viscous damping, Tensioner arm coulomb friction torque, or decreasing belt axial stiffness will result in significant decrease in amplitude due to the energy dissipated due to damping/friction.

Increasing pinion tooth backlash does not have a significant effect on the response, until the backlash is large enough for the gear teeth to bounce and start impacting each other. The main response frequencies values and amplitudes remain unchanged, however; in the torque time domain, some spikes appear due to the impacts. Likewise, decreasing the belt coefficient of friction does not have a significant effect on the system's response until it is low enough such that the belt starts slipping over the pulley. Hence the amplitude of the drive shaft angular velocity starts to decrease due to slip.

Table 4.1 Summary of parameters sensitivity

Parameter	Change	Response Magnitude	Response Frequency
Tension arm			
•Viscous damping.	Increase	Decrease	No change
•Coulomb friction.	Increase	Decrease	No change
Belt			
•Axial damping.	Decrease	No change	No change
•Axial Stiffness	Dec rease	Decrease	No change
•Bending damping.	Increase	No change	No change
•Bending stiffness.	Increase	Decrease	Decrease
•Coefficient of friction.	Increase	Doesn't change above 0.45, but increase below 0.45	No change
•Coefficient of friction.	Decrease	Doesn't change above 0.45, but decrease below 0.45	No change
Gears			
•Gear backlash.	Increase	When backlash is big enough for gear teeth to bounce causing torque spikes	No change
•Gear tooth stiffness.	Increase	Torque spikes appears due to impact of teeth	No change
•Gear tooth damping.	Increase	No change	No change
Drive shaft			
•Torsional stiffness.	Increase	No change	No change
•Torsional damping.	Decrease	No change	No change
Turbine shaft			
•Torsional stiffness.	Decrease	No change	No change
•Torsional damping.	Decrease	No change	No change

5. STRESS CALCULATIONS

In this chapter, different stresses affecting the belt rib are studied, while in Chapter 6, the calculated stresses are used in the fatigue model. The belt ribs suffer different types of stress cycling each time the belt passes over a pulley:

- The belt suffers cycling in **axial stress** because of the torque transmitted to each pulley.
- Due to the curvature of the pulleys, **bending stress** develops in the belt each time the belt passes on a pulley the bending stress depends on the radius of curvature of the pulley, as well as the material properties of the belt.
- Since the belt rib's bottom surface tip doesn't touch the pulley, the normal force transfers from the pulley to the belt through the rib sides. Due to the wedge geometry of the belt rib and the wedge action of the pulley groove, this normal force is transferred as transverse force on the belt rib. Thus, **transverse stress** develops due to squeezing of the V-ribs in the pulley grooves.
- Finally, the belt is driving or being driven by various pulleys. The torque is transmitted from the pulley to the belt or vice versa by the means of the friction force. The friction force is the tangential force acting on a plane parallel to the belt's axis. It is modeled in the system by the asperity spring friction model which approximates coulomb friction. The belt is subjected to a **shear stress** due to this tangential friction force between the sides of the belt ribs and the pulley grooves.

5.1 Axial (Tension) Stress

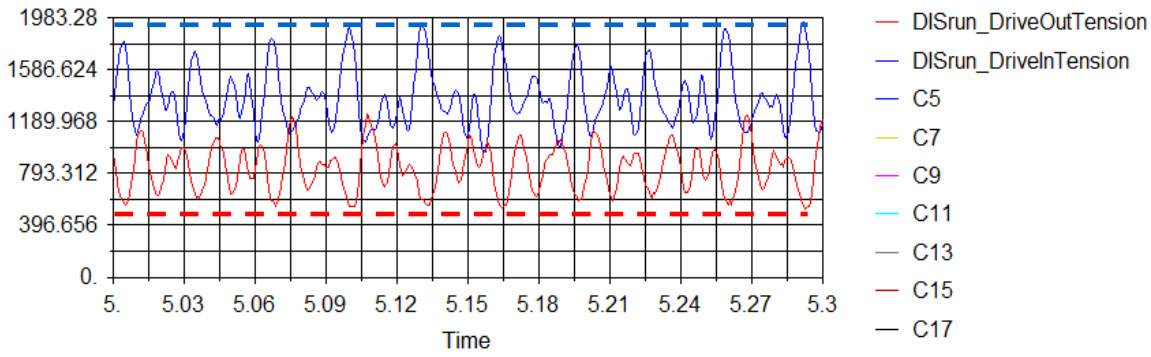

Figure 5.1 Belt span tension at the entry and exit of the drive pulley.

Axial tension varies over the pulley from the belt entry side to the belt exit side. The difference between the belt tension at both sides, as well as the diameter of the pulley and the wrap angle, determine the torque added or consumed by the pulley. Using the DIS code tension in belt spans can be predicted. An example of the DIS output is shown in Figure 5.1. Due to crank angular velocity variations, the tension in the belt span is not constant. To take the effect of the crank angular velocity variations into account, the highest magnitude at high tension side, and the lowest magnitude at the low tension (slack) side are used, instead of using the mean values.

Using the belt tension, belt strain can be calculated, using equation (5.1). Consequently, axial stress can be calculated using Hook's law (equation (5.2)). Mean and alternating stress can be calculated using equations (5.3) and (5.4) respectively.

$$\varepsilon_\theta = \frac{T_\theta}{EA} \tag{5.1}$$

$$\sigma_\theta = \varepsilon_\theta E_{rubber} \tag{5.2}$$

$$\sigma_{\theta m} = \frac{\sigma_{in} + \sigma_{out}}{2} \tag{5.3}$$

$$\sigma_{\theta a} = \pm \frac{\sigma_{in} - \sigma_{out}}{2} \tag{5.4}$$

Where:

σ_θ: The axial stress

EA: The equivalent axial stiffness of the belt

E_{rubber}: Rubber's Young's modulus

T: Belt tension

ε: Belt strain

$\sigma_{\theta m}$: Mean axial stress

$\sigma_{\theta a}$: Alternating axial stress

The main challenge in this step is to determine the Young's modulus (E) of the rubber rib tip of the belt. Nassiri 2010[12] estimated Young's modulus for rubber in 6PK belt to be 7.78 MPa. T. Ha Anh and T. Vu-Khanh [11], on the other hand, studied the variation of Young's Modulus value with the aging of time and temperature. The results of the study indicated that the belt Young's modulus varied from 3.51 to 10.93 MPa (Table 5.1). Such variation affects the accuracy of belt life prediction. For this study, Young's modulus was taken as 7 MPa for the sake of comparison between different belt-drive configurations. For more accurate belt life estimation, experiments should be conducted to determine belt's rubber Young's modulus and its range of variation over the belt life.

Table 5.1 Young's modulus variation for polychloroprene with the aging of time and temperature

Aging temperature (°C)	100					120			
Aging time (hrs.)	12	24	48	96	168	24	48	96	168
E (MPa)	3.51	3.6	3.69	3.68	4.84	4.05	4.74	6.96	10.93

5.2 Bending Stress

Bending stress acts in the axial belt direction. Thus, bending stress can be algebraically added to the axial stress. Figure 5.2 shows a sketch that illustrates the distribution of the bending stress over the belt's cross-section and it's superposition with the axial stress.

Bending stress depends on the pulley radius and the belt material properties. As the belt thickness is much smaller than any of the pulley diameters, the following assumptions can be made:

1. The bending stress distribution is linear over thickness of the belt
2. The radius of curvature is constant and equal to the pulley pitch radius.

Given the above assumptions, the bending stress can be expressed using equation (5.5).

$$\sigma_B = \frac{E_{rubber} y}{R} \tag{5.5}$$

$$\sigma_{Bm} = \frac{\sigma_B}{2} \tag{5.6}$$

$$\sigma_{Ba} = \pm \frac{\sigma_B}{2} \tag{5.7}$$

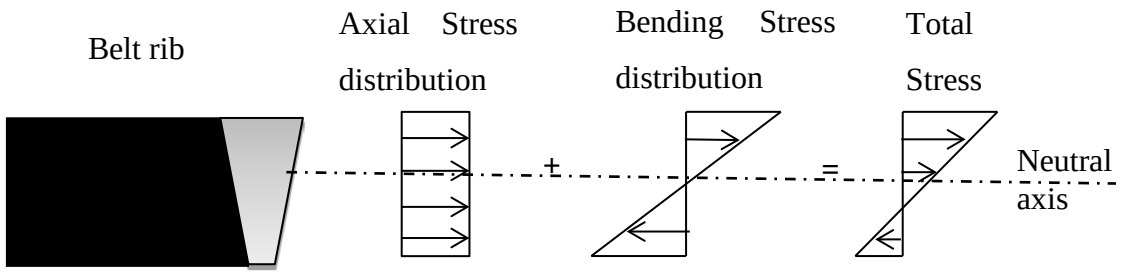

Figure 5.2 Bending stress distribution and superposition

Where:

E_{rubber}= Young modulus for rubber

y= The height of the rib from the chords

R= Pulley pitch radius

5.3 Transverse Stress

As a result of the normal contact force between the pulley and the belt, and the wedge shape of the belt V-rib, a transverse force develops. This force will tend to squeeze the belt rib to try to fit it in the pulley groove consequently developing a transverse stress. The DIS code can predict the normal force between the pulley and the belt. The normal force with the belt geometry can be used to calculate the transverse force as well as the transverse stress. Figure 5.3 shows the time history of the normal force acting from the pulley on one element of the belt as it travels through the different pulleys. A time window was chosen so that the results shown for one complete cycle around the drive.

Figure 5.4 shows a cross section of the V-rib of the belt with transvers forces applied on it. *Transverse force* (F_z) is defined as the force perpendicular to the surface of the belt rib side. The *normal force* (F_N) is defined as the radial force acting from the

pulley on the belt, calculated from the DIS code. DIS code calculates F_N applied on a belt area of length equals to one element length and width equals to the whole belt width.

Assuming equal load sharing between ribs, each rib will share a normal force (F_n) equals to:

$$F_n = \frac{F_N}{number\ of\ ribs} \tag{5.8}$$

As the belt rib carries the load on both sides and due to symmetry, each side will carry half the load only (i.e. $F_n/2$).

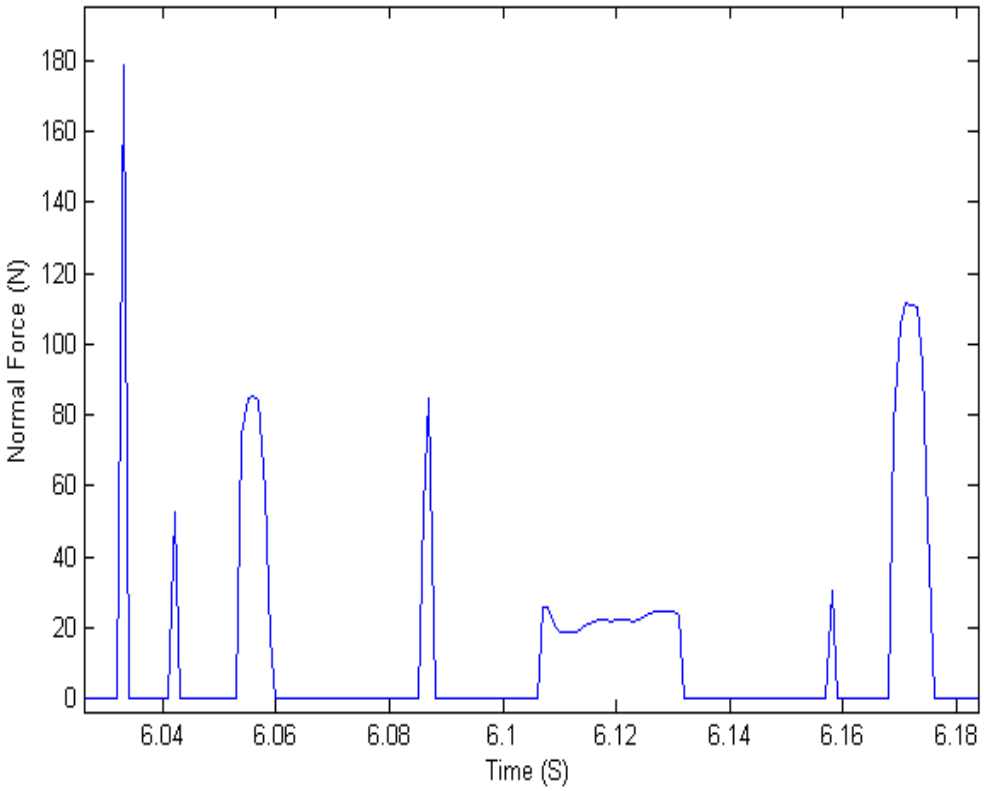

Figure 5.3 DIS results for the calculated normal force on one belt element varying over time as it travels around the belt-drive.

F_z has two components in the normal and axial directions of the pulley. The two components are defined as:

$$F_Z \sin\theta = \frac{F_n}{2} \tag{5.9}$$

$$F_Z \cos\theta = \frac{F_n}{2 \times \tan\theta} \tag{5.10}$$

Where:

θ: Half the belt rib wedge angle (20 degrees for the PK belt section)

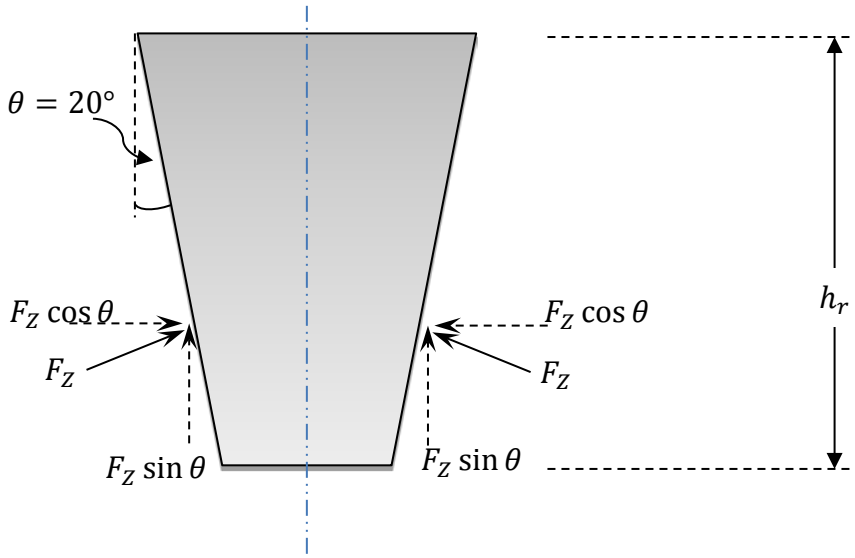

Figure 5.4 Transverse force acting on the belt V-rib cross section due to normal force acting from the pulley in the rib

Hence we can use the F_N calculated by the DIS code and employ it in Equations (5.8) and (5.12) to calculate F_Z. Knowing F_Z and the geometry of the belt, the transverse stress (σ_Z) can be calculated as shown in Equation (5.11).

$$\sigma_Z = \frac{F_Z \cos\theta}{h_r \times l} \tag{5.11}$$

Where:

h_r: Height of the V-rib

l: Length of the belt element in the DIS code

Transverse stress will always be negative, as it is a compression stress. It only happens on the grooved side, in other words, when the belt is front wrapped. The back wrapped pulleys are facing the flat side of the belt, and hence the normal force will not develop any transverse stress. Since we are only interested in the rib stresses so the back wrapped pulleys are not taken into account in the transvers stress calculation.

As the free span is not in contact with any pulley, it will have no applied normal force, and consequently, it will not have a transverse force or transverse stress. Hence the belt enters and exits the pulley with zero transverse stress. The transverse stress (σ_z) when the belt is in contact with the pulley is calculated as shown in Equations (5.8) through (5.11). The mean and the alternating transverse stresses can be calculated using equations (5.12) and (5.13).

$$\sigma_{Zm} = \frac{\sigma_Z}{2} \tag{5.12}$$

$$\sigma_{Za} = \pm\frac{\sigma_Z}{2} \tag{5.13}$$

Where:

σ_Z: Maximum transverse stress

σ_{Zm}: Mean transverse stress

σ_{Za}: Alternating transverse stress

The normal force is not always the same for each cycle. To take the variation into account, and to avoid the dummy spikes in the force distribution, Normal force was observed on a specific pulley for one second with a sampling rate of 1000 Hz. Each cycle, the maximum force was observed, and then the maximums are averaged, and the average maximum is used in the calculations.

5.4 Shear Stress

The belt main function is to transmit power between different pulleys, some of them are driving and others are driven. Power is transmitted within the belt by the means of axial forces, while it is transmitted between the belt and the pulleys by the means of friction forces, which is also referred to as tangential or shear forces. According to equation (5.14), the tangential force depends on the normal force between the belt and the pulley as well as the coefficient of friction between the belt and the pulley.

$$F_T = \mu F_N \tag{5.14}$$

Where:

F_T : Tangential force

F_N : Normal force

μ : Coefficient of friction

Given the coefficient of friction, the DIS code can predict the tangential force. The coefficient of friction is tuned in the model to match the experimental results. Figure 5.5 shows the tangential force on one belt element, as it travels around the belt-drive, with respect to time. The time window was chosen so that the belt element travels about one complete belt cycle. Hence the plot shows the shear force distribution over different pulleys. DIS code calculates F_T applied on a belt area of length equals to one element length and width equals to the whole belt width. Assuming equal load sharing between ribs, each rib will share a tangential force (F_t) equals to:

$$F_t = \frac{F_T}{number\ of\ ribs} \tag{5.15}$$

As the belt rib carries the load on both sides and due to symmetry, each side will carry half the load only (i.e. $F_t/2$).

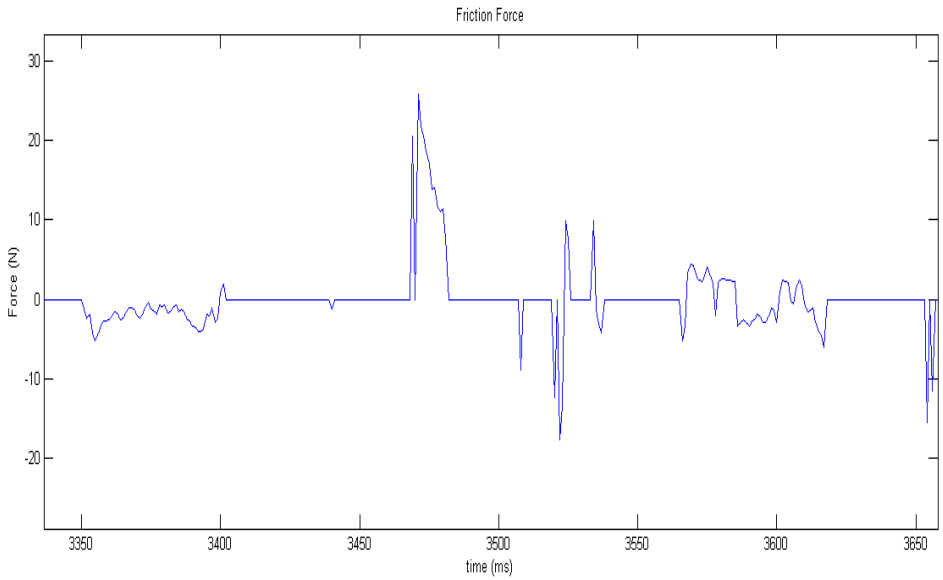

Figure 5.5 Tangential force predicted by DIS code for one element over time

As the tangential forces change with respect to time on each pulley, it was proposed to calculate the shear stress using the maximum shear force in order to account for the most extreme condition. However, the maximum is not the same at each cycle, moreover it may spike at one cycle to a very high value that will never happen again in other cycles. As a result, a code was written to track the maximum shear force at each pulley during the one second of test at a sampling rate of 1000 Hz. Then the maximum values obtained are averaged to reduce the effect of the non-dominant spikes.

Shear stress develops due to the application of the tangential friction force on the sides of the belt ribs. Shear stress is very small at the idler pulleys as there is negligible power transmitted from or to them. On the other hand, shear stress value is large at the crank and the drive pulleys since power is transmitted from or to them.

Given the tangential force acting on the belt and the belt geometry, the shear stress can be calculates as:

$$\sigma_\tau = \frac{F_t \cos\theta}{2 \times h_r \times l} \tag{5.16}$$

As the free span is not in contact with any pulley, it will have no applied tangential force, and consequently, it will not have a shear stress. Hence the belt enters and exits the pulley with zero shear stress. The value of shear stress (σ_τ) when the belt is in contact with the pulley is calculated as shown in Equations (5.15) and (5.16). The mean and the alternating transverse stresses can be calculated using equations (5.17) and (5.18).

$$\sigma_{\tau m} = \frac{\sigma_\tau}{2} \tag{5.17}$$

$$\sigma_{\tau a} = \pm\frac{\sigma_\tau}{2} \tag{5.18}$$

Where:

σ_τ: Maximum shear stress

$\sigma_{\tau m}$: Mean transverse stress

$\sigma_{\tau a}$: Alternating transverse stress

5.5 Equivalent Uniaxial Stress

To employ the fatigue model, uniaxial stress model is required; however the belt stress is multi-axial. Hence, it is required to find an equivalent uniaxial stress that combines the effect of the multi-axial stresses. Using Sine's theory [8, 22], the equivalent mean axial stress is given by:

$$\sigma_m = \sigma_{\theta m} + \sigma_{Bm} + \sigma_{Zm} \tag{5.19}$$

$$\sigma_a = \sqrt{\frac{(\sigma_{a1} - \sigma_{a2})^2 + (\sigma_{a2} - \sigma_{a3})^2 + (\sigma_{a3} - \sigma_{a1})^2}{2}} \tag{5.20}$$

Where:

σ_m: The equivalent uniaxial mean stress.

σ_a: The equivalent uniaxial alternating stress

$\sigma_{a1}, \sigma_{a1}. \sigma_{a1}$: The principal multi-axial alternating stresses

In the next chapter, the uniaxial equivalent mean and alternating stresses will be used to calculate the fatigue life of the belt.

6. BELT LIFE PREDICTION

The multibody dynamics belt-drive model can be used to predict the system dynamic response, including time-histories of belt tension, belt-span transverse vibrations, normal and tangential forces between the belt and the pulleys, pulley angular velocities, pulley hub loads, torque transmitted through shafts and the tensioner arm angle, under various operating conditions. This information can be used to determine if the belt-drive can withstand those operating condition without failure. For example, the pulley mounting points must be able to support the hub loads without experiencing static or fatigue failures. In this chapter we will use the information generated by the multibody dynamics belt-drive model to predict one of the most common failure modes of the belt-drive, which is failure due to belt fatigue. Specifically, in this chapter a belt fatigue life prediction model will be presented.

Section 6.1 describes the failure criteria used to determine belt fatigue life. In Section 6.2 an introduction about fatigue including ***High Cycle Fatigue Model (HCF)*** and ***Low Cycle Fatigue (LCF)*** model, the difference between both models, and the reasons behind choosing the HCF model are presented. In Section 6.3 more details are presented on the methodology of the HCF model. Section 4 shows how the multibody dynamic code results can be used in the fatigue life model to estimate the life-time of the belt drive.

6.1 Failure Criteria

Failure criteria of the belt is described by appearance of cracks in the belt rib tip [8]. When cracks appear, the belt is considered “due for change” as per the advice of

most belt manufacturers. Although the belt chords may not have ruptured and the belt is still functioning, the belt is still considered to have failed. This is because at this point the rubber will start to be torn, so that the belt can no longer transmit power.

6.2 Fatigue Concept

Fatigue failure is the failure of the material due to cycling load, see Figure 6.1. This process passes through two main phases; crack initiation and crack propagation. Depending on the value of the alternating stress, the material would fail after certain number of cycles, the smaller the alternating stress is, the more life cycles the material can withstand. Below certain value of stress, the material tends to operate for infinite number of cycles, such stress is referred to as ***endurance stress*** (σ_e)

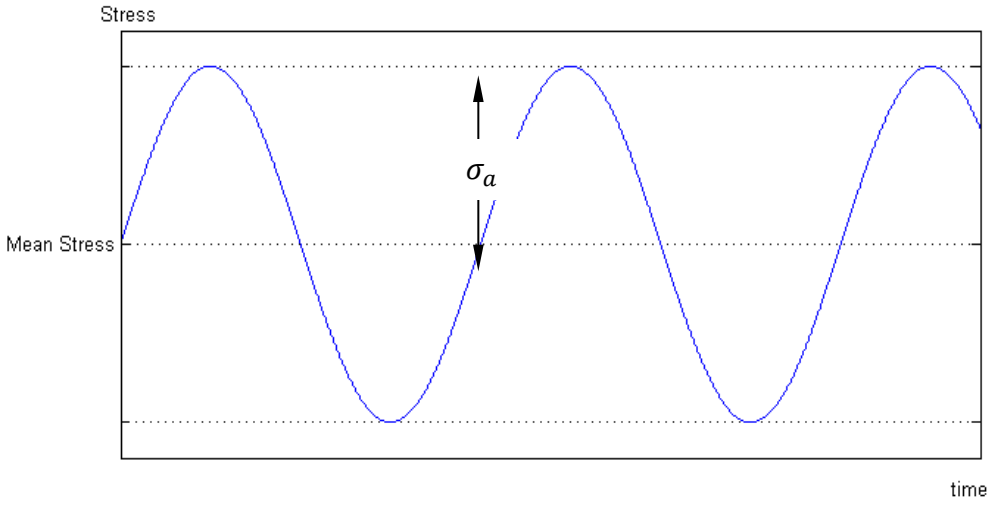

Figure 6.1 Cycling Stress

6.2.1 S-N Curve

The S-N curve is a diagram which shows the relation between the magnitudes of the alternating uniaxial stress applied on the material (σ) and number of cycles (N_f) that

the material can withstand under this stress. Figure 6.2 shows σ as a function of number of reversals ($2N_f$).

The curve can be defined by two main slopes, one of which is the ***plastic strain slope*** (c) and the other is the ***elastic strain slope*** (b). The intercept of the extension of the elastic region and the $2N_f$=1 vertical axis is called the ***fatigue strength (σ_f)***. The slope, b, of the elastic strain region of the curve is called the ***fatigue strength exponent***.

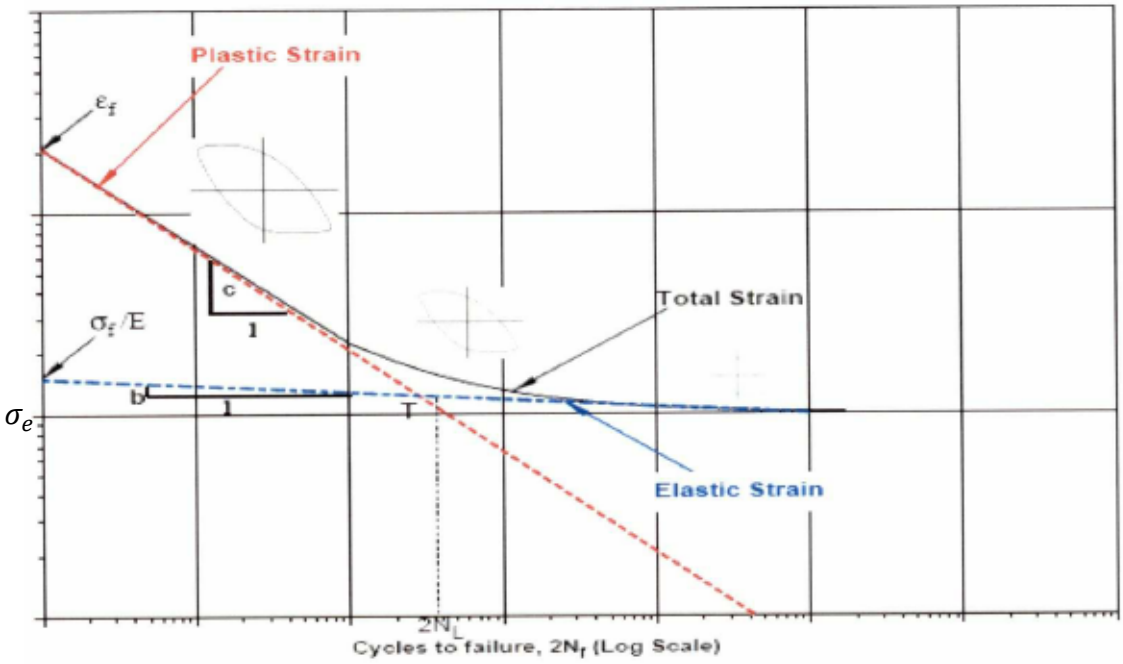

Figure 6.2 S-N Curve (Ref. [8])

As it appears in Figure 6.2, when the alternating stress is much higher than the endurance stress (σ_e), the curve is steeper, with a higher slope (plastic strain slope). This simulates the operation of the material in plastic strain region. This type of fatigue is called ***Low Cycles Fatigue*** (LCF). LCF can be described by Coffin-Manson law as follows (first proposed in 1960's) [8]:

$$\varepsilon_p = \varepsilon_f (2N_f)^c \tag{6.1}$$

Where:

ε_p: Independent plastic strain amplitude

ε_f: Fatigue ductility coefficient

c: Fatigue ductility exponent

N_f: The number of cycles for failure ($2N_f$ is the number of reversals for failure)

On the other hand, when the alternating stress is closer to the endurance stress, the curve tends to be more flat with a smaller slope. This simulates the operation of the material in the elastic strain region. This type of fatigue behavior is called ***High Cycles Fatigue*** (HCF). HCF can be described by Basquin relation, proposed in 1910 [8, 12, 23]:

$$\sigma_a = \sigma_f (2N_f)^b \tag{6.2}$$

Where:

σ_p: Alternating stress

σ_f: Fatigue strength coefficient

b: Fatigue strength exponent

N_f: The number of cycles for failure

When the alternating stress is below σ_e, the material tends to have, theoretically, infinite number of cycles before it suffers a failure.

In a belt drive, the belt chords (made usually from polyester or nylon) have much higher Young's modulus than the belt rubber (usually made from volcanized rubber). This limits the belt chords from straining as much as the rubber under the same tension force, and hence, the chords act as the main tension carrier. As the chords and the rubber are connected in parallel, they have to have the same strain. In this case, the chords will limit the rubber strain at very low values, and the rubber will always operate in the elastic zone. Hence *high cycles fatigue* model is adopted for the belt rubber.

6.2.2 Effect of Mean Stress

In equations (6.1) and (6.2) above, the stress was considered to be cycling around zero stress. When the material suffers cycling stress around non zero mean stress, the fatigue life will be affected [23]. It was observed that if the mean stress is +ve (tension), the fatigue life decreases, while if the mean stress (σ_m) is -ve (compression), the fatigue life increases. Figure 6.3, shows the effect of the mean stress on the fatigue life.

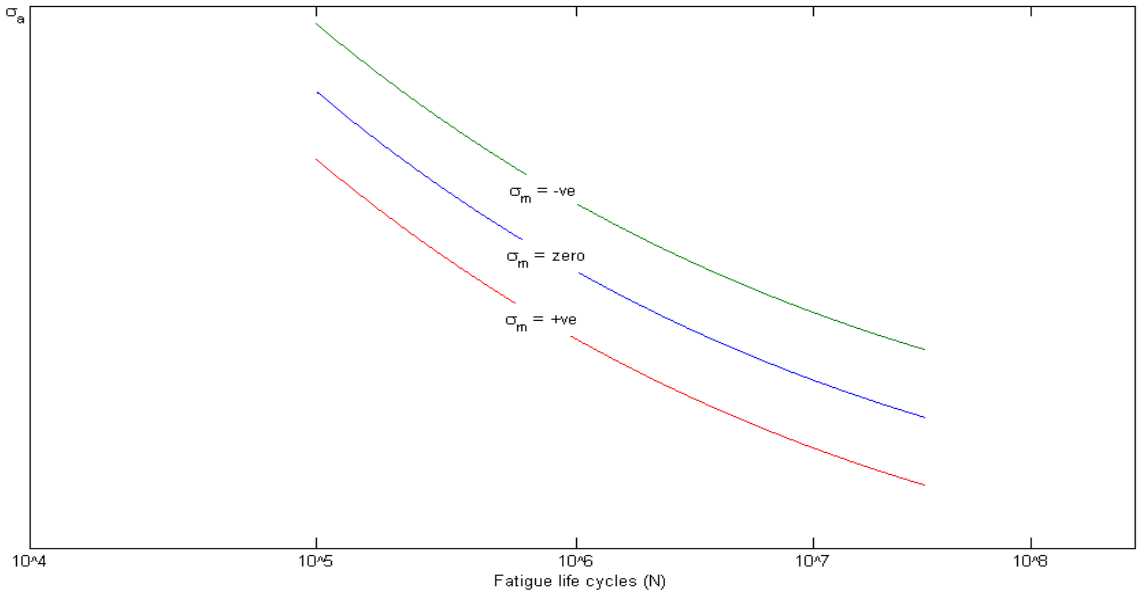

Figure 6.3 Effect of mean stress on fatigue life on S-N curve

The Basquin relation, equation (6.2), is further modified to account for the mean stress. Equation (6.3) below represents the modified equation:

$$\sigma_a = (\sigma_f - \sigma_m)(2N_f)^b \tag{6.3}$$

6.3 Fatigue Model

As discussed in the previous section, the HCF model is employed in this study. The modified Basquin relation, equation (6.3) is employed to relate the stresses to the fatigue life. Using equation (6.3) we can calculate the number of cycles to failure:

$$N_f = \frac{1}{2}\left\{\frac{\sigma_a}{\sigma_f - \sigma_m}\right\}^{\frac{1}{b}} \tag{6.4}$$

The above relation describes single cycling action, however; the belt passes through all the pulleys (more than one) in the belt-drive each cycle. Each pulley would be considered as a different cycling load, Thus Miners ***Linear Damage Rule*** (LDR) [8, 24] will be used as described in the next section.

6.4 Cumulative Damage Theory

When the belt is subjected to different loadings, each loading will consume a fraction of the belt life. Consider at some loading condition, the belt useful life is $\boldsymbol{N_{f1}}$ cycles, while the belt operates at this loading conditions for $\boldsymbol{n_1}$ cycles, then this loading event caused a fraction of damage to the belt as shown in equation (6.5).

$$d_1 = \frac{n_1}{N_{f1}} \tag{6.5}$$

Where

$$N_{fi} = \frac{1}{2}\left\{\frac{\sigma_{ai}}{\sigma_{fi} - \sigma_{mi}}\right\}^{\frac{1}{b}} \tag{6.6}$$

When other k loading events take place, they cause different amounts of damage $d_2, d_3, \ldots, d_k$ according to their loading conditions. The total cumulative damage (D) can be calculated by ***Linear Damage Rule*** (LDR) introduced by Miners in 1945 [8, 24]:

$$D = \frac{n_1}{N_{f1}} + \frac{n_2}{N_{f2}} + \cdots + \frac{n_k}{N_{fk}} = \sum_{i=1}^{k} \frac{n_i}{N_{fi}} \tag{6.7}$$

The failure criteria will be when the summation of the partial damage is greater or equal to one:

$$\sum_{i=1}^{k} \frac{n_i}{N_{fi}} \geq 1 \tag{6.8}$$

In the case of our study, different loadings are represented by different pulleys. Each of the pulleys exerts different values of stresses on the belt. However, in this case the belt has the same number of cycles over all the pulleys. This implies Equation (6.9).

$$n_1 = n_2 = n_3 = \cdots = n_k \tag{6.9}$$

Hence, the cumulative damage rule for one cycle is given by:

$$D|_{n=1} = \frac{1}{N_{f1}} + \frac{1}{N_{f2}} + \cdots + \frac{1}{N_{fk}} = \sum_{i=1}^{k} \frac{1}{N_{fi}} = \frac{1}{N_F} \tag{6.10}$$

$$\Rightarrow N_F = \frac{1}{D|_{n=1}} \tag{6.11}$$

Where N_F is the number of the useful life cycles for the system. Hence, the equivalent life cycles can be determined using Equations (6.6), (6.10) and (6.11).

Finally the time to failure can be calculated using Equation (6.12):

$$h_f = \frac{N_F \ L}{\pi D \ (RPM)(60)} \tag{6.12}$$

Where:

h_f: The number of hours to failure

N_F: Number of cycles to failure due to all the loads

L: Belt length (m)

D: Diameter of crankshaft pulley (m)

RPM: Crank shaft angular velocity (rpm)

6.5 Duty Cycle

The belt doesn't essentially run a constant speed and load (especially in automotive applications), but it runs over a duty cycle. To estimate the life time of a belt,

the duty cycle needs to be known. Suppose we have a duty cycle of total time TT with number of operation ranges K. Each operation range lasts an amount of time ΔT_j, where $j = 1{:}\,K$. Let h_{fj} be the life time (in hours) of the belt operating at operation range j, the total lifetime of the belt is equal to:

$$System\ Belt\ life = \frac{1}{\sum_{j=1}^{k} \frac{\Delta T_j}{T} \cdot \frac{1}{h_{fj}}} \tag{6.13}$$

6.6 Summary of Belt Fatigue Life Solution Procedure

Figure 6.4 shows a flow chart of the belt fatigue life prediction model. The model is defined by the geometry of the belt-drive and the physical properties. Once the information is entered, DIS code calculates the different forces applied on the belt. The output of the DIS code is used to calculate the belt stresses and the fatigue life for each pulley in the system. Then *Miner's Linear Damage Rule* (LDR) is applied to calculate the combined effect of all the pulleys in the belt-drive on the belt fatigue life.

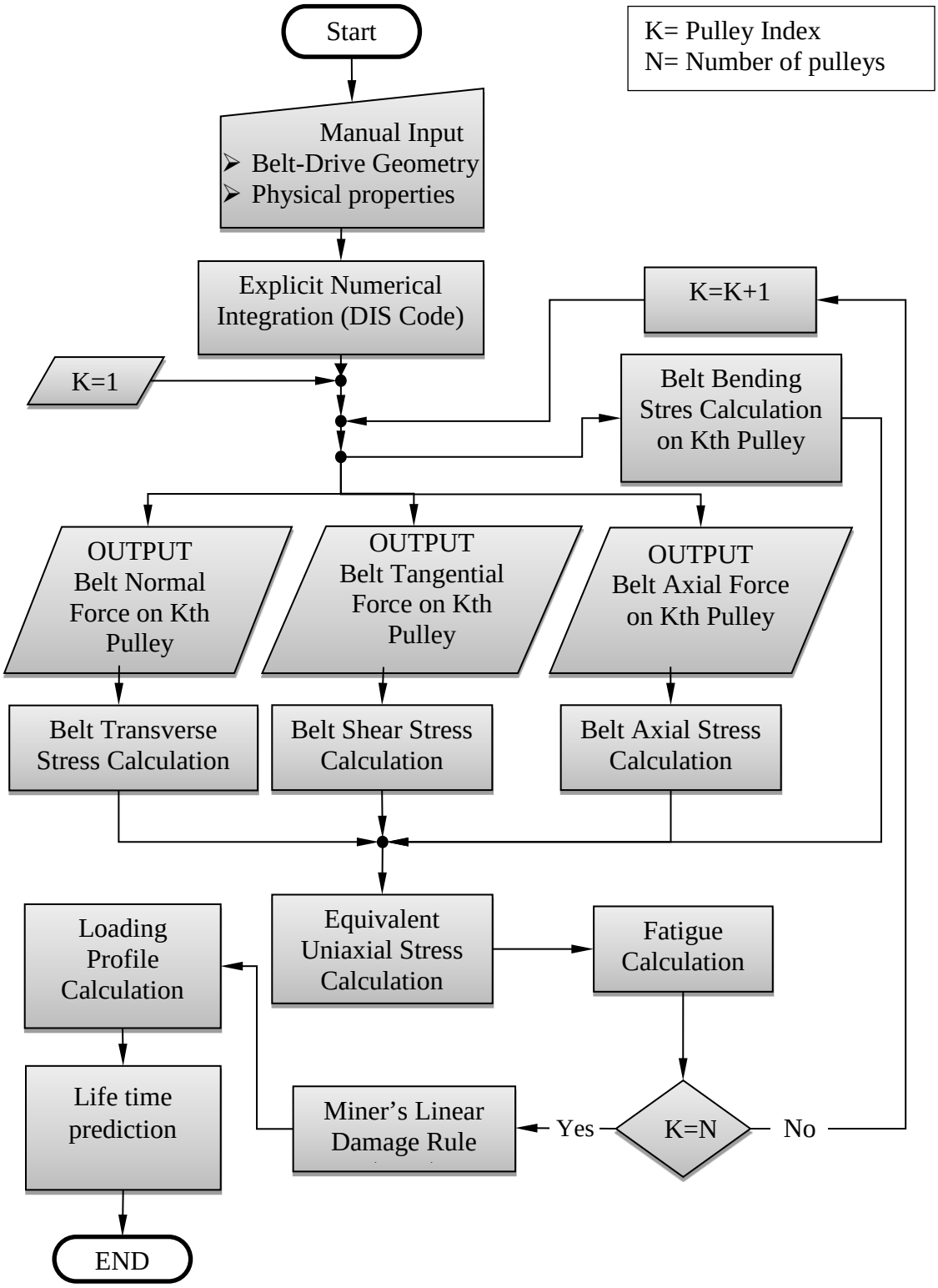

Figure 6.4 Flow Chart of the belt fatigue life prediction model

6.7 Results and Discussion

To calculate the fatigue life-time of the belt, fatigue properties should be known. Fatigue properties are calculated by running many experiments on different belt specimen [23]. As the fatigue behavior depends on many criteria such as surface finish, manufacturing flaws and defects, results are not always repeatable. The best practice is to collect data from many tests and try to average the results to get the closest estimate. For this study the fatigue strength coefficient was taken as **10 MPa** and the fatigue strength exponent was taken as **-0.068** for the sake of comparison of different belt-drive configurations. For accurate belt life estimation, more experiments need to be done to estimate those two material fatigue properties. Also, recall that in Section 5.1 the belt rubber's Young's modulus was estimated to be equal to 7 MPa based on experiments performed References [11, 12].

Applying the procedure shown in Figure 6.4 to the belt-drive shown in Figure 3.1, the number of cycles to failure and time to failure for the various belt-drive operation ranges were calculated and are shown in the bottom of Figure 6.5. The figure also shows the values of different stresses (mean and alternating axial stresses, bending stress, transvers stress, shear stress and equivalent uniaxial mean and alternating stresses) applied on the belt rib. The 6 columns show the different operation ranges, as Idle, A100, B100, C100, Unloaded up and Unloaded down from left to right, respectively. The rows show different pulleys with pulley number 1 in the top and going in order to pulley number 7 in the bottom.

Mean Ax. Stress

2.39E+04	4.07E+04	4.51E+04	4.55E+04	4.14E+04	4.20E+04
2.66E+04	4.88E+04	5.33E+04	4.98E+04	4.09E+04	4.16E+04
2.62E+04	4.74E+04	4.86E+04	4.61E+04	3.98E+04	4.00E+04
3.22E+04	3.87E+04	4.19E+04	4.33E+04	4.28E+04	4.30E+04
3.05E+04	3.26E+04	3.81E+04	4.31E+04	4.38E+04	4.44E+04
2.97E+04	3.25E+04	3.54E+04	4.10E+04	4.44E+04	4.41E+04
3.02E+04	3.28E+04	3.34E+04	3.76E+04	4.16E+04	4.17E+04

Alternating Ax. Stress

1.65E+04	2.52E+04	2.34E+04	1.76E+04	5.66E+03	5.10E+03
1.38E+04	1.70E+04	1.52E+04	1.32E+04	6.10E+03	5.49E+03
1.49E+04	1.55E+04	1.55E+04	1.37E+04	7.64E+03	6.99E+03
2.09E+04	2.12E+04	2.23E+04	1.92E+04	1.07E+04	9.94E+03
2.26E+04	1.40E+04	1.69E+04	1.62E+04	9.75E+03	8.51E+03
2.25E+04	1.65E+04	1.45E+04	1.34E+04	7.40E+03	6.50E+03
2.28E+04	1.73E+04	1.17E+04	9.76E+03	5.90E+03	4.87E+03

Bending Stress

-4.12E+05	-4.12E+05	-4.12E+05	-4.12E+05	-4.12E+05	-4.12E+05
5.81E+05	5.81E+05	5.81E+05	5.81E+05	5.81E+05	5.81E+05
5.81E+05	5.81E+05	5.81E+05	5.81E+05	5.81E+05	5.81E+05
-1.26E+05	-1.26E+05	-1.26E+05	-1.26E+05	-1.26E+05	-1.26E+05
-5.21E+05	-5.21E+05	-5.21E+05	-5.21E+05	-5.21E+05	-5.21E+05
5.81E+05	5.81E+05	5.81E+05	5.81E+05	5.81E+05	5.81E+05
-5.21E+05	-5.21E+05	-5.21E+05	-5.21E+05	-5.21E+05	-5.21E+05

Transverse Stress

-3.21E+06	-4.90E+06	-5.08E+06	-4.83E+06	-3.86E+06	-3.83E+06
0.00E+00	0.00E+00	0.00E+00	0.00E+00	0.00E+00	0.00E+00
0.00E+00	0.00E+00	0.00E+00	0.00E+00	0.00E+00	0.00E+00
-8.94E+05	-9.65E+05	-1.00E+06	-9.96E+05	-1.12E+06	-1.06E+06
-2.91E+06	-3.04E+06	-3.25E+06	-3.39E+06	-3.44E+06	-3.44E+06
0.00E+00	0.00E+00	0.00E+00	0.00E+00	0.00E+00	0.00E+00
-3.71E+06	-4.47E+06	-4.79E+06	-4.93E+06	-5.15E+06	-5.18E+06

Shear Stress

1.84E+05	3.82E+05	3.82E+05	3.91E+05	3.03E+05	3.02E+05
0.00E+00	0.00E+00	0.00E+00	0.00E+00	0.00E+00	0.00E+00
0.00E+00	0.00E+00	0.00E+00	0.00E+00	0.00E+00	0.00E+00
1.22E+05	1.09E+05	1.09E+05	1.09E+05	1.21E+05	1.20E+05
1.66E+05	1.68E+05	1.86E+05	2.06E+05	2.03E+05	1.99E+05
0.00E+00	0.00E+00	0.00E+00	0.00E+00	0.00E+00	0.00E+00
1.61E+05	1.64E+05	1.84E+05	2.00E+05	1.83E+05	1.81E+05

Equivalent Mean Stress

1.42E+06	2.29E+06	2.38E+06	2.26E+06	1.76E+06	1.75E+06
3.17E+05	3.39E+05	3.44E+05	3.40E+05	3.31E+05	3.32E+05
3.17E+05	3.38E+05	3.39E+05	3.37E+05	3.30E+05	3.31E+05
4.16E+05	4.58E+05	4.81E+05	4.78E+05	5.41E+05	5.12E+05
1.22E+06	1.29E+06	1.40E+06	1.48E+06	1.50E+06	1.50E+06
3.20E+05	3.23E+05	3.26E+05	3.32E+05	3.35E+05	3.35E+05
1.62E+06	2.01E+06	2.17E+06	2.24E+06	2.36E+06	2.37E+06

Equivalent Alternating Stress

1.51E+06	2.37E+06	2.46E+06	2.34E+06	1.85E+06	1.84E+06
3.04E+05	3.08E+05	3.06E+05	3.04E+05	2.97E+05	2.96E+05
3.05E+05	3.06E+05	3.06E+05	3.04E+05	2.98E+05	2.98E+05
4.25E+05	4.56E+05	4.75E+05	4.72E+05	5.39E+05	5.10E+05
1.34E+06	1.41E+06	1.51E+06	1.59E+06	1.61E+06	1.61E+06
3.13E+05	3.07E+05	3.05E+05	3.04E+05	2.98E+05	2.97E+05
1.74E+06	2.12E+06	2.28E+06	2.35E+06	2.46E+06	2.47E+06

Cycles to Fail	8.65E+09	2.75E+07	1.24E+07	1.91E+07	1.56E+07	1.38E+07
Hours to Fail	2.09E+06	3.72E+03	1.40E+03	1.80E+03	1.26E+03	1.11E+03

Figure 6.5 Results for fatigue model. Rows represents pulleys from 1 to 7, columns represents different operation ranges (Idle, A100, B100, C100, Unloaded up and Unloaded down from left to right).

Assume that the belt drive operates a duty cycle as shown in Table 6.1. Using Equation (6.13) along with the results in Figure 6.5, the total belt drive fatigue life operating at this duty cycle is equal to:

$$Total\ Belt\ life = 1580\ hours \tag{6.14}$$

Table 6.1 Duty Cycle

Operation range	Percentage time
idle	5%
A100	9%
B100	80%
C100	4%
UnloadedUp	1%
UnloadedDown	1%

7. CASE STUDIES

Different configurations of belt drives were built using the DIS multibody dynamics software to study the variation of estimated fatigue life with different configurations. The new models are studied **ONLY** from fatigue life point of view. Other belt design criteria like belt vibration, space limitation, accessibility, and others are not considered. All the configurations were run at the same speed and load profile as the base configuration, and they are modified to have the same pretension in the belt.

Alternative configuration 1 has one less pulley than the baseline configuration and it is shown in Figure 7.1 and Table 7.1. Alternative configuration 2 is very close to Alternative configuration 1 but has more wrap angle on the tensioner that would help to rapidly take the slack from the belt. This configuration is shown In Figure 7.2 and Table 7.2. Alternative configuration 3 has the same number of pulleys as Alternative configuration 1 and 2, but the tensioner is on the back side of the belt, while the idlers are on the groove side. Alternative configuration 3 is shown in Figure 7.3 and Table 7.3. All the configurations have the same components parameters as the baseline configuration shown in Figure 3.1. The parameters are shown in Table 3.2.

Fatigue life results for the different belt-drive configurations can be calculated using the algorithm shown in Figure 6.4 with the DIS code used to calculate the stresses and forces in the system. In the following sections we will elaborate on the different configurations. The results and conclusion are discussed later in this chapter.

7.1 Alternative Configuration 1

The main idea behind alternative configuration 1 is taking one of the idler pulleys out of the drive. By removing one idler we expect to eliminate the bending, shear and transverse stress developed on this pulley. If an idler was a forward wrapped idler (i.e. it contacts the belt at the rib side), the shear and transverse stresses will decrease the belt fatigue life, while the bending stress will be subtracted from the axial stress resulting in higher fatigue life. On the other hand, if the idler was a back wrapped idler (i.e. it contact the belt on the flat side), the transverse and shear stress will have no effect on the rib, but the bending stress will add to the axial stress at the rib tip. As a result, we eliminated a back wrapped idler hoping to get a higher fatigue life.

Figure 7.1 shows the layout of the suggested model. Table 7.1 shows the location of the pulleys and different idlers, as well as the diameter of the pulleys. The model parameters are the same as the baseline configuration, except for the tensioner arm initial torque and belt length. The tensioner initial torque was changed to 60 N.m so that the initial tension in the belt matches the baseline configuration. As one pulley was removed and other pulleys had different locations, the belt length was also changed to match the new configuration.

The change in the configuration took only the fatigue life into consideration. Other criteria like belt vibration and space limitation were not considered. This is done purely for research purpose to discuss the effect of different configurations on the fatigue life time and not intended to be a complete belt drive design.

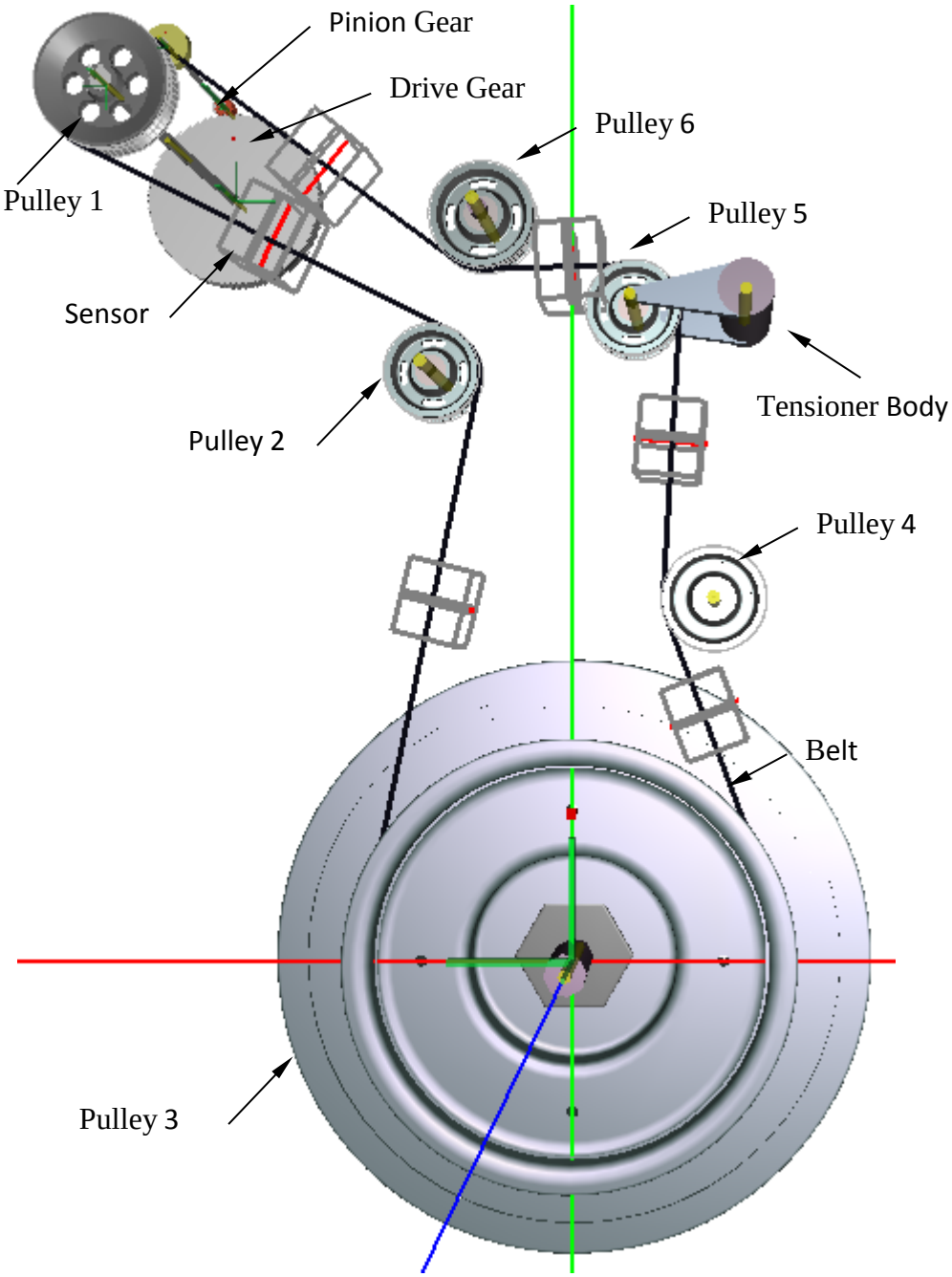

Figure 7.1 Alternative configuration 1 belt drive model

Table 7.1 Layout and geometry of different pulleys

Pulley #	X-Coordinate (mm)	Y- Coordinate (mm)	Pitch diameter (mm)
1	-407.90	722.60	104.4
2	-111.2	474.5	74
3	0.00	0.00	338.3
4	114.8	292.5	82.5
5	50.1	525.6	74
6	-71	600	82.5
Tensioner arm pivot	140	530	N/A

7.2 Alternative Configuration 2

In alternative configuration 2, the main idea was to increase the wrap angle of the belt around the pulley. This makes the direction of the movement of the tensioner the same as the axial direction of the belt spans which will help taking over the slack in the belt quickly. This is because both belt spans will have a larger displacement component in the belt axial direction which means more axial belt displacement for the same unit of the tensioner displacement. This will help the belt derive keep the desired tension without delay and avoid aggressive tension corrections due to belt slack.

Figure 7.2 shows the layout of alternative configuration 2, with increased wrap angle on the tensioner. Table 7.2 contains the coordinates of each pulley, as well as their diameters.

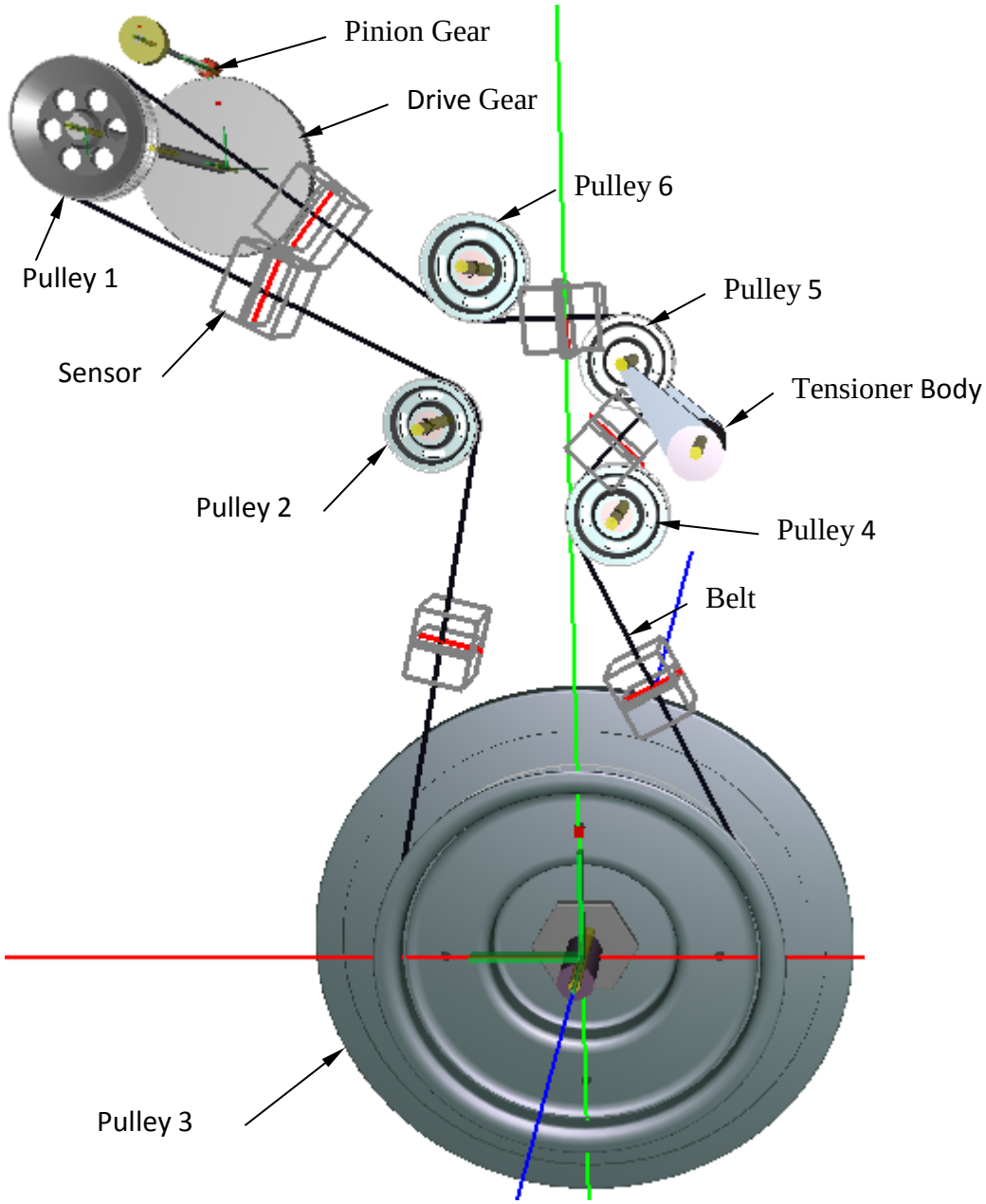

Figure 7.2 Alternative configuration 2 belt drive model

To make a fair comparison between this configuration and the base configuration, the initial tensioner torque was tuned to 110.5 N.M to keep the same initial tension as the one in the baseline configuration. This configuration was studied only from the fatigue life point of view, and didn't consider any other criteria like vibration or space limitation. It's intended only for research purpose and not intended to be a complete design.

Table 7.2 Layout and geometry of different pulleys for alternative configuration2

Pulley #	X-Coordinate (mm)	Y-Coordinate (mm)	Pitch diameter (mm)
1	-407.90	722.60	104.4
2	-111.2	474.5	74
3	0.00	0.00	338.3
4	40	400	82.5
5	107.4	456.3	74
6	-71	600	82.5
Tensioner pivot	107.4	456.3	N/A

7.3 Alternative Configuration 3

As mentioned before in Section 7.1, the back wrapped pulley (contact the belt at the flat side) will results in bending stress added to the axial stress in the rib tip section while there will be no transverse or shear stress. On the other hand, in the forward wrapped pulleys (contact with the belt at the rib side) the bending stress is subtracted from the axial stress, while transverse and shear stress are added. Investigating the last two statements, we cannot say explicitly which kind of wrapping will result in less stress. If the bending is more dominant in the system than transverse and shear stress, then a

forward wrapped pulley will be preferable in the sense of increasing the fatigue life time. On the other hand, if the transverse and shear stress are more dominant than the bending stress, a backward wrapped pulley would be a preferred design.

As mentioned before in Section 5.2, bending moment depends mainly on the geometry and on the belt material which are constant. On the other hand, the shear and transverse stresses depend on the dynamics of the system. Mathematically, we can say that the higher the dynamics in the system, the more dominant the transverse and shear stresses. However by experience, it was found that the transverse and shear stresses are generally less dominant and the bending stress is more dominant. Belt manufacturers and designers recommend that the pulleys are preferable to be forward wrapped (grooved pulley in contact with belt ribs) rather than being back wrapped (flat pulleys contact the flat belt side). This shows the dominance of the bending stress over the transverse and shear stresses. In this configuration the wrapping angle around the tensioner has increased. Moreover, the tensioner wrapping changed sides from being forward wrapped to be backward wrapped. At the same time, idler 4 and 6 has changed wrapping side from backward wrap to forward wrap. In this case, we have two forward wrapped pulleys and one backward versus of two backward and one forward in alternative configurations 1 and 2. Figure 7.3 shows the layout of the suggested configuration and the wrapping of each pulley. Table 7.3 lists the coordinates of the centers of different pulleys, as well as their diameters. As in the previous configurations, the initial torque of the tensioner was tuned so that the initial belt tension matches the baseline configuration. The tuned value of the initial torque is 124 N.m. The belt length has changed as needed to fit in the new configuration.

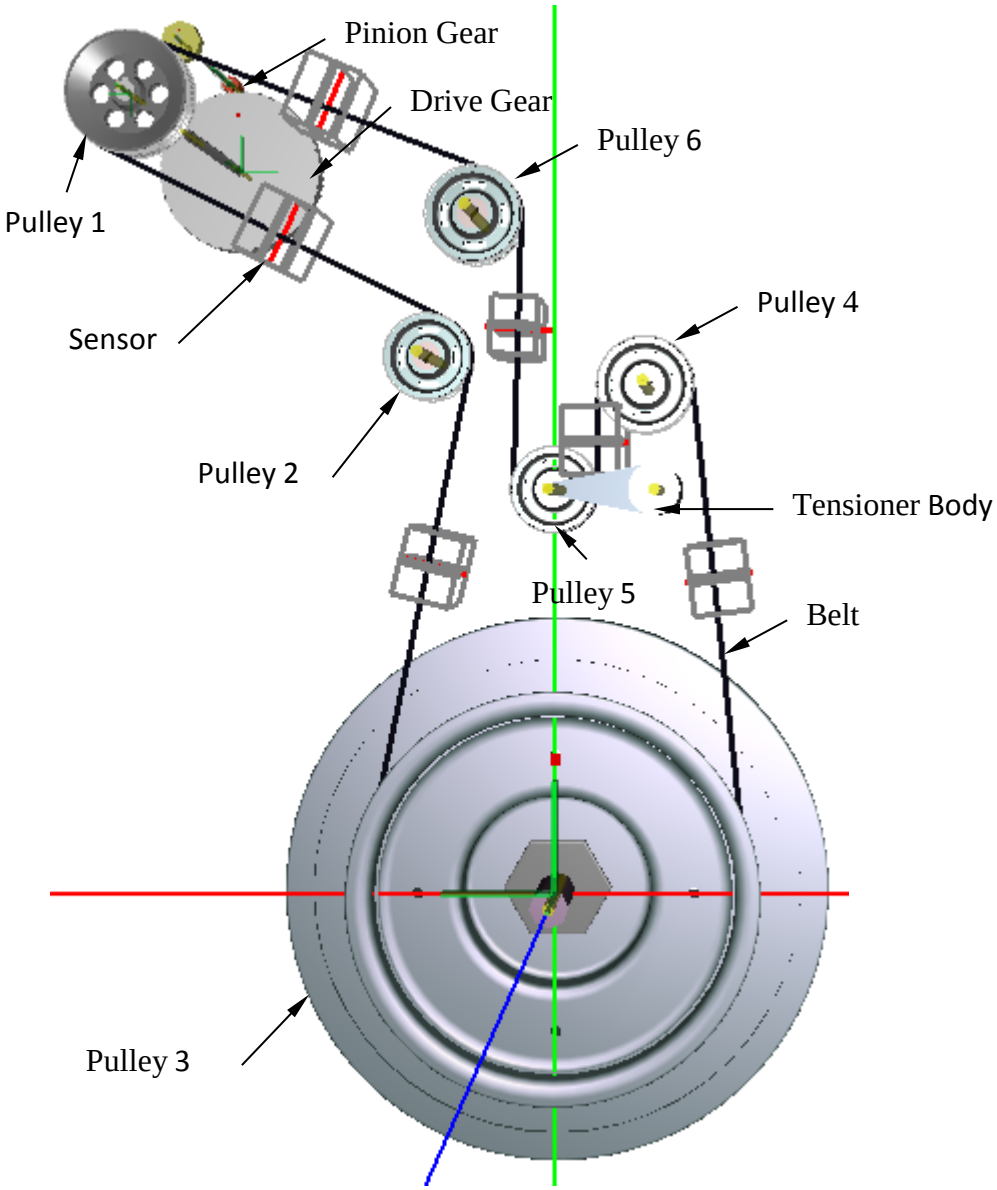

Figure 7.3 Alternative configuration 3 belt drive model

Table 7.3 Layout and geometry of different pulleys

Pulley #	X-Coordinate (mm)	Y- Coordinate (mm)	Pitch diameter (mm)
1	-407.90	722.60	104.4
2	-111.2	474.5	74
3	0.00	0.00	338.3
4	80	450	82.5
5	0	357.7	74
6	-71	600	82.5
Tensioner pivot	90	357.5	N/A

7.4 Results and Discussion

Figure 7.4 to Figure 7.6 show the stress and fatigue life results for different alternate configurations. For each table in the figure, the columns represent one of the six different operation ranges, namely idle, A100, B100, C100, Unloaded up and Unloaded down, respectively. Each row represent different pulleys with the upper row represent pulley1 and the going in ascending order to pulley 6 in the last row.

Although one pulley was removed from the baseline in alternative configuration 1, the belt fatigue life is less than that of the baseline configuration in all ranges of operation. We expected that eliminating stresses on the removed pulley would increase the belt fatigue life however this configuration led to increased belt-drive vibrations which caused higher belt stresses. Similarly, in alternative configuration 2, the belt life is less than that of alternative configuration 1 in all operating ranges, which again was opposite to our expectation. In alternative configuration 3, results were more complicated. The belt life increased in the idle operating range, however it decreased in all other operating ranges. This shows that the belt fatigue prediction model in conjunction with the multibody dynamics model of the belt-drive are essential for accurate prediction of the belt fatigue life.

Mean Ax. Stress

2.97E+04	3.94E+04	4.47E+04	4.62E+04	4.09E+04	4.05E+04
2.71E+04	4.68E+04	4.96E+04	4.83E+04	3.83E+04	3.86E+04
2.47E+04	4.01E+04	4.01E+04	4.13E+04	4.09E+04	4.10E+04
2.83E+04	3.24E+04	3.37E+04	3.80E+04	4.23E+04	4.28E+04
2.66E+04	2.81E+04	3.35E+04	3.77E+04	4.11E+04	4.19E+04
1.73E+04	2.12E+04	2.13E+04	2.28E+04	2.31E+04	2.38E+04

Alternating Ax. Stress

1.12E+04	2.42E+04	2.19E+04	1.85E+04	4.92E+03	4.23E+03
1.39E+04	1.68E+04	1.70E+04	1.64E+04	7.50E+03	6.13E+03
1.15E+04	2.22E+04	2.05E+04	1.91E+04	1.00E+04	8.52E+03
7.95E+03	1.33E+04	1.39E+04	1.35E+04	8.60E+03	6.65E+03
7.52E+03	1.23E+04	9.83E+03	1.07E+04	7.09E+03	5.82E+03
1.68E+04	2.07E+04	2.09E+04	2.23E+04	2.26E+04	2.33E+04

Bending Stress

-4.12E+05	-4.12E+05	-4.12E+05	-4.12E+05	-4.12E+05	-4.12E+05
4.97E+05	4.97E+05	4.97E+05	4.97E+05	4.97E+05	4.97E+05
-1.26E+05	-1.26E+05	-1.26E+05	-1.26E+05	-1.26E+05	-1.26E+05
4.97E+05	4.97E+05	4.97E+05	4.97E+05	4.97E+05	4.97E+05
-5.81E+05	-5.81E+05	-5.81E+05	-5.81E+05	-5.81E+05	-5.81E+05
4.97E+05	4.97E+05	4.97E+05	4.97E+05	4.97E+05	4.97E+05

Transverse Stress

-3.16E+06	-4.85E+06	-5.14E+06	-6.52E+06	-5.33E+06	-5.37E+06
0.00E+00	0.00E+00	0.00E+00	0.00E+00	0.00E+00	0.00E+00
-7.90E+05	-3.53E+06	-3.55E+06	-3.73E+06	-3.81E+06	-3.75E+06
0.00E+00	0.00E+00	0.00E+00	0.00E+00	0.00E+00	0.00E+00
-4.33E+06	-4.77E+06	-4.61E+06	-4.72E+06	-4.93E+06	-4.94E+06
0.00E+00	0.00E+00	0.00E+00	0.00E+00	0.00E+00	0.00E+00

Equivalent Mean Stress

1.41E+06	2.26E+06	2.41E+06	3.10E+06	2.50E+06	2.52E+06
2.76E+05	2.95E+05	2.98E+05	2.97E+05	2.87E+05	2.87E+05
3.56E+05	1.74E+06	1.75E+06	1.84E+06	1.88E+06	1.85E+06
2.77E+05	2.81E+05	2.82E+05	2.87E+05	2.91E+05	2.91E+05
1.90E+06	2.12E+06	2.05E+06	2.11E+06	2.21E+06	2.22E+06
2.66E+05	2.70E+05	2.70E+05	2.71E+05	2.72E+05	2.72E+05

Equivalent Alternating Stress

1.50E+06	2.34E+06	2.48E+06	3.17E+06	2.58E+06	2.60E+06
2.62E+05	2.65E+05	2.66E+05	2.65E+05	2.56E+05	2.55E+05
3.72E+05	1.73E+06	1.74E+06	1.83E+06	1.87E+06	1.84E+06
2.57E+05	2.62E+05	2.62E+05	2.62E+05	2.57E+05	2.55E+05
2.04E+06	2.26E+06	2.19E+06	2.25E+06	2.35E+06	2.36E+06
2.65E+05	2.69E+05	2.69E+05	2.71E+05	2.71E+05	2.72E+05

Cycles to Fail	5.56E+08	2.59E+07	1.13E+07	8.45E+04	5.07E+06	4.39E+06
Hours to Fail	1.28E+05	3.34E+03	1.21E+03	7.58E+00	3.89E+02	3.37E+02

Figure 7.4 Stress and fatigue results for alternative configuration 1

Mean Ax. Stress

3.05E+04	3.97E+04	4.58E+04	4.62E+04	4.31E+04	4.32E+04
2.59E+04	4.77E+04	5.09E+04	4.81E+04	3.99E+04	4.04E+04
2.26E+04	3.74E+04	4.09E+04	4.26E+04	4.30E+04	4.32E+04
2.84E+04	3.81E+04	3.92E+04	4.26E+04	4.48E+04	4.55E+04
2.74E+04	3.36E+04	3.65E+04	4.26E+04	4.44E+04	4.45E+04
1.53E+04	2.15E+04	2.17E+04	2.22E+04	2.41E+04	2.41E+04

Alternating Ax. Stress

1.04E+04	2.38E+04	2.14E+04	1.50E+04	4.32E+03	3.87E+03
1.50E+04	1.58E+04	1.63E+04	1.31E+04	7.52E+03	6.62E+03
1.18E+04	2.47E+04	2.07E+04	1.74E+04	1.07E+04	9.40E+03
5.96E+03	2.24E+04	1.71E+04	1.49E+04	8.97E+03	7.09E+03
5.09E+03	1.63E+04	9.94E+03	9.59E+03	6.40E+03	5.48E+03
1.48E+04	2.10E+04	2.13E+04	2.17E+04	2.37E+04	2.36E+04

Bending Stress

-4.12E+05	-4.12E+05	-4.12E+05	-4.12E+05	-4.12E+05	-4.12E+05
4.97E+05	4.97E+05	4.97E+05	4.97E+05	4.97E+05	4.97E+05
-1.26E+05	-1.26E+05	-1.26E+05	-1.26E+05	-1.26E+05	-1.26E+05
4.97E+05	4.97E+05	4.97E+05	4.97E+05	4.97E+05	4.97E+05
-5.81E+05	-5.81E+05	-5.81E+05	-5.81E+05	-5.81E+05	-5.81E+05
4.97E+05	4.97E+05	4.97E+05	4.97E+05	4.97E+05	4.97E+05

Transverse Stress

-3.20E+06	-4.95E+06	-5.23E+06	-6.73E+06	-5.71E+06	-5.72E+06
0.00E+00	0.00E+00	0.00E+00	0.00E+00	0.00E+00	0.00E+00
-9.06E+05	-1.41E+06	-3.66E+06	-4.18E+06	-4.49E+06	-4.47E+06
0.00E+00	0.00E+00	0.00E+00	0.00E+00	0.00E+00	0.00E+00
-4.39E+06	-4.65E+06	-4.85E+06	-5.10E+06	-5.25E+06	-5.27E+06
0.00E+00	0.00E+00	0.00E+00	0.00E+00	0.00E+00	0.00E+00

Equivalent Mean Stress

1.42E+06	2.31E+06	2.46E+06	3.20E+06	2.69E+06	2.70E+06
2.74E+05	2.96E+05	2.99E+05	2.97E+05	2.88E+05	2.89E+05
4.12E+05	6.80E+05	1.81E+06	2.07E+06	2.23E+06	2.22E+06
2.77E+05	2.87E+05	2.88E+05	2.91E+05	2.93E+05	2.94E+05
1.93E+06	2.07E+06	2.17E+06	2.30E+06	2.38E+06	2.39E+06
2.64E+05	2.70E+05	2.70E+05	2.71E+05	2.73E+05	2.73E+05

Equivalent Alternating Stress

1.51E+06	2.39E+06	2.53E+06	3.28E+06	2.77E+06	2.77E+06
2.64E+05	2.64E+05	2.65E+05	2.62E+05	2.56E+05	2.55E+05
4.29E+05	6.73E+05	1.79E+06	2.05E+06	2.21E+06	2.20E+06
2.55E+05	2.71E+05	2.66E+05	2.63E+05	2.58E+05	2.56E+05
2.07E+06	2.20E+06	2.31E+06	2.44E+06	2.51E+06	2.53E+06
2.63E+05	2.70E+05	2.70E+05	2.70E+05	2.72E+05	2.72E+05

Cycles to Fail	4.15E+08	2.18E+07	7.25E+06	4.24E+04	1.23E+06	1.18E+06
Hours to Fail	9.57E+04	2.81E+03	7.79E+02	3.80E+00	9.41E+01	9.09E+01

Figure 7.5 Stress and fatigue results for alternative configuration 2

Mean Ax. Stress

3.10E+04	4.12E+04	4.83E+04	4.81E+04	4.36E+04	4.38E+04
2.59E+04	4.85E+04	5.21E+04	4.88E+04	4.04E+04	4.11E+04
2.24E+04	3.61E+04	4.26E+04	4.41E+04	4.31E+04	4.41E+04
2.88E+04	3.85E+04	4.03E+04	4.21E+04	4.58E+04	4.63E+04
2.73E+04	3.46E+04	3.77E+04	4.29E+04	4.59E+04	4.61E+04
1.48E+04	2.03E+04	2.04E+04	2.16E+04	2.37E+04	2.36E+04

Alternating Ax. Stress

1.06E+04	2.32E+04	2.07E+04	1.40E+04	4.50E+03	3.88E+03
1.57E+04	1.58E+04	1.68E+04	1.32E+04	7.71E+03	6.59E+03
1.21E+04	2.41E+04	2.08E+04	1.63E+04	1.04E+04	9.59E+03
5.67E+03	2.09E+04	1.37E+04	1.15E+04	7.66E+03	7.43E+03
4.34E+03	1.32E+04	9.07E+03	8.57E+03	5.95E+03	5.18E+03
1.43E+04	1.98E+04	1.99E+04	2.11E+04	2.33E+04	2.31E+04

Bending Stress

-4.12E+05	-4.12E+05	-4.12E+05	-4.12E+05	-4.12E+05	-4.12E+05
4.97E+05	4.97E+05	4.97E+05	4.97E+05	4.97E+05	4.97E+05
-1.26E+05	-1.26E+05	-1.26E+05	-1.26E+05	-1.26E+05	-1.26E+05
-4.97E+05	-4.97E+05	-4.97E+05	-4.97E+05	-4.97E+05	-4.97E+05
5.81E+05	5.81E+05	5.81E+05	5.81E+05	5.81E+05	5.81E+05
-4.97E+05	-4.97E+05	-4.97E+05	-4.97E+05	-4.97E+05	-4.97E+05

Transverse Stress

-3.18E+06	-4.92E+06	-5.28E+06	-6.76E+06	-5.69E+06	-5.78E+06
0.00E+00	0.00E+00	0.00E+00	0.00E+00	0.00E+00	0.00E+00
-9.30E+05	-1.07E+06	-1.50E+06	-1.66E+06	-1.88E+06	-1.92E+06
-3.66E+06	-5.10E+06	-5.74E+06	-6.05E+06	-6.38E+06	-6.41E+06
0.00E+00	0.00E+00	0.00E+00	0.00E+00	0.00E+00	0.00E+00
-3.89E+06	-8.72E+05	-1.06E+06	-1.44E+06	-1.27E+06	-1.31E+06

Equivalent Mean Stress

1.42E+06	2.29E+06	2.48E+06	3.22E+06	2.68E+06	2.73E+06
2.74E+05	2.97E+05	3.01E+05	2.97E+05	2.89E+05	2.90E+05
4.24E+05	5.06E+05	7.29E+05	8.13E+05	9.21E+05	9.41E+05
1.61E+06	2.34E+06	2.66E+06	2.82E+06	2.99E+06	3.00E+06
3.18E+05	3.25E+05	3.28E+05	3.33E+05	3.36E+05	3.37E+05
1.71E+06	2.08E+05	3.03E+05	4.91E+05	4.09E+05	4.30E+05

Equivalent Alternating Stress

1.51E+06	2.37E+06	2.56E+06	3.29E+06	2.76E+06	2.80E+06
2.64E+05	2.64E+05	2.65E+05	2.62E+05	2.56E+05	2.55E+05
4.41E+05	5.08E+05	7.19E+05	8.04E+05	9.14E+05	9.33E+05
1.72E+06	2.43E+06	2.75E+06	2.91E+06	3.08E+06	3.09E+06
2.95E+05	3.04E+05	3.00E+05	2.99E+05	2.96E+05	2.96E+05
1.83E+06	4.09E+05	4.88E+05	6.52E+05	5.81E+05	6.01E+05

Cycles to Fail	2.67E+09	1.14E+07	1.32E+06	3.56E+04	1.51E+05	1.33E+05
Hours to Fail	6.14E+05	1.47E+03	1.42E+02	3.19E+00	1.16E+01	1.02E+01

Figure 7.6 Stress and fatigue results for alternative configuration 3

8. CONCLUDING REMARKS AND FUTURE WORK

8.1 Concluding Remarks

A numerical model was built using an explicit finite element code to simulate a belt-drive. The code uses the trapezoidal integration rule along with an explicit solution procedure to solve the multibody dynamics differential equations, presented in Chapter 2. The belt was modeled using three-node beam elements to account for bending stiffness, while the pulleys, shafts and tensioner body were modeled as rigid bodies. The pulleys have a cylindrical contact surface. The *penalty technique* was used to model contact between the belt and the pulleys. An *asperity-based friction* model was used to approximate the coulomb friction between the belt and the pulleys. To account for the stiffness of the shafts, torsional spring(s) were added at one or both sides of the shaft. The spring(s) equivalent stiffness is equal to the equivalent stiffness of the shaft, and the spring(s) equivalent damping is equal to the equivalent damping of the shaft. Virtual sensors were placed on each belt span to measure belt tension, belt deflection and number of belt node at the sensor position.

There were two inputs defined for the model. The first is the crank angle velocity and it has a velocity profile shown in Figure 3.2. The profile represents 6 operation ranges operating at 5 distinctive average angular velocities. There is a time gap (0.2 seconds) between different ranges to ramp the average angular velocities between different operating ranges. The second input is the turbine torque, and it has a profile that is dependent on the turbine angular velocity as shown in Figure 3.3. The drive shaft (refer to Figure 3.1 for definition) angular velocity and torque obtained by the model were compared to experimental results, supplied by Cummins, Inc., that were obtained from a physical belt-drive. The two results showed excellent agreement match for the 4 operation ranges with the lower crankshaft angular velocity. For the 2 ranges operating at average crankshaft angular velocity 2100 rpm, there was some frequencies in the experimental results that were not matched by corresponding frequencies calculated by the finite element model. By investigating the response of the belt-drive in the experimental results, the number of frequencies was much more than the number of frequencies in the input (crankshaft angular velocity). Hence it was obvious that some of these frequencies were due to other excitation sources than the crankshaft dynamics. These excitations (such as structural resonance) are not included in the numerical model, and hence it is not expected to see such frequencies in the numerical response. To get the complete system response, the whole system should be modeled including the mounting structure of the belt-drive. Comparison plots between numerical and experimental results for the belt-drive response are shown in Section 3.5.

A parameter sensitivity study was performed to evaluate the change in response due to change in specific parameter. Different parameters for different components were studied such as tensioner arm viscous and coulomb damping, belt axial stiffness and damping, belt torsional stiffness and damping, the coefficient of friction between the belt and pulleys, gear-tooth backlash, gear tooth stiffness and damping, and stiffness and damping of shafts. The parameters that had the most significant effect on the response were the viscous and frictional (Coulomb) damping of the tensioner arm pivot, and the coefficient of friction between the belt and the pulleys.

After the numerical model was validated, more information was obtained from the numerical model including normal and tangential forces between the belt and the pulleys as well as the tension force in the belt. This information was used in Chapter 5 to calculate different stresses applied on the belt rib. The different stresses were added using Sine's theory and represented by an equivalent uniaxial stress. The uniaxial stress was then used in Chapter 6 as a damage criterion to estimate the belt life time based on fatigue model. As the belt chords have much larger Young's modulus than the rubber, the chords will limit the rubber strain keeping in the linear elastic zone. Hence, *High Cycle Fatigue (HCF)* model was used and modified Basquin relation was employed to estimate the fatigue life of the belt. The fatigue life was estimated for every operating range and the results are shown in Section 6.7.

Furthermore, three different alternative configurations of the numerical model belt drive were built and simulated for the same input. The different configurations have the same input, the same material properties and the same belt initial tension, but different idler pulleys and tensioner positions and configurations. All the alternatives have one less pulley than the baseline configuration. The response was observed for each configuration and the same analysis was done to calculate the stresses and fatigue life. The three configurations were found to have lower fatigue life than the baseline configuration although they have one less pulley. The results were shown in Section 7.4.

Design configuration changes proposed in Chapter 7 were expected to improve the belt fatigue life; however they had an opposite effect. One main reason is that it is hard to change one condition without affecting other conditions in the system. This appears clearly in the alternative configuration 1, it was expected that one less pulley will eliminate the stresses on the pulley taken out while the stresses on other pulleys will be the same. This will consequently increase the belt fatigue life. After running the simulation and calculating the belt fatigue life, it was found that this assumption was invalid because changing the configuration of the system led to higher belt-drive vibrations. A more complicated case was alternative configuration 3. The effect of the change was not the same in all the ranges. Results show that the estimated belt life-time

is increased in the idle operation range, while the estimated life-time was decreased in all the other operation ranges.

The above conclusion elaborates the importance of the calculation of the system response taking all the effects into account. It also elaborates the importance of using a computational model that can simulate the physical model with high level fidelity. This computational model will give the flexibility of tuning the system and check different configurations while eliminating the cost and the time of setting up test rigs.

Due to the dynamic interactions between different bodies, a single change in the system will propagate in the entire system making it challenging to estimate the resultant change of the system response. Having a high-fidelity multibody numerical model allows designers to obtain an accurate system response of the final product in the design phase. Further analysis can be done and the system response due to different modifications can be accurately predicted. The main challenge to build a numerical model is to predict material properties such as fatigue strength, fatigue exponent index, and belt axial/bending damping, which need to be experimentally determined. This becomes even more challenging when the material property changes due to different operation conditions like Young's modulus changes with operating temperature. One way to overcome this uncertainty is to do a parameter sensitivity study to find the range of the property change and predict the range of the corresponding responses. Other solution is to take the most severe case, or the average of the range of change. The designer shall make the best judgment depending on the application of the model.

8.2 Future Work

As shown in Section 5.1 the system response can vary due to a change in the model parameter. Also Table 5.1 shows how Young’s modulus of the belt rib rubber can vary significantly due to time aging or operating temperature. Young’s modulus has a direct impact on the belt stiffness and damping. Further studies to involve the effect of

operating temperature in the model will help to improve the prediction of the model response in actual operating conditions.

Fatigue failure is only one mode of belt failure. It is true it is most common, but it is not the only mode. Belts may fail due to wear as a result of the friction between the belt and the pulley. Further work to predict the belt life due to wear failure is needed.

In this thesis, belt fatigue was studied for different operation ranges, where each operation range represents a steady-state operation condition. However, the belt-drive can experience transient operating conditions like engine start-up. Accessory belt-drives experience large stresses on the engine start-up to overcome the inertia associated with starting the power steering pump, the alternator, the A/C compressor and the fan, especially if those components are engaged. However, for the belt-drive studied in this thesis is not an accessory belt-drive. It is not expected to have large stresses on the engine startup because the turbine will not be loaded at startup. For more general cases, it will be helpful to evaluate the startup operating conditions as well as other operation conditions such as sudden accelerations/decelerations and wet operating conditions and study their effects.

Also Chapter 7 can be used as a start point for further optimization study to obtain the highest fatigue life time. An optimization model can be developed using the fatigue life model introduced in this thesis to compare different belt configurations, and hence, optimize the design.

LIST OF REFERENCES

LIST OF REFERENCES

[1] S. Ashley. *Recovering exhaust heat to generate electricity and boost efficiency*. Last accessed (2011, 2/28/2012). Available: http://www.sae.org/mags/aei/7916

[2] J. Ringler, M. Seifert, and V. G. a. W. Hübner, "Rankine Cycle for Waste Heat Recovery of IC Engines," *SAE International,* vol. 2, p. 10, 2009.

[3] *Temperatures rise in BMW's work to recover engine waste heat*. Last accessed (2012, 2/14/2012). Available: http://www.sae.org/mags/AEI/10647

[4] G. J. Lake and P. B. Lindley, "The Mechanical Fatigue Limit for Rubber," *Journal of Applied Polymer Science,* vol. 9, pp. 1233-1251, 1965.

[5] Y. S. Huang and O. H. Yeoh, "Crack Initiation and Propagation in Modelcord-Rubber Composites," presented at the American chemical society, Ohio, 1988.

[6] J. N. Fawcett, "Chain and Belt drives review," *Shock and vibration,* vol. 13, pp. 5-12, 1981.

[7] D. Frhzson, "Life Prediction of V-Belts Related to Fatigue Mechanisms," *Transactions of the ASME,* vol. 111, pp. 424 - 433, 1989.

[8] S. Karunendiran, "Development of a New Model for the Prediction of Automotive Serpentine Belt Life," Ph.D, Mechanical and Industrial Engineering, University of Toronto, 2009.

[9] S. Karunendiran, M. Clark, and J. W.Zu, "A New Approach for Life Prediction of Serpentine Accessory Belt Drive System Using Actual Measured Data," presented at the SAE World Congress & Exhibition, Detrit, Michigan - USA 2009.

[10] S. Sundararaman, J. Hu, J. Chen, and K. Chandrashekhara, "Temperature dependent fatigue-failure analysis of V-ribbed serpentine belts," *International journal of Fatigue,* vol. 31, pp. 1262-1270, 2009.

[11] T. Ha-Anh and T. Vu-khanh, "Prediction of mechanical properties of polychloroprene during thermo-oxidative aging," *Polymer testing*, vol. 24, September 2005 2005.

[12] F. Nassiri, "New Approach in Characterizing Accessory Drive Belts for Finite Element Applications," Master of Applied Science, Department of Mechanical and Industrial Engineering, University of Toronto, 2010.

[13] D. Yu, T. H. C. Childs, and K. W. Dalgarno, "V-ribbed belt design, wear and traction capacity," in *Proceedings of the Institution of Mechanical Engineers*, ProQuest Central, 1998, p. 333.

[14] M. J. Leamy and T. M. Wasfy, "Transient and Steady-State Dynamic Finite Element Modeling of Belt-Drives," *Journal of Dynamic Systems, Measurement, and Control*, vol. 124, pp. 575-581, 2002.

[15] M. J. Leamy and T. M. Wasfy, "Analysis of Belt-Drive Mechanics Using a Creep-Rate-Dependent Friction Law," *Transactions of the ASME*, vol. 69, pp. 763-771, November 2002 2002.

[16] T. Wasfy, M. Leamy, and R. J. Meckstroth, "Prediction of system natural frequencies using explicit finite element code with application to belt drive," in *ASME 2004 Design Engineering Technical Conferences and Computers and Information in Engineering Conference*

[17] *DIS (Dynamic Interactions Simulator)*. Last accessed (January 2013). Available: http://www.ascience.com/ScProducts.htm

[18] T. M. Wasfy, J. O'Kins, and D. Ryan, "Experimental Validation of a Multibody Dynamics Model of the Suspension System of a Tracked Vehicle," in *2011 NDIA Vehicles Systems Engineering and Technology Symposium*, Dearborn, Michigan, USA, 2011.

[19] T. Wasfy, "Modeling Spatial Rigid Multibody Systems Using an Explicit-Time Integration Finite Element Solver and A Penalty Formulation," in *28th Biennial Mechanisms and Robotics Conference*, Salt Lake, Utah, 2004.

[20] T. M. Wasfy, "Asperity Spring Friction Model with Application to Belt-Drives," in *ASME 2003 Design Engineering Technical Conferences*, 2003.

[21] M. J. Leamy, T. M. Wasfy, and R. J. Meckstroth, "Finite Element Study of Belt-Drive Frictional Contact under Harmonic Excitation," presented at the SAE 2004 World Congress & Exhibition, Detroit, Michigan, United States, 2004.

[22] W. D. Pilkey, *Formulas for Stress, Strain, and Structural Matrices*. New York - United States of America: John Wiley & sons, Inc. , 1994.

[23] G. E. Dieter, *Material Selection and Design*. USA: ASM International, 1997.

[24] S. S. Manson and G. R. Halford, *Fatigue and Durability of Structural Material*. OH - USA: ASM International, 2006.

[25] J. Carvill, *Mechanical Engineer's Data Handbook*: Butterworth-Heinemann An imprint of Elsevier Science Linacre House, Jordan Hill, Oxford OX2 8DP 200 Wheeler Road, Burlington MA 01803, 1993.

[26] R. J. Meckstroth, T. M. Wasfy, and M. J. Leamy, "Finite Element Study of Dynamic Response of Serpentine Belt-Drives with Isolator Clutches," presented at the SAE 2004 World Congress & Exhibition, Detroit, Michigan, United States, 2004.

[27] A. G. Piersol and T. L. Paez, *Harris' shock and vibration handbook*, 6 ed. USA: McGraw-Hill Companies Inc. , 2010.

[28] T. M. Wasfy and M. Leamy, "Effect of Bending Stiffness on the Dynamic and Steady-State Responses of Belt-Drives," in *ASME 2002 Design Engineering Technical Conferences*, Montreal, Canada, 2002.